Automated detection of propagating cracks in RC beams without shear reinforcement

Von der Fakultät für Bauingenieurwesen der Rheinisch-Westfälischen Technischen Hochschule
Aachen zur Erlangung des akademischen Grades eines Doktors
der Ingenieurwissenschaften genehmigte Dissertation

vorgelegt von

Fahad Seemab, M. Sc.

Berichter: Prof. Dr.-Ing. Josef Hegger
Prof. Dr. habil. Rostislav Chudoba
Prof. Dr.-Ing. Yuri Petryna

Tag der mündlichen Prüfung: 30.10.2024

Zusammenfassung

Trotz umfangreicher Forschungsarbeiten zum Thema Querkrafttragfähigkeit von in Stahlbetonlängsbalken fehlt noch immer ein allgemeiner Konsens in der wissenschaftlichen Gemeinschaft über die Plausibilität der Annahmen, die in die Entwicklung der analytischen Modelle für die Schubausbreitung einfließen.

In dieser Arbeit wird ein automatisiertes Risserkennungswerkzeug zur Identifizierung von Rissen und zur Charakterisierung der Risskinematik sowie der resultierenden Spannungen und Kräfte entwickelt, um den mechanischen Hintergrund des Schubversagens zu verstehen.

Das vorliegende System soll einen vollständigen Einblick in die Schubrisse in längsbewehrten Betonbalken ohne Bügel geben. Darüber hinaus soll in dieser Arbeit ein analytisches Modell zur Bewertung der Querkraft-kapazität solcher Träger und den Vergleich der Kinematik des Modells mit der gemessenen Kinematik des Rissmessgeräts.

Die Ergebnisse der Risskinematik, die mit dem automatischen Risserkennungswerkzeug gewonnen wurden, werden auch mit der GOM-Benutzeroberfläche verglichen, bei der die Risskinematik manuell extrahiert wird und in hohem Maße von der Erfahrung des Benutzers abhängig ist. Die Studie zielt darauf ab, die Effizienz des Anwenders und die Zuverlässigkeit von GOM zu verbessern, da die Ergebnisse von GOM aufgrund der Abhängigkeit vom Fachwissen des Anwenders mitunter unzuverlässig sind.

Als Ergebnis des Risserkennungswerkzeugs lassen sich die Rissöffnung und die Gleitkinematik genau bestimmen, und es werden die Plausibilität und die Grenzen der in der Literatur existierenden konstitutiven Gesetze zur Berücksichtigung verschiedener Mechanismen, die zwischen dem Riss wirken, überprüft und Potenziale aufgezeigt. Darüber hinaus zeigt der Vergleich der Ergebnisse mit dem in Entwicklung befindlichen analytischen Modell die Grenzen des diskreten Rissmodells bei der Vorhersage des Querkrafttrag-verhaltens in längsbewehrten Betonbalken ohne Querkraftbewehrung.

Abstract

In spite of significant research on the topic of shear zones in the longitudinal reinforced concrete beams, still a general consensus among the scientific community regarding the plausibility on the assumptions incorporated into the development of the analytical models for shear crack propagation is missing.

In this thesis, an automated crack detection tool for the identification of cracks and characterization of the crack kinematics, its stress and force resultants is developed to understand the mechanical background of shear failure.

The present framework aims to provide a complete insight into the shear cracks existing in the longitudinally reinforced concrete beams without stirrups. Furthermore, the thesis aims to also develop an analytical model for evaluating the shear capacity of such beams and comparing the kinematics from the model with the measured kinematics from the crack detection tool.

The crack kinematics results obtained from the automated crack detection tool are compared with those extracted manually using the GOM user interface. The manual extraction process heavily relies on user expertise, making the results from GOM sometimes unreliable. This study aims to enhance user efficiency and reduce reliance on GOM by minimizing the variability caused by user dependence.

The crack detection tool enables precise measurement of crack opening and sliding kinematics. It also evaluates the validity and limitations of existing constitutive laws in the literature concerning the interactions occurring within the crack. Furthermore, a comparison with the developing analytical model reveals the limitations of the discrete crack model in accurately predicting the shear behavior of longitudinally reinforced concrete beams lacking shear reinforcement.

Acknowledgments

This dissertation, titled "Automated Detection of Propagating Cracks in RC Beams without Shear Reinforcement," is the culmination of my six years of work as a research assistant at the Institute of Structural Concrete (Institut für Massivbau) at RWTH Aachen University. I am deeply grateful to the Deutsche Forschungsgemeinschaft (DFG) for funding this research and for their invaluable support throughout the project. I would also like to extend my heartfelt thanks to the Deutscher Akademischer Austauschdienst (DAAD) for awarding me a grant that enabled my four-year stay in Aachen. My sincere appreciation also goes to the CBI at RWTH Aachen for offering me a work contract to extend my stay for an additional six months, allowing me to focus entirely on my dissertation.

I am profoundly thankful to Prof. Dr. habil Rostislav Chudoba for providing me with the opportunity to work on this project and for his exceptional guidance and mentorship. His trust in my abilities, along with his unwavering support, kindness, and friendship, greatly enriched my academic and personal growth during my time in Aachen. I am particularly grateful for his constructive feedback and insightful suggestions, which significantly enhanced the quality of my work. I would also like to thank Prof. Dr. Josef Hegger for his consistent support and encouragement throughout my research.

I owe a special debt of gratitude to Dr. Abedul Bakhteer for his unwavering guidance and support, which helped me navigate the challenges of this journey. I am also grateful to Homam Spartali and Mario Aguilar Rueda for their valuable advice in honing my programming skills. A heartfelt thanks goes to my colleagues and friends, Jan Philip Schulze-Ardey, Jan Ungerman, Annkathrin Sinning, Benjamin Camps, and Maximilian Schmidt, for their camaraderie and for the many memorable moments and gatherings that made me feel at home in Germany while deepening my understanding of its rich culture.

I am particularly thankful to my close friends, whose support and encouragement during the final weeks of my thesis were a source of immense strength. They stood by me when I was racing against time and struggling to keep up with the demands of this endeavor. I am especially grateful to Zack Jafer, Harshit Mishra, Ekaterina Plekhanova, Alana Bestaeva, Jonas Schumacher, Diren Kaygisiz, Murad Bayramli, Shubham Verma, and Gülben Micik for their unwavering encouragement and friendship during the last few months of my doctorate.

I would also like to extend my appreciation to my flatmates, who offered emotional support during some of the most challenging times of my research. In particular, I want to thank Hamza Ikram, Lourdes Camarma, Khalid El Maghawry, Despoina Skempi, and Sophie Ostermann for their kindness and encouragement throughout my stay in Germany.

Lastly, and most importantly, I dedicate this degree to my parents, Uzma Seemab and Seemab Iftikhar, and my sister, Tazeen Seemab. Their unwavering love and support have been the foundation of my success. My mother stayed awake late into the night to ensure I woke up early to study as a child, and my father worked tirelessly to provide for my education during my formative years. Watching their hard work and sacrifices instilled in me the motivation to pursue my dreams with passion and determination. Though the journey was not without challenges, their prayers, encouragement, and unconditional support gave me the strength to persevere. I am forever grateful to them for everything they have done to make my achievements possible and dedicate this degree to their love and sacrifices.

Fahad Seemab

Aachen, October 2024

Contents

Nomenclature

The most important units and formula symbols are listed below. Unlisted symbols are explained in the text.

Units

Force	N, kN
Stress	N/mm^2, MPa
Strain	%, ‰
Length	mm, cm, m
Area	mm^2
Time	sec, min
Angle of rotation	°

Lower-case Latin letters

n_I	Nodal positions
n_T	Number of DIC snapshots
f_t	Tensile strength of concrete
f_c	Compressive strength of the concrete
w	Crack opening
w_cr	Critical crack opening
d_ag	maximum size of aggregate
s	Crack slip
f_y	Yield strength of the longitudinal reinforcement respectively
b_n	Net width of the beam
b	Width of the specimen
n	Number of reinforcing bars
c_m	Minimum concrete cover
l_{ef}	Effective length of concrete
b_{ef}	Effective width per bar
s_b	Spacing between bars
c_b	Concrete cover under the bars
k_b	Strength reduction factor
p	Perimeter of steel reinforcement

c	Distance of the neutral axis from the top face of the beam
a	Shear span
l_B	Length where the tributary flexural cracks
x	Horizontal axis
y	Vertical axis
f	Body forces
l_{ch}	Characteristic length
$\mathrm{a_c}$	Equivalent crack
$\mathrm{a_0}$	Initial crack
f_2	Geometry factor
f_1	Geometry factor
z	Lever arm
x_{ak}^{fps}	Tip of the fracture process zone
x_{an}^{tip}	Tip of the pre-existing process zone
t_{ak}	Line vector of the fracture propagation segment
x_{ak}^{rot}	Unknown center of rotation
x_{0k}^{fps}	Horizontal position of the tip of the fracture process zone segment
x_{1k}^{rot}	Vertical position of the center of rotation
$x_{ak}^{\mathrm{tip},\varphi}$	Rotated position of the tip of the crack
p_a	Vector connecting the rotation center with the current crack tip on the fixed and rotated plate
q_a^{ξ}	Vector connecting the rotation center with the current crack tip on the fixed and rotated plate
x_{La}^{1}	Rotated position of a point on the ligament L
$x_{\mathrm{L}a}^{0}$	Node on the line of the ligament running through the cross section with L segments
x_a	Crack positions
x_{Ia}	Nodal positions
x_{fpz}	Horizontal distance from clamping moment to the position of force contribution from fracture process zone
z_{fpz}	Vertical distance from clamping moment to the position of force contribution from fracture process zone
x_{da}	Horizontal distance from clamping moment to the position of force contribution from dowel action
z_{da}	Vertical distance from clamping moment to the position of force contribution from dowel action
$x_{\mathrm{V,agg}}$	Horizontal distance from clamping moment to the position of force contribution from aggregate interlock action
z_{agg}	Vertical distance from clamping moment to the position of force contribution

	from aggregate interlock action
z_{Fs}	Vertical distance from clamping moment to the position of horizontal force contribution at steel reinforcement

Upper-case Latin letters

X_{TPa}	History of position of all points
U_{TPa}	History of displacement fields of all points
F_T	Load levels
L_a	dimensions of rectangular grid
X_{aIJ}	Position array of grid coordinates
X_{aEiFj}	Element-wise indexed arrays of nodal coordinates
U_{TEFia}	Element-wise indexed arrays of nodal displacements
J_{EmFnas}	Jacobi matrix in each element E,F and material point m,n
$B_{EiFjmnabc}$	Kinematic operator mapping the displacement to strain field at all quadrature points
X_{aEmFn}	Global positions of quadrature points
C	Index of a detected crack
X^{tip}_{Ca}	Intermediate position of crack tip
U^{left}_{aCN}	Global displacements on the left side of the crack
U^{right}_{aCN}	Global displacements on the right side of the crack
T_{CNab}	Coordinate rotation operators
T^{l}_{Cab}	Coordinate rotation operators
X_{Cpa}	Band of points on the right plate along a crack
$X^{\ell_0}_{Cpa}$	Reference system on the left side of a crack
$X^{\ell_\lambda}_{Cpa}$	Reference system on the left side of a crack
$U^{\ell_\lambda}_{Cpa}$	Local displacement vectors
X^{mid}_{Cpa}	Midpoint positions
X^{line}_{Cpa}	Lines perpendicular to the displacement of individual points
W_{Cpa}	Radial vector of rotational movement
G_{f}	Fracture energy
G_{f0}	Base value of the fracture energy
A_y	Contact areas between aggregate particles and cement matrix perpendicular to the crack surface
A_x	Contact areas between aggregate particles and cement matrix parallel to the crack surface

$\mathrm{V}_{\mathrm{da(I)}}$	Transfer of shear force as a result of concrete tensile strength along the longitudinal reinforcement
$\mathrm{V}_{\mathrm{da(II)}}$	Transfer of shear force due to deformation of the longitudinal reinforcement
A_s	Area of steel
E_f	Modulus of steel reinforcement
A_f	Area of reinforcement
E_c	Elastic modulus of concrete
L_c	Characteristic length
$\mathrm{M}_{\mathrm{ext}}$	External moment
E_s	Modulus of elasticity of steel
R_{kl}^{β}	Transformation matrix
R_{kl}^{θ}	Transformation matrix
K_I	Mode I stress intensity factor
K_{II}	Mode II stress intensity factor
$S_{ij}^{I}(\theta)$	Angular function from Irwin's approximation
$S_{ij}^{II}(\theta)$	Angular function from Irwin's approximation
T	T-stress
R	Crack driving force
G_c	Critical fracture energy
$K_{I\mathrm{c}}$	Critical stress intensity factor
CTOD_c	Critical crack tip opening displacement
M_x	Bending moment
M_{CA}	Clamping moment
$\mathrm{V}_{\mathrm{cr,m}}$	Cracking shear force
L^{fps}	Length of the fracture process zone segment
H	Height of beam
L_c	Characteristic length
P	Principal stresses
D	Eigen values
M_{Ca}	Clamping moment
V_{fpz}	Shear force contribution from the fracture process zone
V_{agg}	Shear force contribution from the aggregate interlock action
V_{da}	Shear force contribution from the dowel action

Greek letters

α	Kinematic hardening state variable

$\tilde{\alpha}$	Relative crack length
ΔX_a	Horizontal and vertical distances between nodes
$\mathcal{G}_{aIJ}$	Index mapping of grid points
η_a	Parametric coordinates
ξ_{aij}	Element corner coordinates
δ_{rs}	Kronecker delta
$\mathcal{H}_{aEiFj}$	Index map of elements and their nodes
$\varepsilon_{TEmFnab}$	Time-space grid of strains
ε_{o}	Onset of inelasticity
ε_{f}	Initial rate of damage response
ω	Damage variable
λ	Load factor
$\omega_{\lambda MN}$	Values of damage on interpolated grid
$\bar{\omega}$	Predefined damage threshold
Δx	Distance between crack ligament and the points on each side of the crack
ΔU_{aCN}	Global displacement jumps
ΔU^{ℓ}_{bCN}	Local displacement jumps
σ_{fpz}	Stress resultant of the fracture process zone
σ_{ag}	Normal stress resultant from the aggregate interlock
σ	Stress resultant in the compression zone
σ_x	Normal stress at crack tip
τ_{ag}	Tensile stress resultant from the aggregate interlock
τ_z	Shear stress at the crack tip
μ	Friction coefficient
σ_{pu}	Yield strength of the cement matrix
ϕ_s	Diameter of the reinforcement
(ε_s)	Increasing strains in the longitudinal reinforcement
τ	Bond stress
α_1	Empirical calibration constant
α_2	Empirical calibration constant
ε	Normal strain in the longitudinal reinforcement
ρ	Reinforcement ratio
$\bar{\sigma}_{ij}$	2D stress state
$\bar{\sigma}$	Far field stress
η	Coefficient acting as a switch whose value range from zero to one to constitute the cases from pure tension to pure shear
β	Initial crack inclination angle
$\bar{\sigma}^{\beta}_{11}$	Normal local stress state at the tip of the crack

$\bar{\sigma}_{12}^{\beta}$	Tangential local stress state at the tip of the crack
θ	Crack operation angle
ψ	Propagating crack angle
ι	complex function
σ_{∞}	Stress state
$\Delta \mathrm{a_c}$	Effective crack extension
α	Pre-critical stable crack growth
xi	Vector normal to the fracture propagation segment depending on the crack orientation angle ψ and slip of the crack segment
ℓ	Incremental extension of the crack propagation segment
γ	Level set function
ΔF_{s}	Force difference in between concrete teeth
ε_{abc}	Levi-Civita symbol

Indices notations

a,b,c,d	Spatial coordinates $[a,b,c,d \in (0,1)]$
I,J	DIC grid nodal coordinates $[I \in [0,n_I-1])$ and $J \in [0,n_J-1]]$
P	Index of points within DIC field $[P \in [0,n_P-1]]$
E,F	Element indexes $[E \in [0,n_I-2], F \in [0,n_J-2]]$
M_{C0}	Indexes of the peak values $[M_{C0} \subset [0,n_M-1]]$
K,L	Finite element grid indices $[(E,i) \rightarrow K$ and $(F,j) \rightarrow L]$
m,n	Quadrature points of FE $[m,n \in [0,1] \times [0,1]]$
i,j	Finite element nodes $[i,j \in [0,1] \times [0,1]]$
r,s	direction of the parametric coordinate η $[r \in [0,1], s \in [0,1]]$
ω	damage variable $[\omega \in [0,1]]$
λ	time history index $[\lambda \in (0,1)]$
T	time history index $[T \in (0,n_T-1)]$
C	crack index $[C \in [0,n_C-1]]$

Abbreviations

COR	Center of rotation
DCDT	Damage based crack detection tool
CMOD	Crack mouth opening displacement

CTOD	Crack tip opening displacement
DIC	Digital image correlation

Operators

$(.)^+$	Positive part of a tensor
$\mathrm{tr}(.)$	Trace of a tensor
$\mathcal{R}()$	Response surface of parameters
$H()$	Heaviside function

1 State of the art

1.1 Introduction

Over the past century, there has been a lot of research done on the shear strength of beams and one-way slabs. Even so, it might be difficult to characterize the shear behavior of reinforced concrete elements without shear reinforcement. The topic's importance stems from the wide range of situations in which the shear strength of cracked concrete without transverse reinforcement can serve as the primary design factor for reinforced concrete beams. This holds true for all realistic applications (i.e. beams, retaining walls, shells, footings, one-way and two-way slabs etc.). The code requirements for shear design have been relied on empirical expressions calibrated on the basis of the available test data for many years due to the intricacy of the design phenomenon [Committee, 2008, EN, 1992]. Problems arise when these empirical formulas are used outside of their calibrated range, leading to potentially unsafe outcomes. [Collins and Kuchma, 1999, Muttoni, 2008]. Many correction factors have been added on a continuous basis to increase its validity. [Committee, 2008]. The actual structures, however, differ greatly from the results obtained in the lab under ideal conditions. As a result, the addition of correction factors does not guarantee the safe applicability of empirically derived design formulas, necessitating a conceptual understanding of the mechanical background for shear design.

The observed limitations of the empirically derived equations allowed researchers to focus on the physical understanding of the test results in order to propose suitable mechanical models for shear behavior design in practical cases. The publication of "The riddle of shear failure and its solution" in 1964 drew a lot of attention from the scientific community, motivating many researchers to look for mechanical explanations for the shear failure phenomenon. Different mechanical models in the literature exhibit conceptual differences. This can be concluded with the fact that there is still no consensus on the governing mechanism causing shear failure. Crack localization and propagation of shear cracks in RC structures without shear reinforcement represents a complex problem with many interacting influence factors. The need for a rigorous understanding of the governing mechanisms posed several burning question to the scientific community. Assessment of existing reinforced concrete structures have gained notable interest in the last few decades. In this regard, deeper knowledge of the crack behaviour is vital for the conceptual understanding of the nonlinear response of structural concrete. Extensive research in this field has led to the development of several mechanical models that can support the design process. However, the validity of the modeling approaches is still a subject of an ongoing, intense discussion within the community.

1.2 Shear zone models for RC beams

1.2.1 Smeared crack models

Numerical finite-element models of reinforced concrete beams used in engineering practise represent the crack development as localized bands of high strains. Even though, these models can fairly well predict the load deflection response in some configurations [Tambusay et al., 2021], they cannot explicitly capture load carrying mechanisms developing along the localized crack, namely the aggregate interlock and dowel action.

1.2.2 Cohesive crack models

An explicit inclusion of a propagating discontinuity into the finite element discretization has become possible using the extended finite element method [Belytschko and Black, 1999, Roth et al., 2015, Faron and Rombach, 2020, Baktheer et al., 2024b, Baktheer et al., 2024c]. With a discrete representation of a localized crack it became possible to explicitly reflect the evolving crack width and slip across the crack faces. To extend this types of models with stress transfer mechanisms acting across the crack, experimental data are required that can validate the evolution of the crack kinematics on a broad scale of stress and geometry configurations.

Besides numerical finite element models, several analytical models have been introduced at the level of the shear crack ligament, based on the cross-sectional equilibrium of the stress resultants, i.e. bending moment, normal force and shear force. These models introduce constitutive assumptions to relate the stress transfer across the ligament to the kinematic variables along the crack ligament, namely the opening and sliding of a localized crack in the tensile zone and the assumed strain tensor profile in the compression zone [Vecchio and Collins, 1986, Reineck, 1991, Cavagnis et al., 2018b]. Recently, this ligament based equilibrium solution was applied also for the steel fiber reinforced concrete beams without shear reinforcement [Bi et al., 2021]. The crack kinematics of these models, delivering the profiles of crack opening and crack sliding along the crack path, is predetermined through the chosen crack shape in the state of shear failure. An incremental ligament based model has been introduced by considering an additional vertical equilibrium condition in the fracture process zone of a concrete tooth. This ligament based models can simulate the crack propagation process and predict the crack shape at ultimate state [Classen, 2020].

1.2.3 Effect of energy release

As pointed out by [Donmez and Bazant, 2018], a significant effect to be considered in a rigorous modeling of the shear zone is the interplay of the energy dissipation mechanisms during the crack propagation. Recalling the phenomenology of the fracture mechanics, the authors demonstrate that the crack propagation process and the ultimate load is strongly affected by the ratio of the energy dissipation rate owing to the elastic unloading and to the fracturing. This ratio does not remain constant for different sizes of a structure. The reason is that the elastically stored energy grows quadratically and the fracture energy only linearly with the size of the structure. This phenomenon is not implicitly covered by all models formulated at the ligament level.

1.3 Development and limitations of cohesive crack models

1.3.1 Critical shear crack theory

The theory was introduced for the first time in 1991 [Muttoni and Schwartz, 1991] and can be applied to the design of one- and two-way shear slabs [Muttoni and Fernández Ruiz, 2008, Muttoni, 2008] with or without transverse reinforcement or fibers. This theory's design equations have also been incorporated into the fib Model Code 2010 [Code, 2010]. According to the theory, the shear strength of reinforced concrete members without transverse reinforcement is determined by the opening and sliding of a critical shear crack [Muttoni and Fernández Ruiz, 2008]. The following are the main CSCT postulates:

1. The development of the critical shear crack governs the shear strength.
2. The profile of opening and sliding of the crack varies throughout the height of the cross section and is dictated by the kinematics of the crack, under the assumption that the center of rotation characterizing the relative displacement is positioned at the tip of the crack.
3. Shear forces can be carried by various shear transfer actions such as aggregate interlock, dowel action, residual tensile strength of concrete and the inclination of the compression chord.
4. Shear Transfer by each shear action can be calculated using equilibrium, kinematics, and the constitutive laws of materials.
5. When shear demand equals the capacity of a free body defined by the critical crack to transfer shear forces, failure occurs, i.e.

   $$V_R = V_a + V_r + V_d + V_c \tag{1.1}$$

   where, V_a, V_r, V_d, V_c are the force contributions from aggregate interlock, residual stresses, dowel action and compressive forces respectively.

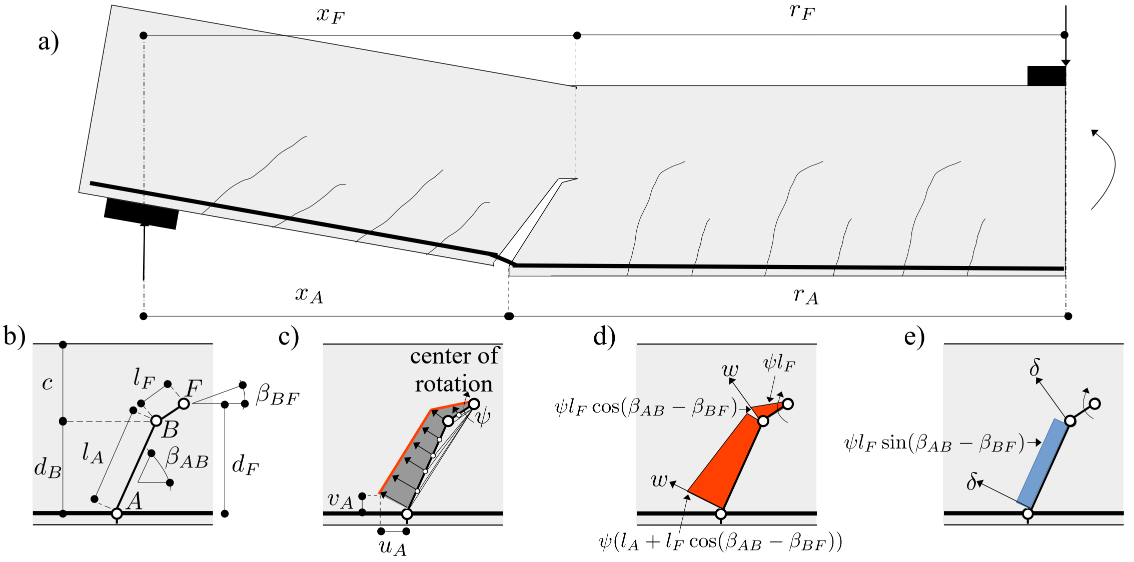

Figure 1.1: Critical shear crack theory (CSCT) [Muttoni and Fernández Ruiz, 2019]

The theory postulates that the critical crack can develop at any given section and can be characterized by a bilinear shape (Fig. 1.1a). The CSCT-adopted length and angles for shear crack characterization (Fig. 1.1b) were carefully validated by comparison to test findings. After that, the entire profile of the opening and sliding along the height of the cross section is calculated based on the assumption on the crack's shape and its kinematics (i.e. considering two rigid bodies separated by a critical crack with the location of center of rotation at the crack tip) (Fig. 1.1(c-e)) [Muttoni and Fernández Ruiz, 2019].

In this theory, the width of the critical crack is assumed to be proportional to the reference longitudinal strain, such that:

$$w \propto \varepsilon \cdot d \tag{1.2}$$

where, d represents depth of the cross section up to steel reinforcement. On the basis of the assumption in CSCT, the developed failure criterion reads as:

$$V_c = \frac{bd\sqrt{f_c}}{3} \frac{1}{1 + 120\frac{\varepsilon_d}{d_{g0}+d_g}} \text{ [MPa, mm]} \tag{1.3}$$

here, b, f_c represent the width of the beam and the compressive strength of concrete. The decay in the shear transfer action is governed by $(\varepsilon_d)/(d_{g0} + d_g)$ which is associated to concrete properties (i.e. cracked concrete response and the roughness of the crack lips) and to the reference shear crack width [Muttoni and Fernández Ruiz, 2019]. Furthermore, to calculate the shear resistance, a linear-cracked response of reinforced concrete in bending is assumed. Therefore,:

$$\varepsilon = \frac{M}{bd\rho E_s(d - c/3)} \frac{0.6d - c}{d - c} \tag{1.4}$$

where, M, ρ, E_s represents the moment, reinforcement ratio and modulus of steel respectively. For further reading about the model refer to the critical shear crack theory presented in [Muttoni and Fernández Ruiz, 2019].

1.3.2 Shear crack propagation theory

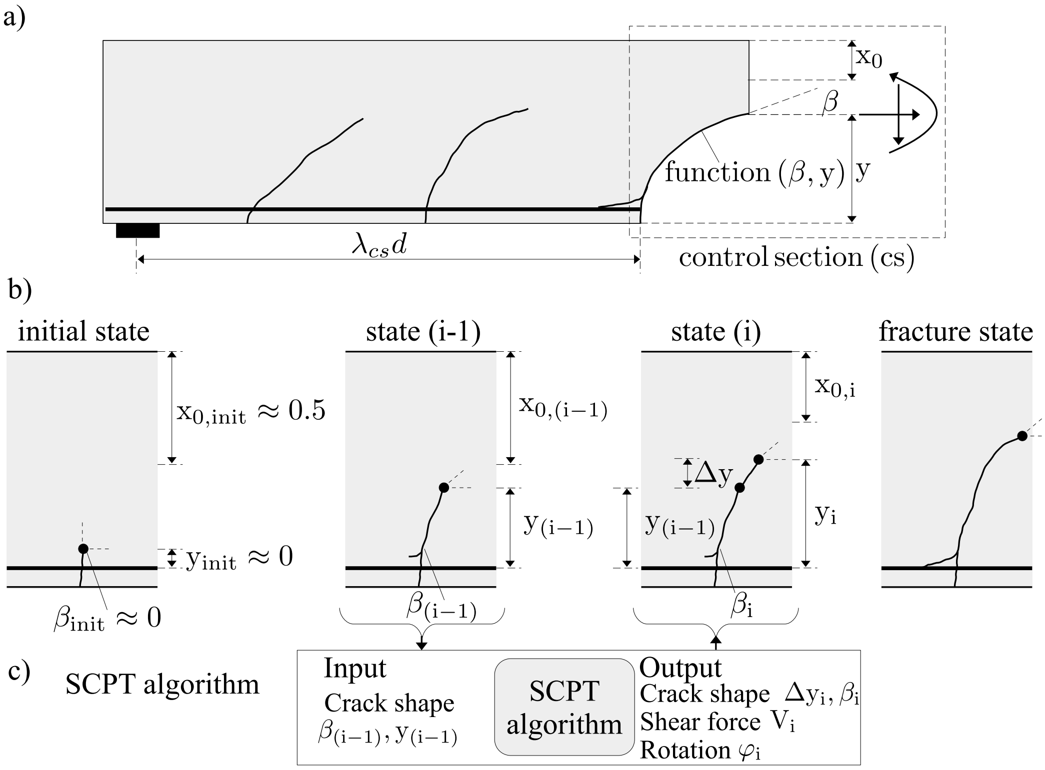

Figure 1.2: Incremental procedure of Shear crack propagation theory (SCPT) [Classen, 2020]

The theory came forward in 2020 [Classen, 2020]. SCPT proposes an incremental procedure to analyze the entire shear loading process including the crack propagation up to the failure state (see Fig. 1.2). A control section of the procedure consists of the curved crack path and a vertical segment through the uncracked section up to the crack tip [Classen, 2020]. Before the instantaneous method begins, the instantaneous geometry of the crack is already known (i.e at the steel reinforcement). The algorithm uses this state (i-1) as an input. The method then determines, for a specific reduction in the compression zone depth, the crack propagation angle β and the vertical dimension of the crack propagation length Δy. Consequently, the algorithm outputs the crack shape, the rotation of the control section, and all internal forces over a predetermined length of the compression zone depth. This output data then serves as an input for the calculation of step (i+1) in the loading process. SCPT also takes into account the biaxial shear crack propagation criterion (cohesive crack approach by Hillerborg combined with Kupfer's criterion) in which the condition for the fracture process zone to propagate depends on the stress-strain behavior of the continuous concrete at the crack tip. Furthermore, the case of cantilever action is included to account for the vertical stress state at the crack tip. Because of its level of complexity and iterative incremental procedure, the SCPT necessitates high computational efficiency. More information on the theory can be found in [Classen, 2020].

1.3.3 Problem statement

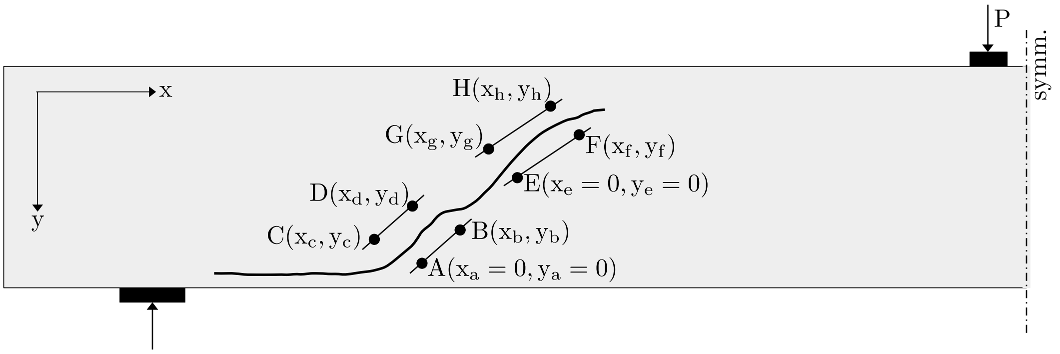

Figure 1.3: Parallel line pairs, located above and below the diagonal cracks for COR calculation [Abdullah Dönmez et al., 2020]

The development of these analytical models to comprehend the mechanical background underlying the shear failure phenomenon gave rise to doubts regarding the validity of certain assumptions and results. The role of interacting effects within the critical crack is one such topic of discussion. The CSCT claims that aggregate interlock governs shear failure within the shear crack. However according to SCPT, the contribution of uncracked section is much more during the initial phases of the loading history, which is thereafter surpassed by the dowel action. According to this theory, aggregate interlock appears to govern only in the later stages, after its activation and just prior to the ultimate condition of failure. The CSCT's conclusions about the aggregate interlock contribution to shear failure are criticized in [Abdullah Dönmez et al., 2020], where the aggregate interlock stresses appear to be minimal and are overwhelmed by enormous compressive stresses above the crack tip. In addition, another crucial conclusion is that the normal and shear stresses reported from CSCT near the fracture tip are unrealistic and contradict FE analysis. The location of the center of rotation dictating the rigid body's rotation about the crack tip is also a subject of discussion. CSCT considers the center of rotation (COR) to be at the crack tip, whereas SCPT considers the COR to be a small distance vertically above the crack tip as long as the propagated crack tip is in the tension zone. However, as the crack propagates into the compression zone, the location of COR shifts vertically below the crack tip. In citation [Abdullah Dönmez et al., 2020], an experimental investigation was conducted to verify both of these CSCT and SCPT presumptions. For this, two initially parallel line pairs, $\overline{AB} - \overline{CD}$ and $\overline{EF} - \overline{GH}$ (see Fig. 1.3) are anchored on both sides of diagonal cracks in zones of least nonuniform deformations. The corresponding inclination angles are computed using FE analysis. The study shows that the distance of centers of relative rotation from the crack tip is in the order of 100 m or more. Furthermore, it is claimed that by placing these parallel line pairs closer to the region exhibiting nonuniform strains, the location of the center of rotation can be found closer to the crack tip. Moreover, this study questions the verification of rigid body rotation with the observation that the masses on the crack planks move apart in almost translatory motion that is restrained by the longitudinal reinforcement at the crack mouth and is lead by expansion of compression crushing zone above the crack tip [Abdullah Dönmez et al., 2020]. The findings also raise question on the validation of the hypothesis with the DIC measurements as the strain field near the crack is nearly nonuniform and variable. The aforementioned issues that were brought up in the scientific community provided the impetus and opened the door for research in this area and the reporting of the findings that are being made in this thesis.

1.4 Sensing of discrete material degradation events

1.4.1 Thermography

For the crack detection in thermo-sensitive materials, an infrared (IR) thermography based method that uses IR image rectification with the extraction of isotherms for the detection as well as geometric characterization and orientation of cracks to predict its direction of propagation is elaborated in [Rodríguez-Martín et al., 2016]. Thermal cameras that uses specular reflection to identify the defects in Si solar cells is presented in [Brooks et al., 2015]. Laser excited thermography has also been used for crack detection in [Pei et al., 2016]. Another example of an IR based crack identification procedure with ultrasonic IR thermography adopted for aluminium parts is given in [Guo and Vavilov, 2013]. An IR thermography image rectification technique, for detection of cracks using the notches is also presented in [Broberg, 2013].

1.4.2 Ultrasonic sensing

An application of a hybrid system combining laser, ultrasonic scanning excitation, and piezoelectric air coupled sensing technique for the crack detection in aluminium specimens has been described in [Dhital and Lee, 2012]. An example of crack identification procedure employing ultrasonic sensing to concrete specimens has been reported in [Wolf et al., 2015]. Here, the presented results indicate that acoustic emission is the most sensitive method for the degradation events in the concrete material structure. A method based on ultrasound has also been developed to determine the depth of cracks [Pascale and Lolli, 2015]. Using ultrasonic, a multi-synthetic aperture focusing approach was established in [Shirahata et al., 2014] to observe the closure and opening of crack tips, which are significant for longer cracks. DIC in combination with Acoustic Emission, and Ultrasonic Pulse Velocity was used to highlight the time and location of the crack [Iliopoulos et al., 2015].

1.4.3 Acoustic emission

Degradation events inside a specimen, including their position can be measured using acoustic emission methods as presented in [Alam et al., 2015]. This technique, together with ultrasonic pulse and digital image correlation have been used simultaneously for volume and surface monitoring of RC specimens in [Iliopoulos et al., 2015]. Another class of material degradation monitoring method called Time of Flight Diffraction (TOFD) has been used in [Merazi Meksen et al., 2010]. Recently, for the inspection of building pathologies, unmanned aerial vehicles were also used as an effective tool in combination with some image processing algorithm for crack detection in the building structures [Pereira and Pereira, 2015].

1.5 Surface monitoring of the cracking process

1.5.1 Line sensors

The monitoring of the crack propagation process during tests has been, and in most cases still is, performed by visual inspection. In the earlier days, estimation of the opening of the selected cracks using visual inspection was obtained by comparison with printed line widths. The manual inspection procedures for crack detection has its own limitations such as the sketch of the cracks were prepared manually and this procedure solely relied on the specialist's experience and knowledge with the equipment. Furthermore, these methods lack objectivity in the quantitative analysis [Mohan and Poobal, 2018]. Hence, with the advancement of technology, this technique has been replaced and now linear variable displacement transducers (LVDT's) and optical systems are employed extensively for crack detection due to their high accuracy.

1.5.2 Pixel based image processing

Pixel intensities have been used by many researchers to develop automated crack detection algorithms. Such optical methods have gained more popularity than the visual inspection methods as they are more objective and can be automated [Mohan and Poobal, 2018]. Different image based crack detectors have been presented in the literature which are conceptualized upon thresholding, morphological operations or deep learning techniques [Cha et al., 2017, Islam and Kim, 2019, Li et al., 2018, Liu et al., 2019, Luo et al., 2019, Yang et al., 2018]. A crack detection algorithm for glass has been proposed based on digital image processing in [Yiyang, 2014]. Gabor filters were used for automatically distinguishing cracks in digital images [Salman et al., 2013]. Sabor filtering and otsu's method have also been employed for automated crack identification [Talab et al., 2016]. The study investigating the pre- and postcracking shear behavior of reinforced concrete beams using laser interferometry and photogrammetry, revealing nonlinear pre-cracking stress distributions and limited post-cracking shear friction in low and high shear reinforcement ratios can be found in [Hegger et al., 2004].

1.5.3 Digital image correlation

With the recent advancement in digital image technology providing digital image correlation (DIC) methods and tools, the development of a new class of crack detection methods has been triggered. This method is used to analyze 2D and 3D displacement fields and requires high resolution cameras for detailed acquisition of the history of displacement fields. These displacement fields have been employed to develop crack detection tools. Examples of obtaining continuous displacement fields from DIC can be found e.g. in [Hild et al., 2002, Besnard et al., 2006].

1.5.4 DIC applications

A pioneering application of DIC has been presented in [Choi and Shah, 1997] to monitor the microscopic cracking process between aggregates and the cement matrix in a specimen loaded in compression. Applications of DIC used to monitor the displacement and strain fields on a limited portion of various structures and materials e.g. in masonry walls [Tung et al., 2008], on the surface of FRP bonded to masonry [Ghiassi et al., 2013] and on the surface of RC specimens strengthened with composite plates [Muller et al., 2004] are also present in literature. Some applications of this technique on full scale structures also exist i.e., use of DIC for crack monitoring on a RC bridge beam, both *in situ* and in laboratory static load test [Küntz et al., 2006] and identification of multiple cracks propagating through a RC slab [Helm, 2008].

1.5.5 DIC and manual crack characterization

The potential usage of DIC for shear crack measurement is already well known in the scientific community. The usage of DIC to track displacement fields and the cracking patterns can be seen in [Cavagnis et al., 2018a]. Furthermore, another model where the crack kinematics is obtained via DIC measurements and the relevant shear transfer interaction mechanism is acquired by using existing constitutive laws is given in [Huber et al., 2016]. One more method for the extraction of crack kinematics using DIC is presented in [Cantone et al., 2022]. A detailed study on the crack development and obtaining the contribution of interacting effects using existing constitutive laws within a shear zone by using DIC imaging is performed in [Adam, 2021a].

1.5.6 DIC and crack detection using 1D strain-field

Manual extraction of the crack characteristics from the DIC data by the specification of virtual reference points at both sides of a crack can be tedious and can result in a loss of important information. In order to increase the objectivity of the characterization, an automated crack path identification procedure has been proposed for tensile tests of reinforced specimens [Mündecke and Mechtcherine, 2020]. In this techniques, several horizontal measuring lines are analyzed to detect points of the crack on the basis of the local maxima in the distribution of horizontal strains. A strain peak picking along a horizontal direction has also been used in an algorithm proposed in [Ruocci et al., 2016]. However, the application of these methods is limited to simple crack patterns (i.e., non-branching cracks). Furthermore, the model is also unable to take into account the local rotations of the tested specimen. The development of an experimental approach that combines digital image correlation, fiber optic sensors, and strain gauges, enabling the visualization of fatigue damage progression in compression zones, is detailed in [Becks et al., 2023, Baktheer et al., 2024a]. Another study on the application of fiber optic sensing (FOS) in textile-reinforced concrete (TRC) is presented in [Becks et al., 2022]. Additionally, a study on an FOS Evaluator—a Python-based software developed to enhance the processing and analysis of distributed fiber optic sensing (DFOS) data, facilitating more comprehensive structural monitoring in civil engineering applications is available in [Janiak et al., 2023].

1.6 Crack path as an evolving geometrical entity

Manual extraction of crack characteristics from images using analysis software is tedious, time consuming and can lead to loss of important information as only selected points of certain chosen cracks can be measured [Koščak et al., 2022]. These aforementioned limitations can be overcome by implementing automatic crack detection algorithms based on DIC measurements.

1.6.1 DIC based crack detection using 2D strain-field

A more general approach for automated crack detection has been proposed in [Gehri et al., 2020]. This refined approach uses well established methods of image processing to detect the skeleton of the crack pattern. The identified cracks are represented as thin traceable lines in areas with principal strain values above a certain specified threshold. The algorithm was found to be in a good agreement with the visually observed crack patterns. The method works well for non-branching and well separated cracks but the crack detector fails for very closely spaced cracks due to overlapping high strain areas. A detailed insight on the development of the crack detection scheme is reported in the upcoming section (Sec. 1.7).

1.7 Development and limitations of DIC based crack detection schemes

1.7.1 Overview

The optical-photogrammetric measurement technology known as Digital Image Correlation (DIC) enables the detection of surface deformations. Comparing the characteristics of the loaded and unloaded surface conditions allows for the recording of deformations. In recent years, DIC measurements have been widely employed to examine concrete constructions [Adam, 2021b, Görtz, 2004, Herbrand, 2017, Hillebrand, 2023, Teworte and Hegger, 2014, Baktheer and Becks, 2021]. One such approach for crack assessment using DIC and Noise-filtering is presented in [Ruocci et al., 2016] (see Fig. 1.4). The article offers a method for post-processing DIC readings to evaluate cracks on large-scale constructions. The method generates cracks through a 'peak-picking' procedure. The approach posits that cracks correspond to zones where a discontinuity is noticed in the displacement field. These discontinuities manifest as peaks in the strain field, which is treated as a data set and analyzed by simple moving average. Identification of cracks is achieved by analyzing many horizontal measuring lines independently (see Fig. 1.4). A certain threshold on the strain peaks is automatically defined as the mean value plus one standard deviation $(\nu + \sigma)$ of the longitudinal strain distribution. Any points exceeding this threshold are classified as cracks. Now, the crack paths are assigned by linking several crack points inside user defined search areas. In addition, based on the two-dimensional surface displacement field, the crack widths and slips are retrieved from the information obtained from two reference points located to the left and right of the crack point location. The proposed method had some limitations which are highlighted in [Gehri et al., 2020] (i.e. the crack detection method is direction dependent as only longitudinal deformations are taken into account, the application of the tool is limited to simple and non-branching cracks inside the user-defined searching areas).

On the basis of these aforementioned reasons, another automatic crack detection tool is proposed in [Gehri et al., 2020]. The tool makes use of general formulations for the investigated surface deformations in the two-dimensional plane, enabling the detection

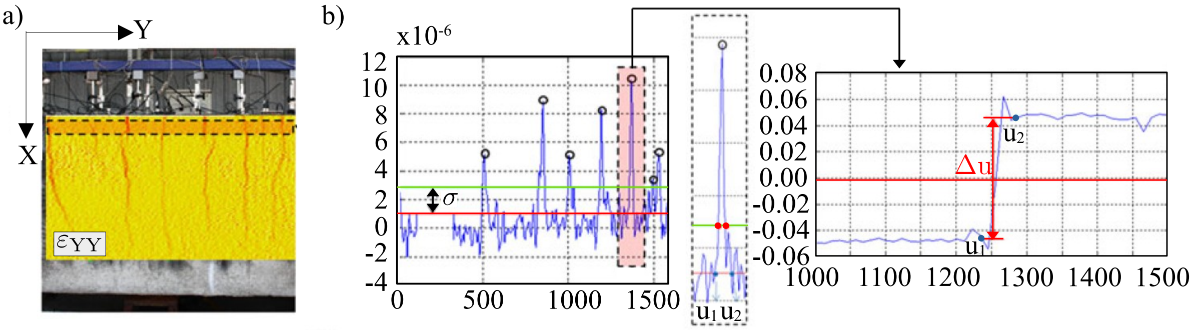

Figure 1.4: (a) Strain field and data windowing, (b) cracks peaks-picking and 1D crack width measurement [Ruocci et al., 2016]

of cracks and the determination of crack kinematics. The proposed crack kinematic measurement technique can also handle the tested specimen's local rotations, which is critical for crack slip measurement. The cracks are extracted as skeletons using well-established image processing methods. The DIC principle tensile strain field is used in this method. As a result of the detected cracks being directly linked to the measured surface deformations, much finer cracks and more reliable crack locations can be extracted. A brief overview of the conceptualization of the automated crack detection measurement tool (ACDM) can be visualized in Fig. 1.5. The DIC system extracts the full displacement field from the specimen surface. The principal tensile strain field is computed using this acquired data and serves as an input for the crack detection algorithm. Cracks are detected in areas where strains exceed a certain threshold. Morphological thinning is then used to extract crack entities as thinned lines connected to skeletons. Following that, the crack kinematics are measured using a method for calculating the relative displacements of the crack lips and determining the local crack inclination (i.e. crack opening and sliding) (see Fig. 1.5).

Recently, a mechanical model based on the cutting-edge measuring method utilized to derive the real strain field from reinforced concrete members has been developed [Cantone et al., 2022]. This tool tracked displacement fields by combining conventional measurements (e.g., LVDTs, inclinometers) with DIC. The resultant displacement field allowed for horizontal and vertical displacements at each point where rotation and shear strains described the average flexural and shear strains of the cross section. The conclusion of the paper is that the kinematical considerations of the Critical Shear Crack Theory (CSCT) can reproduce the observed strain field distribution effectively.

1.7.2 Problem statement

The present thesis is motivated by a number of shortcomings in the proposed crack detection schemes. The noise filtering approach using DIC data [Ruocci et al., 2016] is found to work only for simple and non-branching cracks. The method has direction dependency since it only considers longitudinal deformations, and as a result, it can only identify cracks that have their major opening component in the longitudinal direction. The crack displacement vector and its decomposition into crack width and slip is biased in the regions with local rotations of the specimen. In this procedure, there is no mechanical meaning to the definition of the strain threshold utilized to detect crack tips in a measurement line. Based on these limitations, the application of this method to experiments with more complex cracking behavior is severely constrained, paving the way for the development of an automated crack detection and measurement scheme (ACDM) [Gehri et al., 2020].

ACDM detects non-branching and well separated cracks perfectly, but it fails to detect very closely spaced cracks or regions near crack intersection due to overlapping high strain areas caused by individual or branched cracks. Furthermore, a more accurate

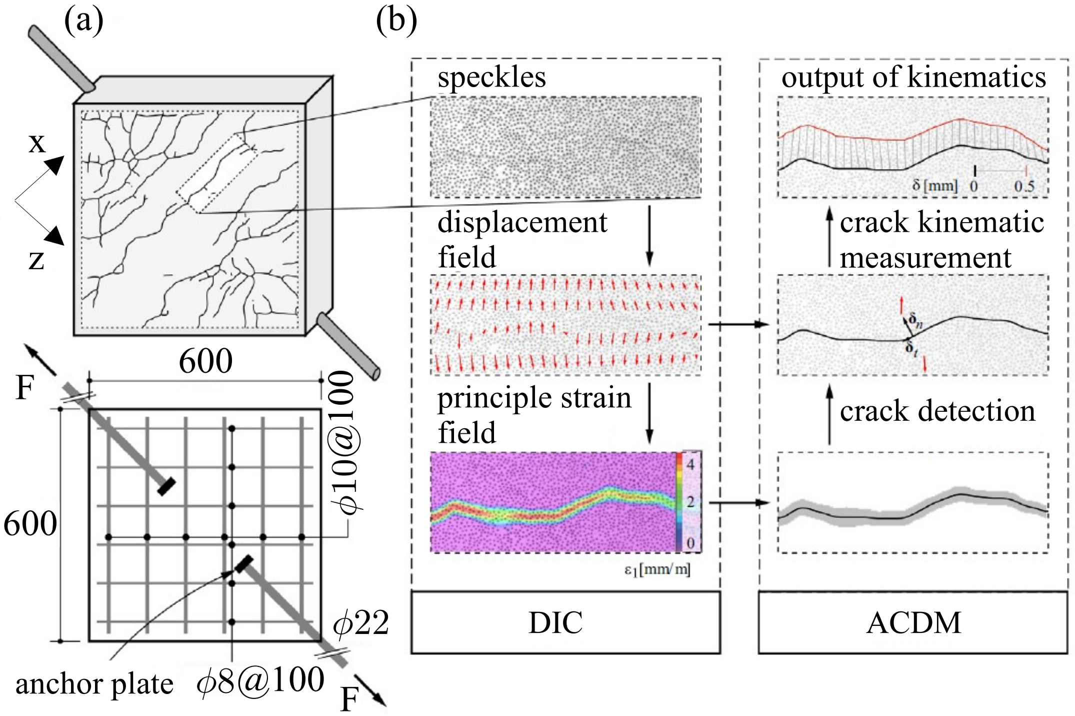

Figure 1.5: Conceptualization of the crack detection and crack kinematic measurement procedure, (a) setup of the experiment, (b) flow hart of the automated crack detection and measurement (ACDM) tool [Gehri et al., 2020]

crack detector that takes into account local variations within the high strain area would improve crack location accuracy, but the crack kinematic measurement at locations with closely spaced cracks and crack intersections may still be biased depending on how the reference points are set up, as noted in [Gehri et al., 2020]. In addition, it was also determined that the regions on both sides of the crack between the crack lips and reference points must move as rigid bodies in order to produce reliable results.

The findings of the mechanical model proposed on the basis of advanced measurement techniques have some reservations about the CSCT assumptions. These reservations were previously discussed in subsection 1.3.3. Based on these constraints, the current thesis proposes the development of a novel crack detection scheme that can serve as a valuable tool in the future not only for crack identification, but also for crack kinematics measurement.

1.8 Characterization of shear cracks

Various specimens exhibit different patterns of cracking, although a number of typical cracks are distinguished based on their shape and origin in [Cavagnis et al., 2015]. Here, we talk about these different kinds of cracks (see Fig. 1.6), such that:

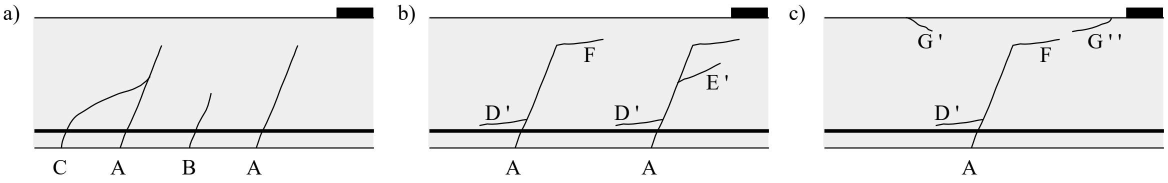

Figure 1.6: Definition of types of cracks propagating in the shear zones [Cavagnis et al., 2015]

- **Type A** cracks are primary cracks and seems to have a bending origin. They are often created early in the loading history and have a high slope.
- **Type B** cracks are secondary cracks and are found to be located in between two primary cracks or near the supports of the specimen. These cracks form at later stages of the loading history and have a lower height than type A cracks. Here, the spacing between the primary and secondary cracks is dependent on the bond condition of the reinforcement and the concrete and also on the amount of reinforcement present inside the structural component.
- **Type C** cracks are either primary or secondary cracks that merge with another primary flexural crack. These cracks develop when crack type A or B propagate at such an angle and distance that it ultimately joins the another crack of type A.
- **Type D’** develop from the surface of the specimen and joins the primary flexural crack A. They are inclined cracks and forms systematically as the crack type A develops. Type D’ cracks mostly start at the level of reinforcement.
- **Type E’** is an aggregate interlock induced crack. It can develop at both sides of an existing crack and usually originates from a primary or a secondary flexural cracks.
- **Type F** cracks are the propagation of the primary cracks within the compression chord. These cracks appear to be rather flat cracks that are originating from a primary crack.
- **Type G’** cracks are formed within the compression chord but have no link to the primary cracks. This type of crack is formed due to the local bending of the compression chord.
- **Type G”** crack develops due to the large shear forces in the compression chord or due to crushing of the compression chord.

1.8.1 Critical shear cracks types

Four different types of critical shear cracks have been found to exist in the literature [Cavagnis et al., 2015]. A brief overview of these cracks is summarized here (see Fig. 1.7):

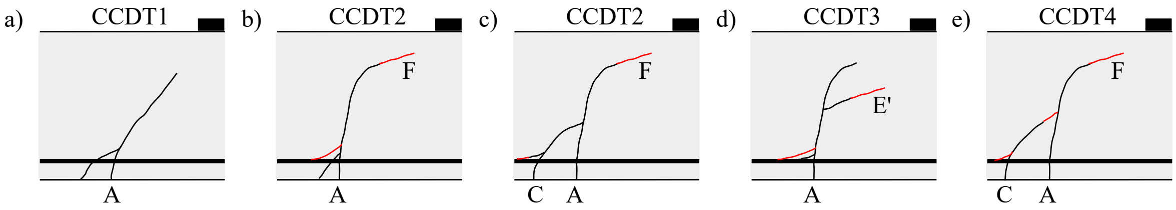

Figure 1.7: Critical shear crack development types (CCDT), (cracks in black refer to increasing load while cracks in red depict the development after maximum load) [Cavagnis et al., 2015]

1. **Critical Crack Development Type 1 (CCDT1)** allows full arching action to develop. This crack is found to develop for specimens with crack propagating at locations such that a direct compression strut is developed without being disturbed by the propagation of the critical shear crack.
2. **Critical Crack Development Type 2 (CCDT2)** is characterized by the development of a quasi-horizontal crack (crack type F) from a primary crack (crack type A) within the compression zone. The propagation of the crack is stable up to failure. In this case, a secondary flexural crack (crack type C) may also emerge along with the primary flexural crack at low load levels followed by a stable growth of crack type F.
3. **Critical Crack Development Type 3 (CCDT3)** emerges due to the propagation of an internal crack that develops due to the aggregate interlock action. The crack develops diagonally (crack type E') from the primary flexural crack (crack type A) as a result of aggregate interlock forces that leads to failure.
4. **Critical Crack Development Type 4 (CCDT4)** appears due to merging of the secondary flexural crack (crack type C) with a primary flexural crack (crack type A). Here, crack type C is found to merge with crack type A-F that leads to an increase in the opening of the critical shear crack and loss of shear-carrying capacity causing failure of the specimen.

1.9 Objectives of the research

The purpose of this thesis is to establish a modeling framework for the realistic investigation of shear crack propagation in longitudinally reinforced concrete beams without shear reinforcement. The following is a summary of the thesis's primary goals:

(1) Development of an effective and automated crack detection technique capable of identifying crack patterns utilizing an anisotropic damage model.

(2) Obtaining realistic crack opening and sliding kinematics from the crack detection tool, hence making the study of crack kinematics independent of the human expertise required for the manual inspection from DIC images.

(3) Assessing the limitations of present constitutive laws with the aid of measured crack opening and sliding values for the purpose of future refinements of the laws.

(4) Development of an effective discrete crack model based on crack propagation criterion that is being governed by the level of stress in the area around the crack tip.

First, we obtain the surface displacements of each node during the course of the loading history, as recorded by the DIC cameras in each image. Following that, finite elements discretization is utilized to estimate strains and stresses based on the triangulated mesh surface displacements. An anisotropic damage model is employed after that to get the damage field, which is then used by the crack detector to find the crack paths. After crack profile prediction, the crack opening and sliding kinematics are found. These will be used as input parameters to analyze the stress distribution along each of the shear cracks present throughout the loading history by applying simple constitutive laws from the literature. Finally, on the basis of the conceptual understanding of the mechanical background governing the shear failure phenomenon, a discrete crack propagation model is being developed.

1.10 Overview of the dissertation

The work on the shear zones project that was carried out at the Institute of Structural Concrete at RWTH Aachen University is documented in this dissertation. German research foundation (DFG) provided funding for the project while the funding of the scholar was from DAAD. The following is a detailed summary of the thesis (see Fig. 1.8):

Part I deals with the explanation of the method to extract surface displacements in the form of triangulated grid from GOM user interface (Chapter 2). The part then continues with the extraction of strains and damage by using finite element and microplane material model respectively (Chapter 3).

In **Part II**, the focus shifts towards the development of a crack detection algorithm based on the extracted damage fields (Chapter 4). The algorithm also assesses crack kinematics (Chapter 5). The validation of the crack identification method involves the use of four beams with varying material and geometrical properties, and their respective opening and sliding profiles are discussed. Additionally, this section features the determination of the center of rotation for each detected crack using rigid body kinematics. To achieve this, two reference systems (vertical and inclined) are selected, and the corresponding results are presented within these chosen systems. Ultimately, a trend regarding the presence of the center of rotation (COR) for each crack is identified and explained. This serves to support the assumptions made about the COR in the kinematic models created and available in the literature (Chapter 5).

Part III focuses on the evaluation of stresses and the discussion of the governing parameters causing failure (Chapter 6). Several constitutive laws are considered to incorporate various interacting effects, and the appropriate findings obtained by applying these laws are discussed. The equilibrium state and force contributions attributable to each individual interaction effect are also provided to shed light on the force equilibrium inside the crack during the loading history (Chapter 6). The focus then shifts to the development of a discrete shear crack propagation model (Chapter 7), followed by the findings of interacting effects utilizing various constitutive laws available in the literature.

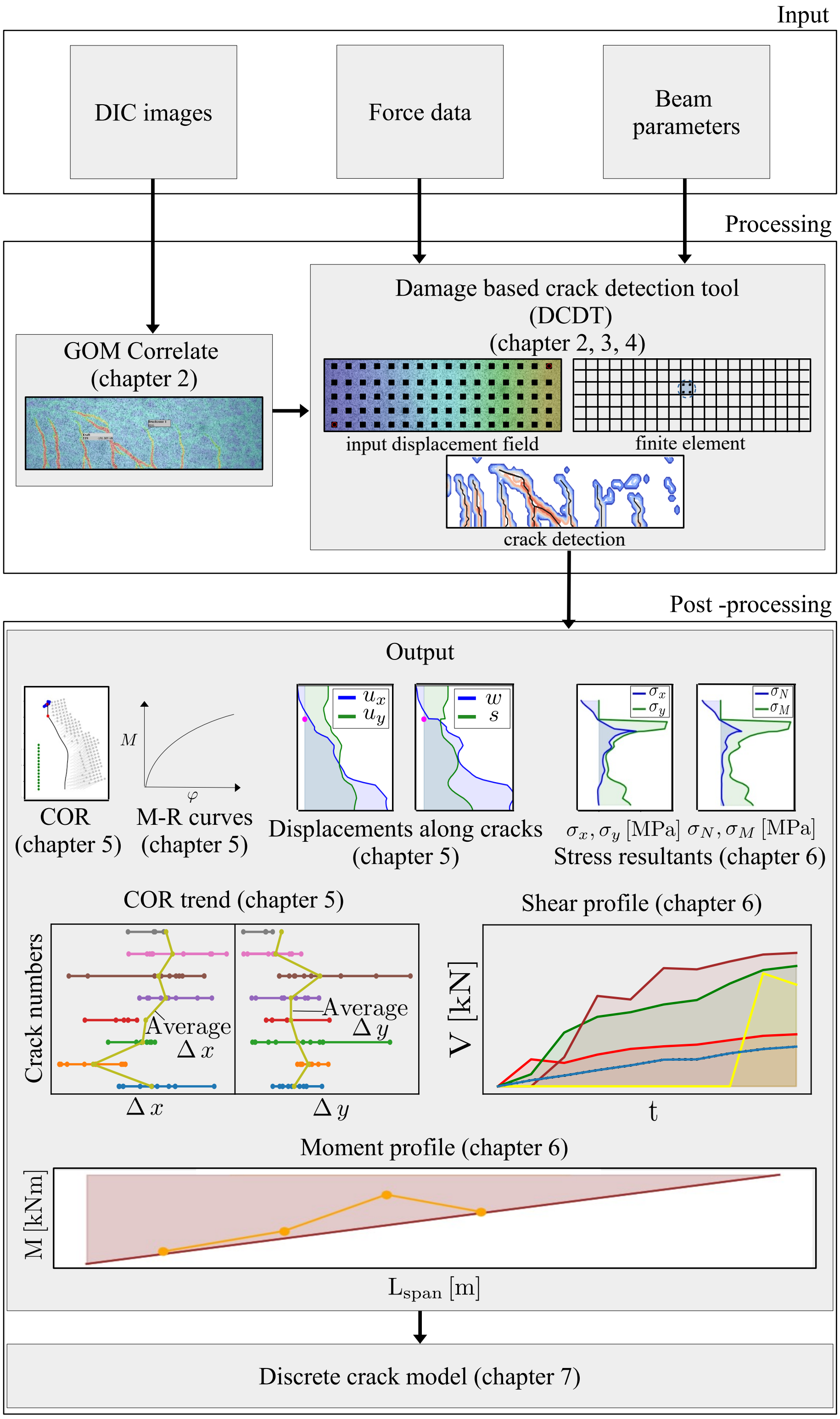

Figure 1.8: Overview of the thesis

Part I

Conversion of DIC data to time space interpolators

2 Displacement field history grid interpolator

2.1 Introduction

This chapter focuses on the transformation of data from tests to the Damage-Based Crack Detection Tool (DCDT). The DCDT's development aims to advance automated crack identification techniques based on measured kinematics, providing a more effective way to examine the mechanical background of shear failure. By analyzing extracted data, the DCDT can identify crack patterns and obtain corresponding crack opening and sliding kinematics. The development of this tool allows for greater flexibility in data refinement, enabling more accurate and detailed analysis of crack behavior. The chapter is divided into two sections:

- Import of displacement field from DIC measurements
- Output from the damage based crack detection tool (DCDT) (see Fig. 2.1)

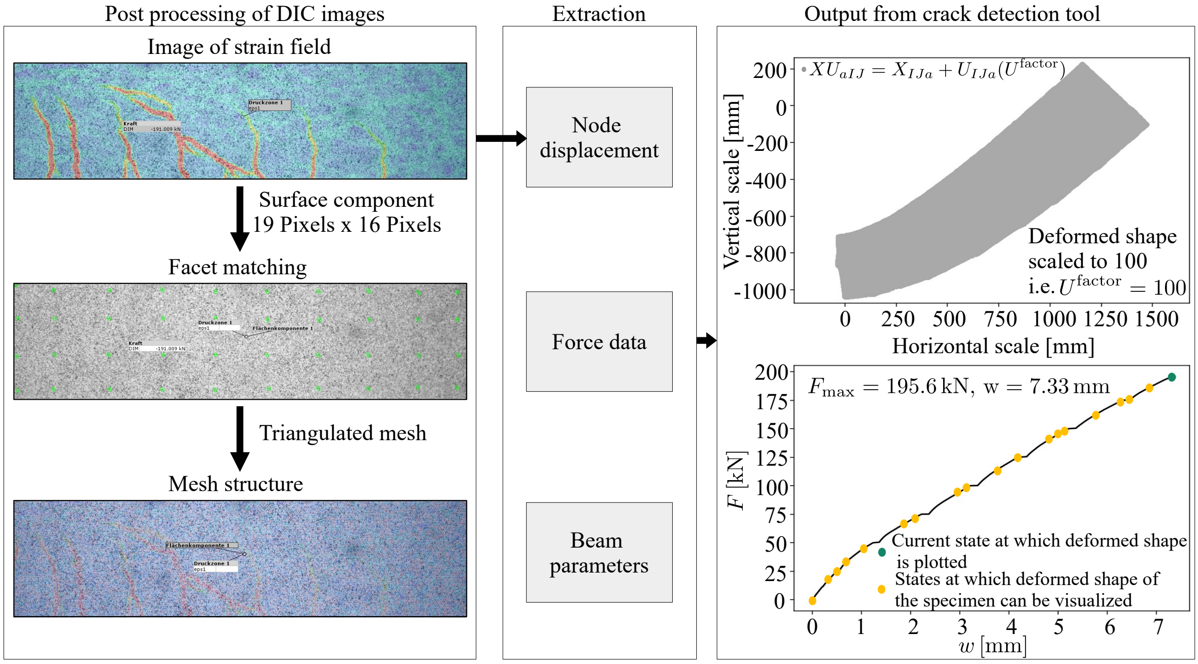

Figure 2.1: Process for data extraction from the DIC images

2.2 Import of displacement field from DIC measurements

The displacement field, a critical parameter for the Damaged-based Crack Detection Tool (DCDT), is essential for identifying cracks. This field is derived from the Digital Image Correlation (DIC) technique, which analyzes images captured using software tools such as GOM Correlate Professional 2019 [gom, 2019] (see Fig. 2.2 for an example). It should be emphasized that the described concept and implementation is independent of a particular software package or their versions.

DIC is an optical method that facilitates the extraction and analysis of surface deformations. By comparing the surface properties of materials under loaded and unloaded conditions, DIC images enable the precise determination of surface deformations. Various DIC software tools, including open-source options, are available to perform these analyses. Some notable tools include Vic-2D/Vic-3D by Correlated Solutions and ARAMIS by GOM.

DIC tools function by monitoring displacement through pattern recognition and identifying displacement trajectories during testing. An integral part of these tools is the evaluation of strains. However, in this work, achieving the goal of damage-based identification of evolving discontinuities requires more flexibility than standard strain evaluation can offer. Therefore, a general concept is described to transform the displacement field from unstructured data representing the movement of the monitored field at individual identified points into a structured time-space object. This transformation is essential for establishing a platform for further processing, aimed at identifying individual cracks and their local characteristics.

This chapter presents the motivation and added value of this approach. By transforming the displacement field into a structured format, we can better analyze and identify damage characteristics. This methodology underpins the subsequent steps in our research, providing a clear rationale for our chosen approach and demonstrating its broader applicability beyond specific software tools.

2.2.1 Facet size

The segmentation of the surface is based on the pixel fragmentation within the images, determining the division of the surface into square segments for analyzing displacement data in GOM. Each segment, or facet, is characterized by its central point. The identification of these facets across different images is achieved through facet matching. This correlation process between images depicting the deformed state and the initial state enables a systematic observation of the surface transformation. The gradual tracking of these transformations forms the core of this analysis.

It’s important to note that delving into the intricate mathematical underpinnings of GOM’s formulation exceeds the scope of this thesis. For an in-depth exploration, in-

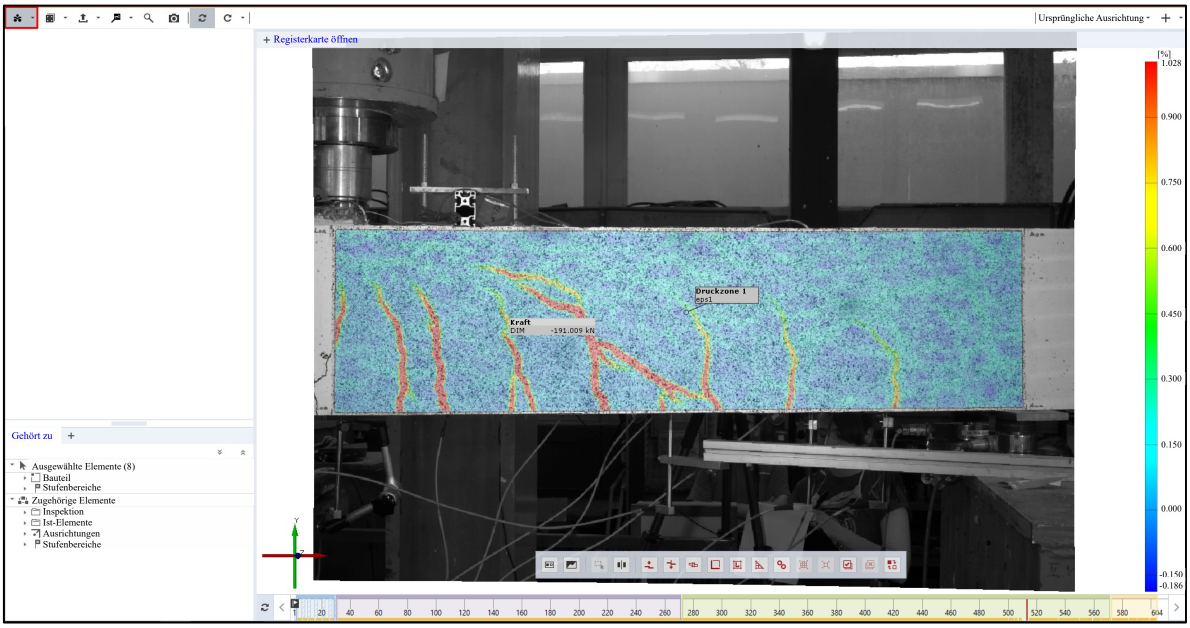

Figure 2.2: GOM user interface

terested readers can refer to [gom, 2020]. The visual representation of facet mapping is elucidated in Fig. 2.3a.

The surface component is defined by a default facet size of 19 × 16 pixels, which can be adjusted based on the measurement tasks and stochastic pattern. Changing the facet size may improve accuracy or reduce computation time. Larger facet sizes lead to faster computation times, but result in poorer acquisition of local effects within the facet. Conversely, smaller facet sizes result in better acquisition of local effects within the facet but require more computation time. For instance, Fig. 2.3a provides a visual representation of the surface of the beam after the facet size has been defined.

2.2.2 Mesh structure

Following the definition of the surface component, a structured mesh is generated to represent it. Accessible via the menu tab (mesh structure as indicated in Fig. 2.3bc), each mesh component is systematically numbered, aligned with the established global reference system, typically situated near the structural element's center.

It is important to note that data will only be saved for the current loading state/image. The x and y displacements for each node are recorded in a '.csv' file. Therefore, the analysis must be run to store the surface displacements relative to the initial state for all captured images.

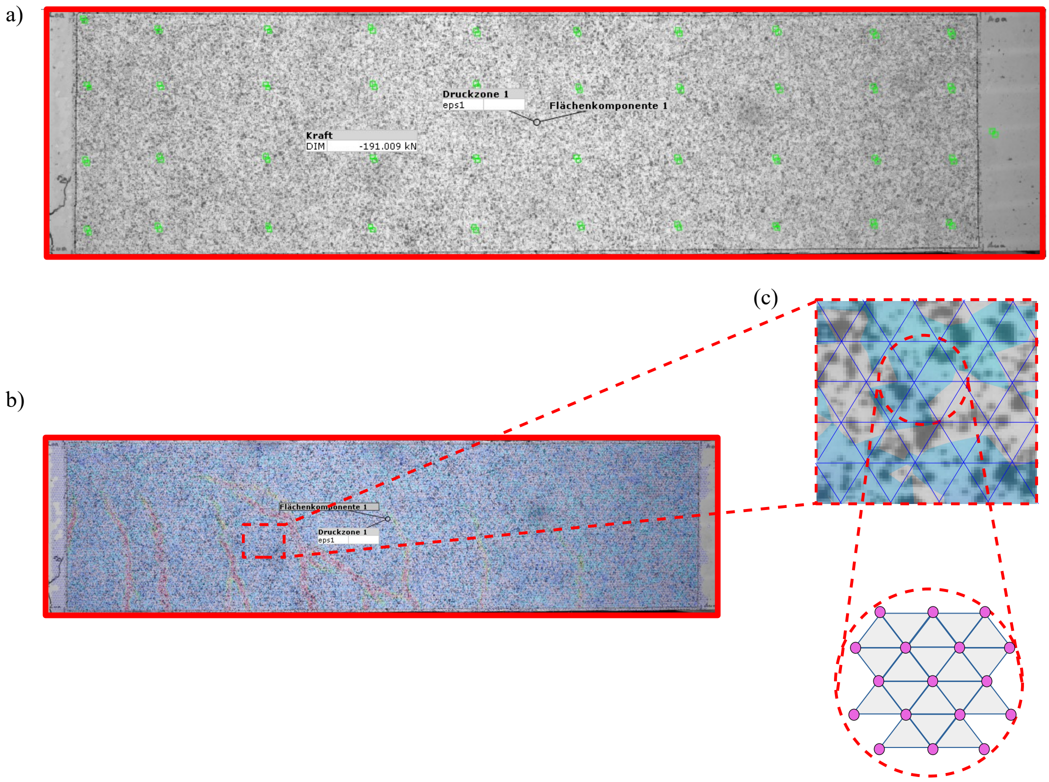

Figure 2.3: (a) Facet matching on the structural element, (b) mesh structure on the beam, (c) zooming the beam to show the triangulated mesh structure

2.2.3 Time scale

Following the computation and storage of surface displacements for every image, the calibration of the scale bar becomes pivotal to represent the temporal progression accurately, subsequently reflecting the time scale in seconds (refer to Fig. 2.4). This temporal calibration allows for a comprehensive examination of the structural element.

For a more nuanced analysis, Digital Image Correlation (DIC) images are systematically captured at predefined intervals. As the load incrementally approaches the beam's failure point, a heightened frequency of image capture is employed, enabling a finer sampling rate. This refined approach provides a detailed observation of the structural behavior, particularly as the beam nears its point of mechanical failure.

2.2.4 Example of data extraction from a DIC tool

The flowchart behind the data extraction process depicted in Fig.2.6 illustrates the aspects involved in the general transformation of data from DIC monitoring to the crack detection tool. This process ensures that the collected data is systematically archived in '.csv' files, facilitating subsequent processing steps (refer to Fig.2.5). Users have the flexibility to export all stages or the current single stage as needed. Each step's data is stored in separate files, ensuring organized and specific data records.

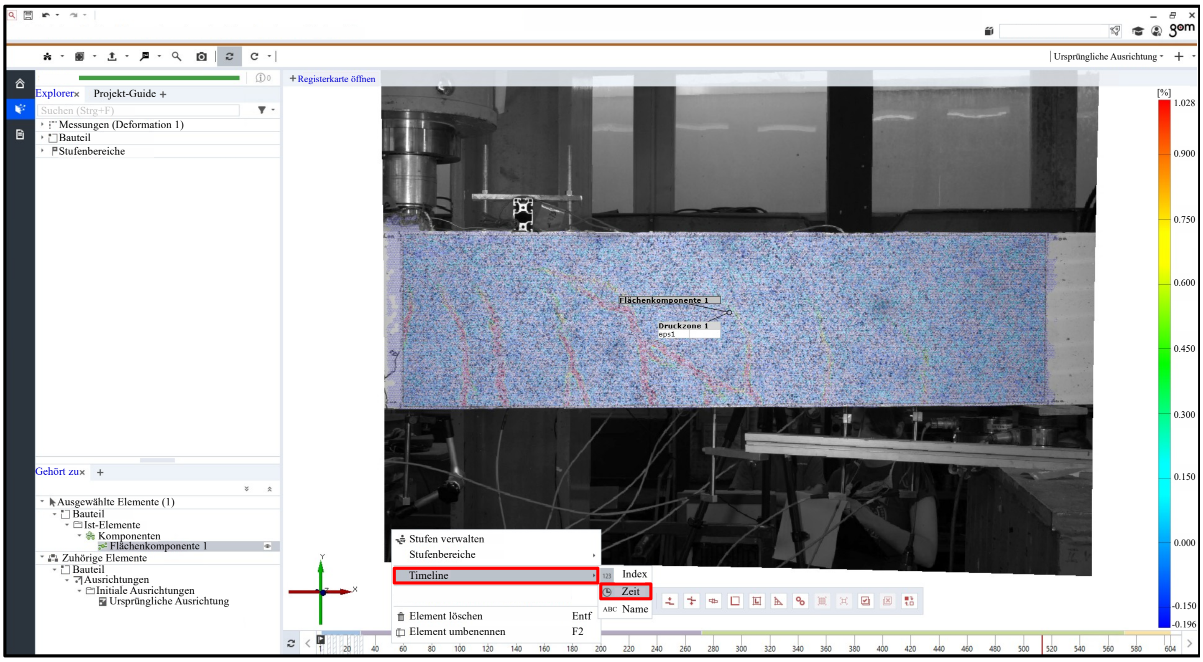

Figure 2.4: Changing the scale from DIC image count to time in seconds

To retrieve load stages using the 3D GOM system is straightforward. However, for those utilizing simpler imaging systems such as Pentax cameras, it is crucial to correlate DIC deflection measurements with actual deflection to accurately obtain load data.

Following precise file naming conventions, the load data is diligently archived in '.csv' format, ensuring accessibility and enabling further detailed analysis.

2.3 Transformation of the unstructured displacement histories into time-space grid

In this section, the input of data into the damage based crack detection tool (DCDT) is briefly explained.

2.3.1 Displacement field and loading data

The Damaged-based Crack Detection Tool (DCDT) is crucially dependent on two primary datasets: the extracted displacement field and the corresponding loading data encompassing all time steps.

Within the specified directory, displacements for each point of the triangulated mesh throughout all stages are meticulously recorded. The dataset extraction assumes a flexible format, typically comprising time-stamped files. Each file contains identified points P along with their respective displacements u_x, u_y, u_z. The associated load-time data may optionally include additional LVDT measurements.

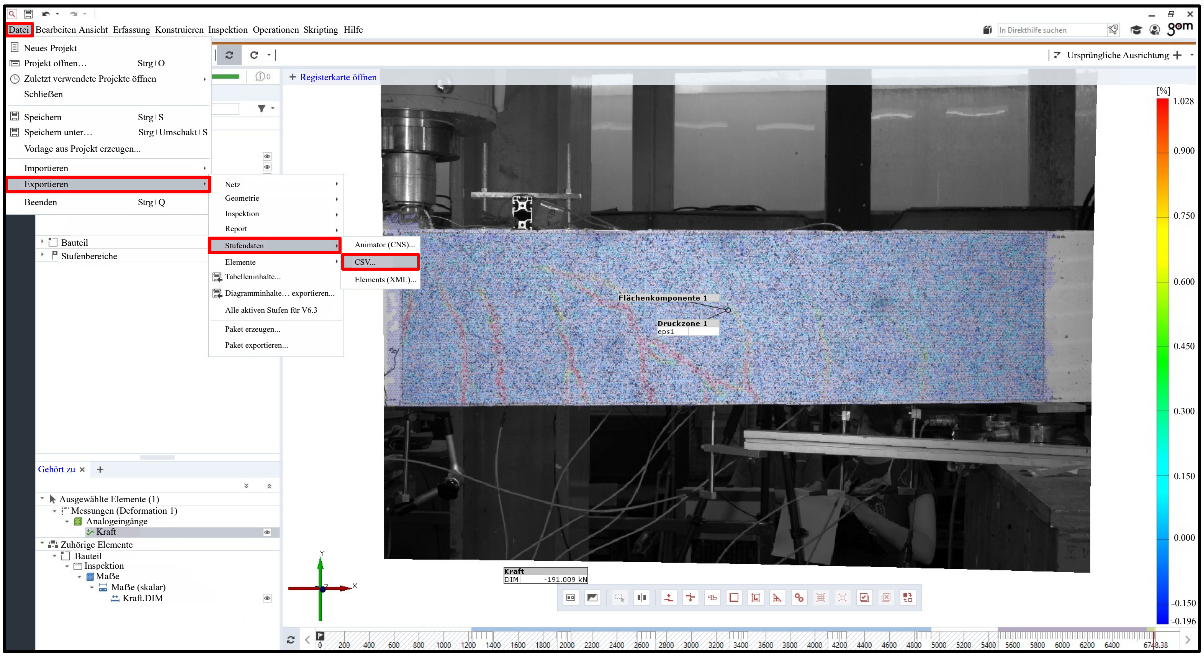

Figure 2.5: Exporting data in '.csv' format

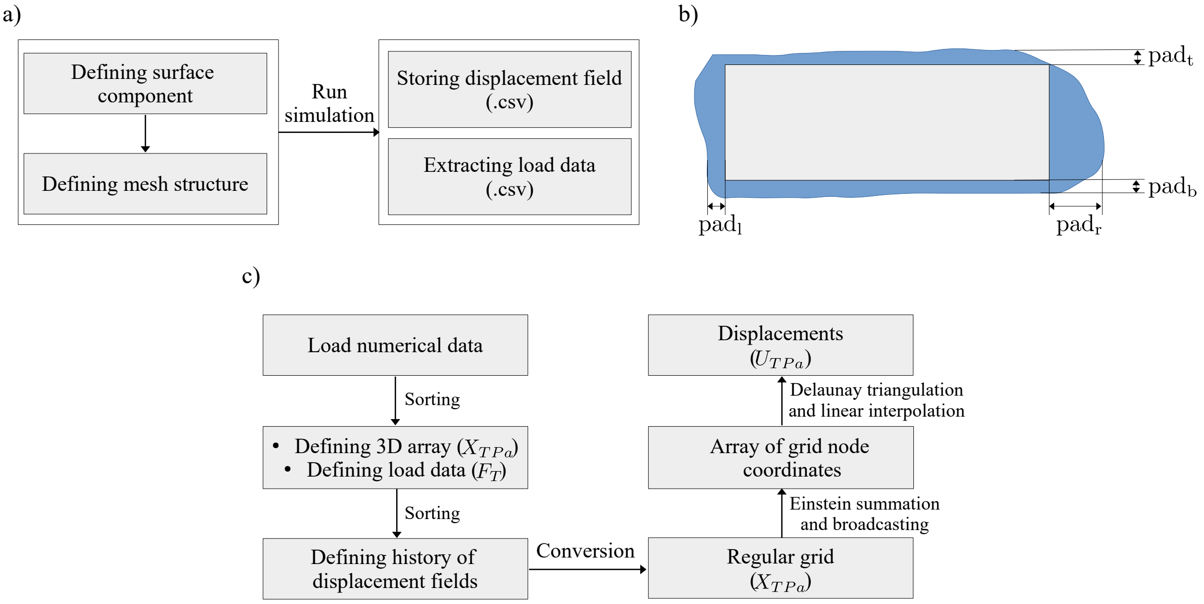

Figure 2.6: (a) Flow chart of steps to extract data from GOM, (b) pictorial representation of padding definition, (c) Conceptual work flow of post processing of data in DCDT

For clarity, technical specifics are delineated. When considering GOM-exported monitoring data, for instance, the 'Δ.DIC.csv' file encompasses load data across all stages. The 'dic_params' file specifies critical parameter values: x_{offset} and y_{offset} indicating horizontal and vertical offsets of the DIC input displacement grid from the beam's left and bottom boundaries. Additionally, pad_t, pad_b, pad_l, and pad_r denote cutoff distances for top, bottom, left, and right pads, respectively (see Fig. 2.6b and Fig.2.8b).

Once the file locations are established, the extracted data becomes accessible and serves as input for DCDT. Detailed code snippets facilitating this data extraction process are provided in the appendix for reference. Subsequent sections further elaborate on the integration of this data within the tool.

2.3.2 Example of transformation for beam test

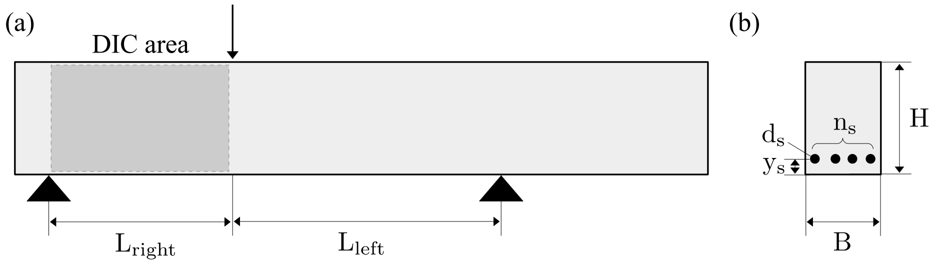

Figure 2.7: Beam and its cross sectional parameters

In the context of analyzing beam behavior using Digital Image Correlation (DIC) data, precise definition of design parameters is pivotal. These parameters encompass critical dimensions such as beam size and reinforcement ratio, along with the accurate placement of the DIC measurement zone along the beam specimen. Establishing these parameters is fundamental to correlating experimental data with theoretical principles of constitutive behavior and equilibrium conditions.

Fig. 2.7 illustrates key variables: L_{right} and L_{left} denote the distances from the DIC zone to the right and left supports, respectively. Additionally, B (beam width), H (beam height), n_s (number of steel bars), y_s (distance of bars from the bottom), and d_s (diameter of reinforcement) define structural dimensions and reinforcement specifics critical for thorough analysis.

Accurate representation of these dimensions ensures a comprehensive understanding of the beam's mechanical response under varying loads. Specifying the reinforcement ratio and precise DIC zone positioning enhances the analytical robustness and reliability of the study, facilitating deeper insights into structural behavior and performance.

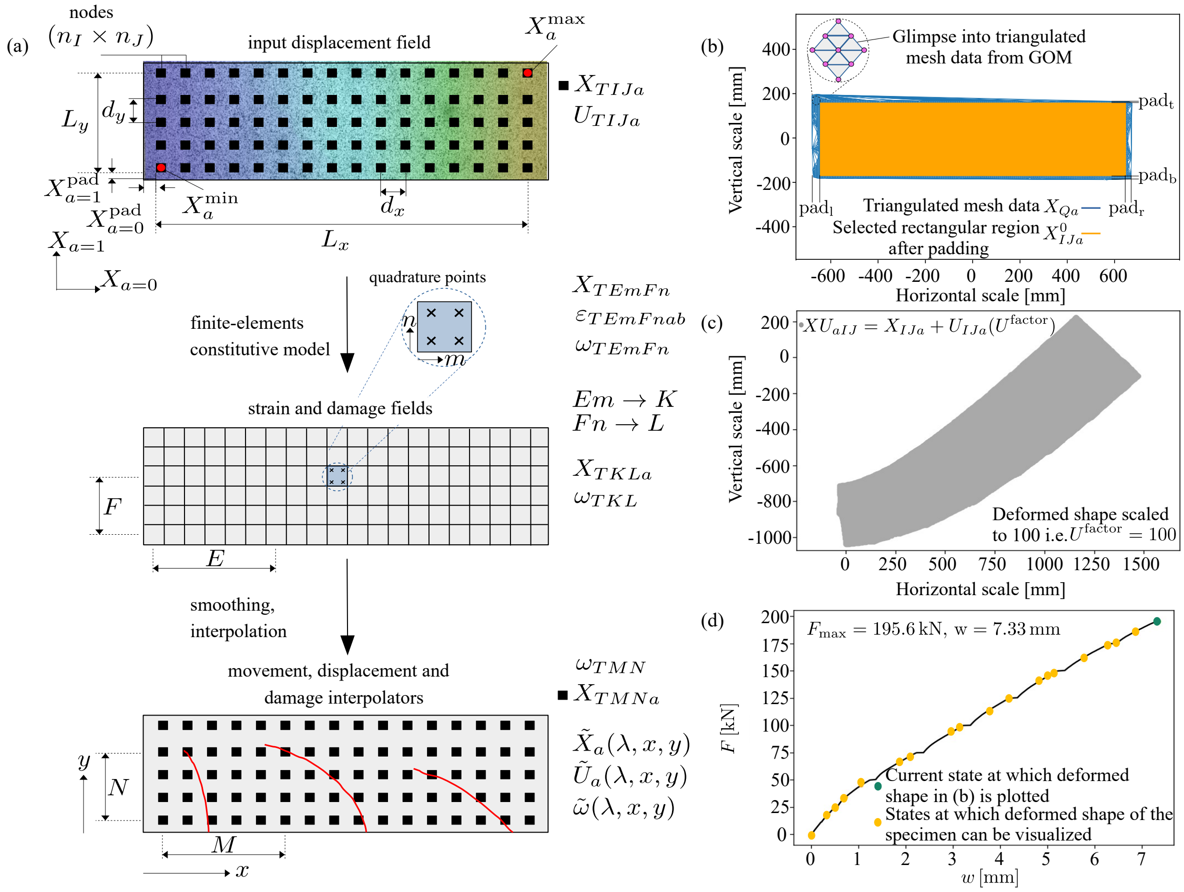

Figure 2.8: (a) Sequence of processing steps starting from the DIC grid, calculation of the strain, damage and stress grid, construction of interpolators for the crack detection algorithm and quantification of crack ligament states, (b) pictorial explanation of mesh and padding for understanding the concept of the model, (c) deformed shape of the beam enlarged to the scale of 100, (d) load deformation plot obtained from the code

2.3.3 Load displacement history

To seamlessly integrate the load-displacement history from the tests into the Damaged-based Crack Detection Tool (DCDT), the recorded values undergo a careful reading and processing phase. This process is facilitated through the utilization of prominent Python libraries, notably `pandas` [pandas development team, 2020] and `numpy` [Harris et al., 2020]. Refer to the code snippet provided in the Appendix for a detailed implementation.

These Python libraries serve as instrumental tools, offering robust functionalities to read and process the recorded test data. Leveraging the capabilities of `pandas` and `numpy`, the load-displacement history is efficiently prepared for seamless assimilation within the DCDT.

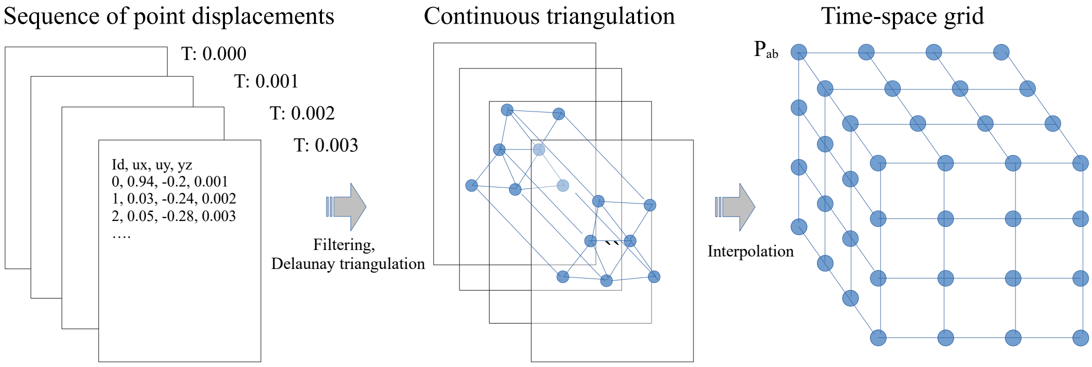

Figure 2.9: Transformation of text data into numerical arrays

2.3.4 Synchronization of data input channels

Aligning the measurements from the DIC snapshots and the machine requires synchronization of their respective time and force data. This alignment process is crucial to eliminate potential errors arising from minor time discrepancies between the camera and measurement systems. Synchronizing the load-time data from the DIC snapshots with the load-displacement history from the machine enables the alignment of these two datasets.

The procedure involves several steps:

- Reading and saving the time and force data from the DIC snapshots into the tool.
- Determining the number of camera time sampling points up to the peak load.
- Reading and processing the load and time data from the machine, determining the number of machine sampling points up to the peak load.
- Aligning the two datasets based on the peak load and the number of sampling points while correcting any identified time offset.

This precise synchronization process ensures accurate alignment of measurements from both instruments, significantly contributing to reliable data analysis and interpretation. Refer to the Appendix for a detailed code snippet elucidating this synchronization process.

2.3.5 Displacement history of the DIC grid

In the initial step, the displacement history undergoes processing using the Python package `numpy`. Subsequently, the transformed data is converted into a numerical array, which is then filtered and sorted to establish a time-space grid (Fig. 2.9). This filtering and sorting process is applied to eliminate recorded displacements that contain missing data due to incomplete displacement values at certain time steps. This ensures a consistent dataset for further analysis.

After identifying such nodes, the damage based crack detection tool (DCDT) requires a three-dimensional array of point positions X_{TPa} and corresponding load levels F_T as input. Here, $T \in (0, n_T - 1)$ represents an index within the history of n_T DIC snapshots, $P \in [0, n_P - 1]$ represents the index of a point within a DIC field, and $a \in [0, 1]$ represents the dimensional index, with 0 corresponding to x and 1 to y. The history of displacement fields of all points P is then defined based on this array, such that:

$$U_{TPa} = X_{TPa} - X_{0Pa} \tag{2.1}$$

Let us represent a simple code snippet here to explain the implementation in the python code using numpy.

```
data = np.load('dic_data')

# Extracting displacement (X_TPa) and force (F_T) data
X_TPa, F_T = data['X_TPa'], data['F_T']

# Obtaining the displacement at the first time step
X_0Pa = X_TPa[0,:,:]

# Calculating displacement relative to initial positions via broadcasting
U_TPa = X_TPa - X_0Pa[None,...]
```

This code snippet illustrates a basic implementation where data is loaded, and displacement is derived by comparing positions with their initial states utilizing broadcasting in NumPy.

To provide a maximum flexibility for processing of the point displacements U_{TPa} (see Fig. 2.8a), we need to transform them to a regular grid of $n_I \times n_J$ points denoted as X_{IJa} covering the monitored area, where $I \in [0, n_I - 1])$ and $J \in [0, n_J - 1]$. The grid points X_{IJa} must be within the monitored area covered by the positions X_{TPa} during the loading history. The bounding box of the monitored grid domain Ω is then obtained as

$$X_a^{\mathrm{min}} = \min_{Pa}(X_{0Pa}) + X_a^{\mathrm{pad}}, \; X_a^{\mathrm{max}} = \max_{Pa}(X_{0Pa}) + X_a^{\mathrm{pad}}, \tag{2.2}$$

The code snippet will thereby be written as:

```
# Padding values for the X-axis and Y-axis
X_pad_a = np.array([40, 40])

# Calculating minimum coordinates considering left and bottom values
X_min_a = np.array([np.min(X_0Pa[:,a]+X_pad_a[a]) for a in (0,1)])  # Left & Bottom

# Calculating maximum coordinates considering right and top values
X_max_a = np.array([np.max(X_0Pa[:,a]-X_pad_a[a]) for a in (0,1)])  # Right & Top
```

where, X_a^{pad} ensure that the rectangular frame is inscribed into the monitored region (see Fig. 2.8a). The dimensions of the rectangular grid and the horizontal and vertical distances between the nodes are expressed as

$$L_a = X_a^{\max} - X_a^{\min}, \;\; \Delta X_a = [L_0/n_I, L_1/n_J]\,. \tag{2.3}$$

This can be performed in numpy as:

```python
# Calculating frame dimensions based on maximum and minimum coordinates
L_a = X_max_a - X_min_a  # Frame dimensions

# Node distance and dimensions
d, n_a = 4, 2  # Node distance [mm], n_a dimensions

# Calculating grid dimensions (number of nodes along each axis)
n_I, n_J = np.array(L_a / d, dtype=np.int_)

# Calculating grid spacing along each axis
d_X_a = [L_a[0] / n_I, L_a[1] / n_J]
```

Now, the index map of the grid points can be generated using the expression

$$\mathcal{G}_{aIJ} = (1-a)I + aJ, \tag{2.4}$$

The code to obtain this reads as:

```python
# Generating index arrays for nodes along each axis
I, J, a = [np.arange(n) for n in (n_I, n_J, n_a)]

# Generating the grid of interpolation points
G_aIJ = (np.einsum('a, I->aI', (1 - a), I)[:, :, None] +
         np.einsum('a, J->aJ', a, J)[:, None, :])
```

The corresponding code written here to explain the implementation uses two powerful concepts related to the multi-dimensional array data model: (i) The product of indexed arrays defined using an Einstein notation provided by the `numpy.einsum` method, and (ii) the broadcasting of arrays that expand the dimensions of the I and J arrays to combine their values.

The array of the grid node coordinates can be obtained by multiplying the index map with the step size in directions a

$$X_{aIJ} = X_a^{\min} + \Delta X_a \mathcal{G}_{aIJ}. \tag{2.5}$$

Therefore, the code to obtain the grid coordinates reads as:

```
# Generating the grid of points in 3D space based on minimum coordinates and grid spacing
X_aIJ = (X_min_a[:, None, None] +                                                          2
         np.einsum('aIJ, a->aIJ', G_aIJ, d_X_a))
```

To project the displacements U_{TPa} onto the regular grid X_{aIJ}, the Delauney triangulation in combination with a linear interpolator class `LinearNDInterpolator` is applied. Both methods are provided by the `scipy` package [Virtanen et al., 2020]. By executing this rapid transformation for each time index T we obtain the history of displacement as a four-dimensional array U_{TIJa}. Let us remark, that this transformation is very efficient and allows for the most simple format of input data without any restriction on the structure of the DIC monitored points. The structured input data is constructed solely from the list of points and their movement during the monitoring.

Starting from this point, all the code snippets corresponding to each set of equations utilized in developing the DCDT are consolidated in the appendix.

2.4 Elementary study

This section aims to present a fundamental study demonstrating the benefits of using the displacement field history grid interpolator. A reinforced concrete beam tested at the Institute of Structural concrete has been selected for this study. The displacement history for various loading stages of this beam will be analyzed. This analysis seeks to provide valuable insights into the effectiveness and advantages of employing the displacement field history grid interpolator. The characteristics of the beam are as follows (see Fig. 2.10 (ab)):

Table 2.1: Geometrical parameters of beams

Index	**Beam 1**
Shear slenderness [λ]	4.30
Aggregate diameter [$\mathrm{d_{ag}}$]	32 mm
Reinforcement ratio [ρ]	0.0105
Diameter of steel [$\mathrm{d_s}$]	16 mm
Shear span [L]	1300 mm

Fig. 2.11 presents the load deformation curve obtained during the laboratory testing of the beam. To analyze the beam's behavior under different loading conditions, three specific loading stages were chosen from the load displacement history. Using the displacement field history grid interpolator (Fig. 2.11 (abc)), the corresponding displacements at each load step were determined.

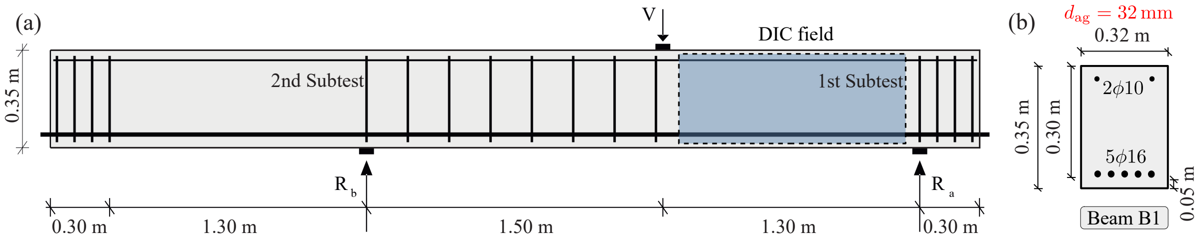

Figure 2.10: (a) Test setup, (b) cross section

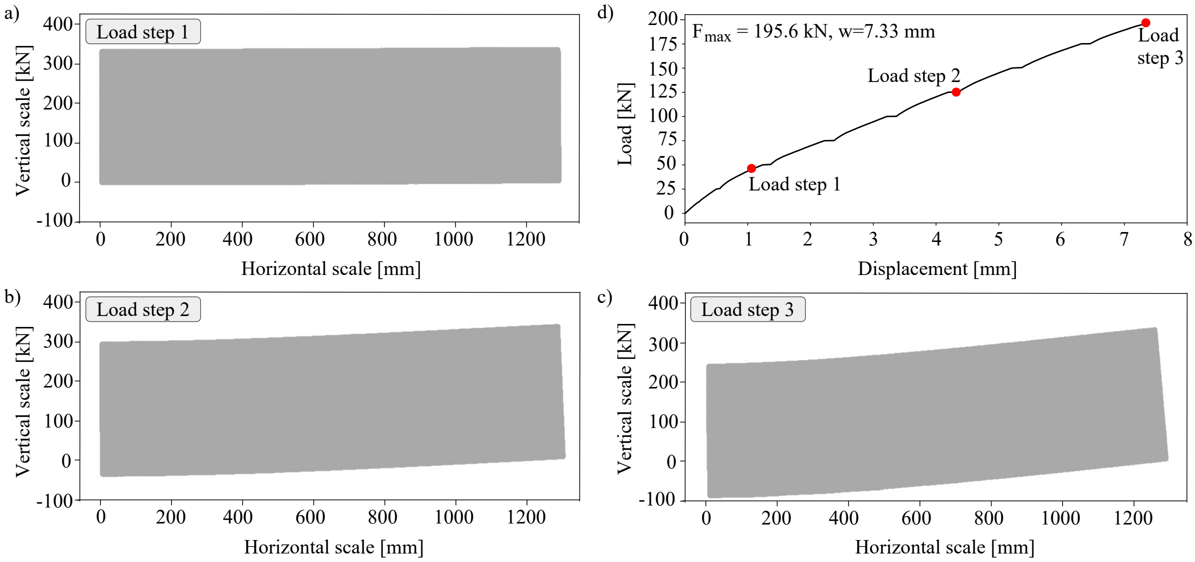

Figure 2.11: (abc) Deformation stages during various load steps, (d) Load deformation curve of the studied beam

The study demonstrates the transformation of DIC monitoring data into an efficient time-space grid interpolator. By recording displacement data at each load step and applying interpolation techniques, the study achieves a clear visualization of the concrete beam's deflection and deformation patterns. This process aids in understanding the beam's behavior under various load levels. The interpolator identifies critical points, such as potential areas of high displacement, enhancing the assessment of the beam's performance.

2.5 Conclusions

This chapter serves as a comprehensive guide to extracting and storing displacement field data from various measurement systems, as well as load-displacement history data from testing. These datasets serve as crucial input parameters for the damage-based crack detection tool (DCDT), the central focus of this thesis. Additionally, the chapter provides a conceptual overview of the Python code snippets available in the appendix, which facilitate data extraction and processing.

The developed method focuses on integrating displacement history with the constitutive behavior of the concrete matrix, emphasizing the critical role of accurate time-space approximation of displacement fields. This precision is essential for capturing detailed insights into strain, stress, and potential damage fields necessary for effective crack detection.

Ultimately, the presented elementary study showcases the benefits of incorporating the displacement field history grid interpolator into the analysis of reinforced concrete beams. The method's capacity to accurately capture structural behavior and deformation patterns under varying loading conditions renders it a valuable tool for structural engineers and researchers alike. Leveraging the power of this interpolator enables us to elevate the safety and dependability of reinforced concrete structures, thereby advancing modern structural engineering practices.

3 Strain and damage field history evaluation

3.1 Introduction

In this chapter, the main emphasis lies in the development of a DIC-controlled damage localization model tailored to detect cracks in reinforced concrete structures. The primary objective of this model is to deepen our understanding of the cracking behavior and nonlinear response of structural concrete. While the literature offers various crack detection methods, they often come with inherent limitations. To overcome these challenges associated with crack detection in quasi-brittle materials like concrete, the proposed model takes advantage of damage fields. By utilizing these fields, the model aims to provide a more effective and reliable approach to detecting cracks, ensuring a comprehensive analysis of the structural integrity of concrete elements.

The procedure applied to detect the cracks, including the history of propagation, is sketched in Fig. 3.1 [Seemab et al., 2022]. The crack detection algorithm takes the 2D displacement fields obtained from the DIC analysis as an input for a nonlinear finite element analysis. The DIC markers are equivalent to the nodes of the rectangular finite discretization using bilinear elements as indicated in Fig. 3.1a. The resulting approximation of the displacement field is used to evaluate the strain field in each material/quadrature point of the finite elements shown as the field of maximum tensile principle strain in Fig. 3.1b. The strain tensor obtained at each material point is used as an input for the evaluation of the stress and damage using the microplane damage material model. The anisotropic damage field shown in Fig. 3.1c covering the whole shear zone serves as the basis for the automated crack detection algorithm.

3.2 Multi-dimensional array

The ambition in this thesis is not only to explain the mathematical concepts behind the crack detection tool but also to illustrate the implementation method. To accomplish this, the mathematical expressions are accompanied with the code snippets in the appendix indicating how is the math translated to the executable code. This way of description should make the code of the crack detection tool readable and adaptable for interested readers of the thesis. Moreover, the implementation is available in an interactive form as an open-source on github [Chudoba et al., 2022] and can be remotely executed in a standard web browser using the interactive Jupyter notebook.

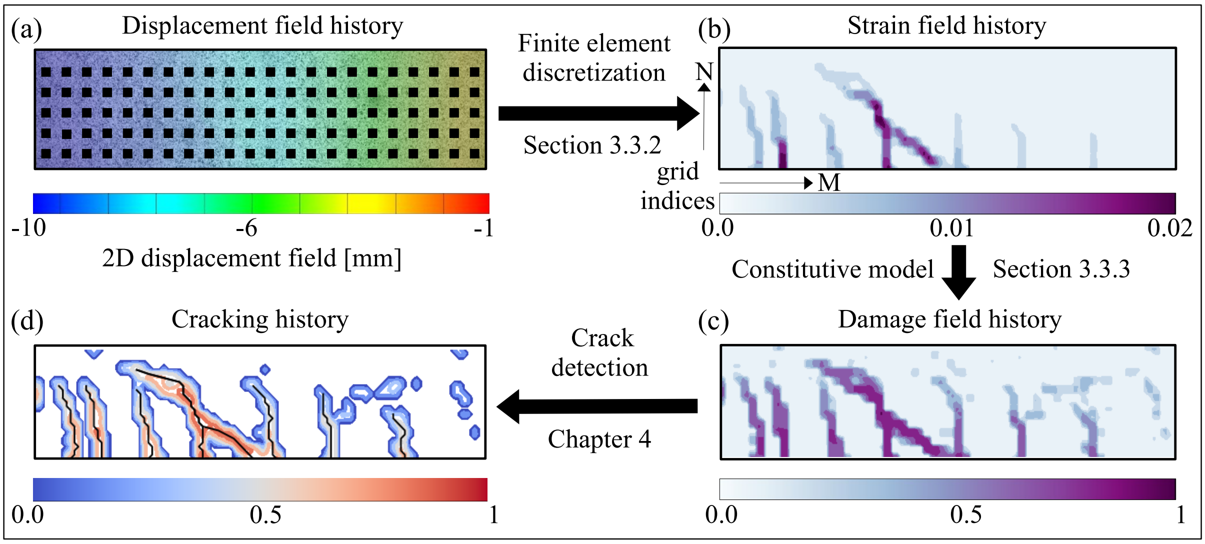

Figure 3.1: Roadmap through the chapter structure showing the processing steps (a-d) of the crack detection scheme

The crack detection procedure incorporates an integrated tiny finite-element solver, which relies on the concept of multi-dimensional arrays using index variables to denote individual dimensions. Operators are defined using the Einstein summation rule for the indexed variables. This notation facilitates the direct transfer of mathematical derivations into an executable form using modern Python packages for scientific computing, such as `numpy` and `scipy` [Virtanen et al., 2020].

The expressive power of the index-based operator definition simplifies the data model, eliminating the need to explicitly type scalars, vectors, and matrices, as they are automatically represented as generic multi-dimensional arrays. Consequently, the resulting code achieves high computational efficiency, benefiting from highly optimized array contraction and expansion operators.

After extracting displacements as explained in Chapter 2, the strain and damage field for the shear zones will be obtained as described below:

3.3 Strain field history

To calculate the strain field on the surface of the specimen, bilinear approximation over a quadrilateral element with the nodes arranged consistently with the grid $\mathcal{G}_{aIJ}$ (see Fig. 2.8a)

$$g_{aij} = \mathcal{G}_{a;I=i;J=j}, \quad i,j \in [0,1] \times [0,1] \tag{3.1}$$

and parametric coordinates

$$\eta_a = (\eta_0, \eta_1) \in [-1,1] \times [-1,1], \tag{3.2}$$

defined within the corner node positions

$$\xi_{aij} = 2g_{aij} - 1 \tag{3.3}$$

can be readily defined as

$$N_{ij} = \frac{1}{4}(1+\eta_0\xi_{0ij})(1+\eta_1\xi_{1ij}). \tag{3.4}$$

This definition renders $N_{ij} = 1$ if the parametric coordinate takes the value of the respective node position $\eta_r = \xi_{rij}$. To allow for an efficient implementation using the index summation rule, the values and the derivatives of the shape functions (3.4) in the quadrature points inside an element

$$\eta_{rmn} = \frac{1}{\sqrt{3}}\xi_{r;i=m;j=n},\ m,n \in [0,1] \times [0,1] \tag{3.5}$$

are expressed in an expanded form as

$$\begin{aligned} N_{ijmn} &= \frac{1}{4}\left[1+\eta_{rmn}\xi_{rij}+\frac{1}{2}(1-\delta_{rs})\eta_{smn}\xi_{sij}\eta_{rmn}\xi_{rij}\right], \\ N_{ijmn,s} &= \frac{1}{4}\left[\xi_{sij}+(1-\delta_{rs})\,\xi_{sij}\eta_{rmn}\xi_{rij}\right], \end{aligned} \tag{3.6}$$

with δ_{rs} representing the Kronecker delta, and r,s are the indexes of the parametric coordinates. The code calculating the local derivatives in the quadrature points of an element can be seen in the appendix.

To obtain the displacement derivatives in the global coordinates of the DIC frame, the grid data X_{IJa} and U_{TIJa} must be transformed into the format that is compatible with the subgrid of the element nodes and the attached shape functions defined by (3.3) and (3.4). This can be achieved by addressing the nodes I,J through an index map consisting of element indexes $E \in [0,n_I-2], F \in [0,n_J-2]$ and element node indexes i,j, that can be constructed by combining the mappings (2.4) and (3.1) as

$$\mathcal{H}_{aEiFj} = \mathcal{G}_{aEF} + g_{aij}. \tag{3.7}$$

The element-wise indexed arrays of node coordinates and displacements is then obtained by substituting the index map $\mathcal{H}_{aEFi}$ for the indexes I, J in X_{aIJ} and U_{aTIJ} to obtain

$$\begin{aligned} X_{aEiFj} &= X_{I=\mathcal{H}_{0EFi};I=\mathcal{H}_{1EFi};a} \\ U_{TEFia} &= U_{T;I=\mathcal{H}_{0EFi};I=\mathcal{H}_{1EFi};a} \end{aligned} \tag{3.8}$$

The corresponding code applies slice indexes and broadcasting into mutually orthogonal array dimensions (see Appendix).

With the consistently arranged element-wise representation of the grid (3.8) and the local shape function derivatives (3.6), the Jacobi matrix J_{Ear} in each element E, F and material point m, n is obtained as

$$J_{EmFnas} = N_{ijmn,s} X_{EiFja}. \tag{3.9}$$

Then, the kinematic operator, mapping the displacements to the strain field at all quadrature points as

$$B_{EiFjmnabc} = \frac{1}{2}(\delta_{ac}\delta_{bd} + \delta_{ad}\delta_{bc}) N_{ijmn,s} J^{-1}_{EmFnsd}. \tag{3.10}$$

The time-space grid of strains is then expressed as

$$\varepsilon_{TEmFnab} = B_{EiFjmnabc} U_{TEiFja}, \tag{3.11}$$

3.4 Damage field

With the strain tensor field (3.11) at hand, a damage material model can be used to detect the zones of localization. Compared to purely strain-based crack detection approaches, a normalized variable ω in each material point appears more suitable for the crack detection scheme. The amplified resolution of the localization zones can be ascertained by comparing the field of principal strain and damage shown in Fig. 3.1bd.

In the implementation of the crack detection scheme described later, the microplane damage model [Jirásek, 1999] is used to obtain an anisotropic damage tensor field within the DIC frame. For a concise explanation of the damage field evaluation, a simple scalar damage model with an equivalent strain κ has been used here. The damage is controlled by the maximum value of the principal strain components ε_a as $\kappa = \max(\varepsilon_a)$ and an exponential damage law

$$\omega(\kappa) = \frac{\varepsilon_{\mathrm{o}}}{\kappa} \exp\left(-\frac{\kappa - \varepsilon_{\mathrm{o}}}{\varepsilon_{\mathrm{f}} - \varepsilon_{\mathrm{o}}}\right), \tag{3.12}$$

where ε_{o} and ε_{f} represent the onset of inelasticity and initial rate of damage response, respectively.

The damage function is part of the constitutive law allowing for the evaluation of the stress field over the monitored zone. Let us note, that the stress field does not implicitly satisfy the global equilibrium conditions. This would be the case only when the constitutive law captures the material behavior. This statements indicates the further potential of the described DIC driven simulation for the calibration or validation of a constitutive model using the monitored localization process on the surface.

The damage field obtained on the element grid with the global positions of the quadrature points given as

$$X_{aEmFn} = N_{ijmn} X_{EiFja}, \tag{3.13}$$

needs to be transformed to a simple grid X_{aKL} for further processing using the index substitution

$$\begin{aligned} X_{a;K=2E+m;L=2F+n} &= X_{aEmFn} \\ \omega_{T;K=2E+m;L=2F+n} &= \omega_{TEmFn}. \end{aligned} \tag{3.14}$$

The equivalent code performing this transformation uses the array reshaping, i.e. flattening of the neighboring dimensions $(E,m) \rightarrow K$ and $(F,n) \rightarrow L$ (see Appendix).

In this form, the grid is prepared for further processing to provide the optimum resolution and smoothness of the damage field suitable for the crack detection algorithm. To preserve a maximum flexibility, the available time-space grid is transformed to a mapping from the continuous time-space domain to the interpolated damage variable

$$\tilde{\omega} : (\lambda, x, y) \rightarrow \omega,\ \lambda, \omega \in [0,1],\ (x,y) \in \Omega, \tag{3.15}$$

where λ denotes the load factor defined as normalized load

Table 3.1: Geometrical parameters of beams

Index	**Beam 1**	**Beam 2**	**Beam 3**	**Beam 4**
Shear slenderness [λ]	4.30	4.30	4.30	2.00
Aggregate diameter [d_{ag}]	16 mm	32 mm	16 mm	16 mm
Reinforcement ratio [ρ]	0.0105	0.0105	0.01025	0.0105
Diameter of steel [d_s]	16 mm	16 mm	25 mm	16 mm
Shear span [L]	1300 mm	1300 mm	1300 mm	600 mm

$$\lambda = \frac{F}{F_{\max}}. \tag{3.16}$$

To construct the mapping (3.15), each DIC snapshot T must be associated with a load level F_T. For the purpose of crack detection, only ascending loads up to $F_{\max}$. The post-peak response is not considered suitable for crack detection, as the majority of the cracks starts to unload and close. With these assumptions, the mapping between the time-space domain and the damage variable (3.15) can be coded as described in appendix.

Similarly to the mapping $\tilde{\omega}$, other mappings for the field variables, i.e. displacement, strain, and stress, can be constructed. These mappings are exploited in the formulation of the crack detection algorithm, validation of kinematic hypotheses or crack propagation models as shown in the upcoming chapters.

The interpolation of the coordinate and displacement fields $\tilde{X}_a(\lambda, x, y)$ and $\tilde{U}_a(\lambda, x, y)$, respectively, over the time-space domain is used in the upcoming chapters to analyze the kinematics between two teeth of a shear zone.

3.5 Experimental data for elementary studies

The developed crack detection scheme has been validated using a systematic experimental program investigating the shear behaviour in RC concrete beams without shear reinforcement. Detailed information on the test-setup and the monitoring system can be found in [Schmidt et al., 2021]. The specimens had variable lengths, and the rectangular cross-section with the dimensions $b = 320$ mm, and $h = 350$ mm. The diameter of steel reinforcement and the maximum aggregate size were also varying (see Tab. 3.1). At the time of testing the compression strength of concrete read $f_c = 38$ MPa. Each beam was designed such that two shear sub-tests could be conducted. Each sub-test was performed as three-point bending test with a cantilever (Fig. 3.2).

The vertical displacements w were measured using three linear variable displacement transducers (LVDTs) placed at the position of the load and in the middle positions between the load and each support. Apart from the LVDT measurements on the front side,

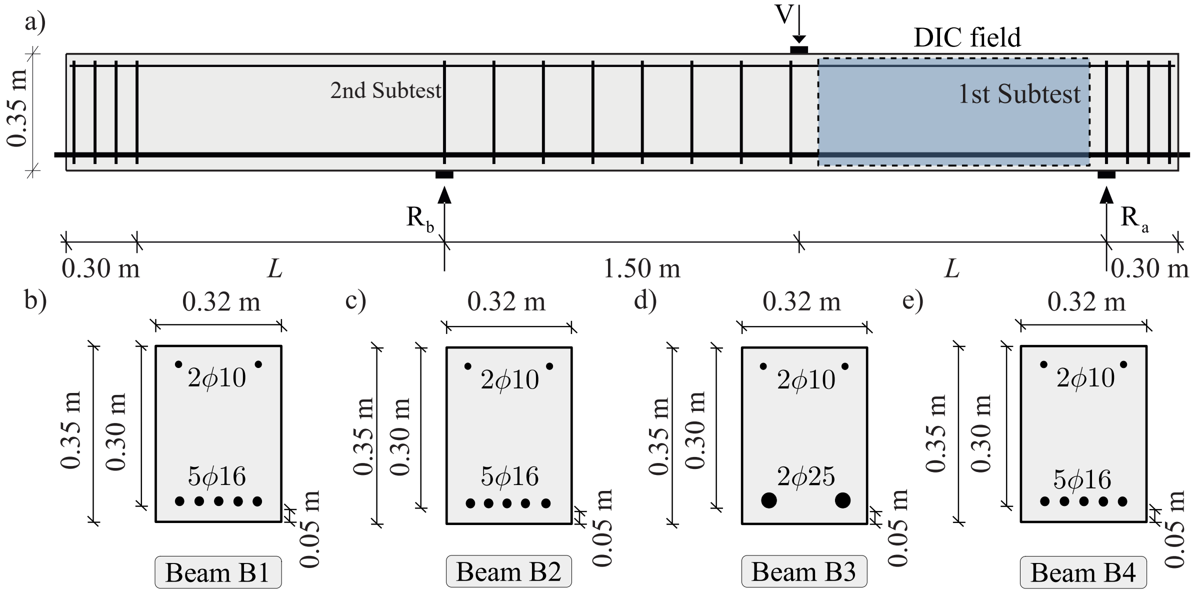

Figure 3.2: (a) Experimental test setup, (b)(c)(d)(e) cross sectional parameters of beam B1, B2, B3 and B4

a 3D-digital image correlation (DIC) measurement system was used to monitor the shear crack formation at the backside of the beam. The monitoring rate was of between 0.5 to 1 Hz. The period of one minute prior to failure was tracked with the rate of 5 Hz to capture failure process in detail by using a ring buffer system. In addition to the external measurements, strain gauges and fiber optical sensors (FOS) at the flexural reinforcement bars were used for internal measurement.

3.6 Elementary study

This section presents an elementary study aimed at demonstrating the advantages of utilizing a damage-based crack localization model. The primary focus is to highlight the suitability of incorporating a damage-based material model into the crack detection scheme, as opposed to relying solely on the strain field. This approach proves to be more appropriate for detecting cracks in concrete, a quasi-brittle material where crack formation involves localized damage.

3.6.1 History of strain and damage fields

The DIC (Digital Image Correlation) driven constitutive modeling, as outlined in Section 3.2, has been meticulously developed with a specific objective in mind: to enhance the derived strain distribution by incorporating crucial information about the constitutive behavior of the concrete matrix during localization. The application of material models takes into account the triaxial stress state inside the volume of the specimen, ensuring

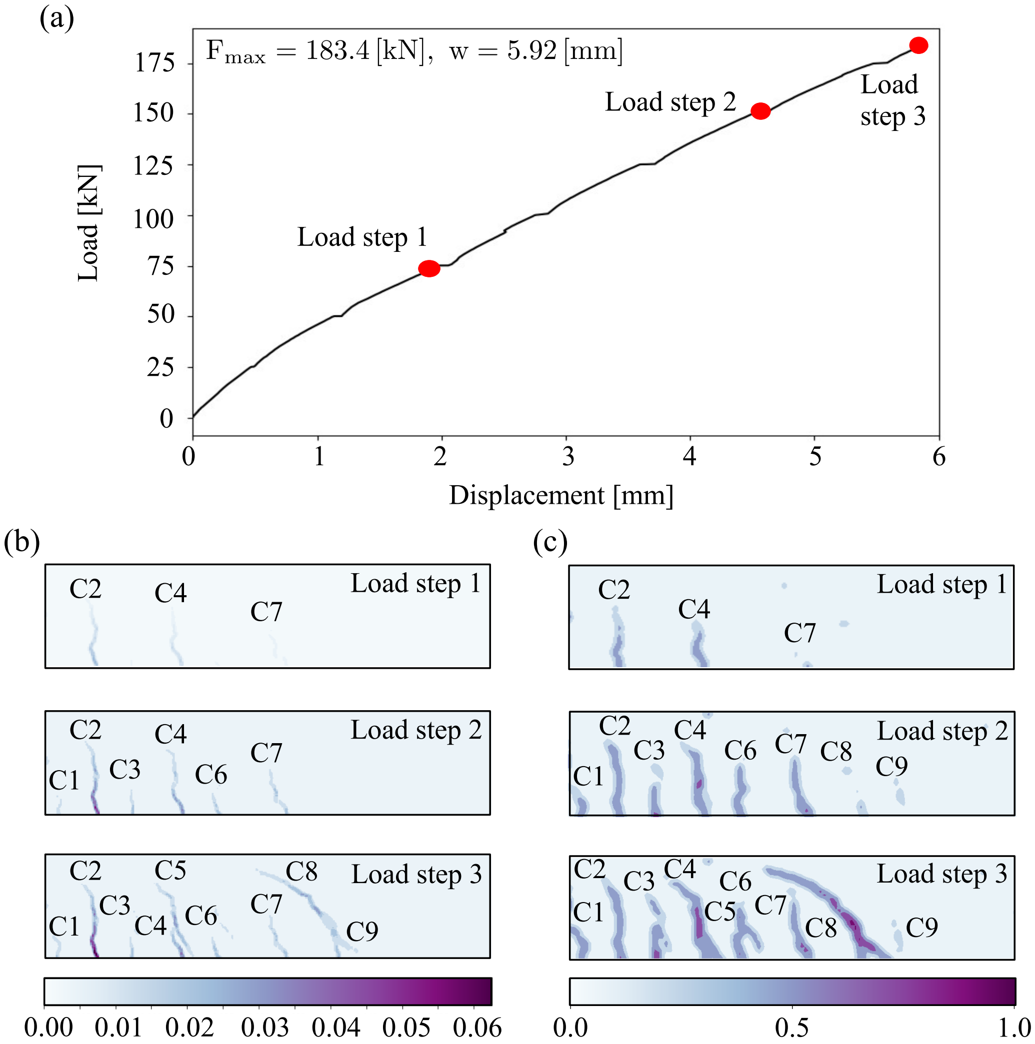

Figure 3.3: Amplification of the localization zones obtained using the damage model (a) load deflection curve (beam B1), (b) strain field distribution, (c) damage field distribution

a comprehensive and accurate representation of the material's response under various loading conditions.

To showcase the effectiveness and added value of the constitutive model, we present Fig. 3.3, which displays the strain and damage fields obtained for beam B1 using the microplane damage model at three distinct load levels. Upon closer examination, it becomes evident that the damage field provides a more comprehensive and detailed representation of the cracks compared to the strain field.

Notably, cracks are more distinctly recognizable in the damage field, particularly during the initial stage of crack localization at the bottom of the shear zone for cracks C6 in load steps 2 and 3, as well as cracks C3 and C8 in load step 2. These cracks, which might have been challenging to detect solely from the strain field, are clearly highlighted in the damage field, thereby providing valuable insights into the crack initiation and propagation process.

Moreover, the damage field proves especially advantageous in identifying branched cracks, as demonstrated in load step 3 for crack C6. While the strain field may only show this crack as a small standalone feature, the damage field enables us to recognize it as a secondary branch of another primary crack. This capability to detect branched cracks is of utmost importance, as it contributes significantly to our understanding of crack patterns and their potential impact on the overall structural integrity.

In conclusion, the incorporation of the constitutive model into the DIC-driven analysis enriches the strain distribution with critical information about the concrete matrix's behavior during localization. The damage field not only allows for better detection of cracks but also facilitates the identification of branched cracks, leading to a more comprehensive and accurate assessment of the material's response to loading. By providing deeper insights into crack development and behavior, this advanced modeling approach holds great promise for enhancing our understanding of structural mechanics and material performance under varying conditions.

3.7 Conclusions

The proposed damage-based crack localization approach offers a valuable contribution to our understanding of crack behavior and propagation in concrete. By shifting the focus from strain distribution to local damage for visualizing cracks, this method provides a more effective means of detecting not only primary cracks but also branched and closely spaced cracks that were challenging to identify using traditional strain-based techniques.

Concrete, as a quasibrittle material, undergoes a complex crack development process. Utilizing local damage to track cracking patterns and assess kinematics provides a logical and insightful strategy, shedding light on shear failure mechanics and concrete behavior under varying loads, thus deepening our understanding of crack evolution and interaction.

A significant advantage of the damage-based crack localization approach lies in its ability to identify finer crack details and complexities, including branched and closely spaced cracks, which are often overlooked in strain-based analyses. This capability is critical for evaluating the structural integrity of concrete elements and exploring new approaches to enhance safety and reliability.

Furthermore, this approach has the potential to innovate crack detection and characterization techniques in concrete mechanics. It offers a nuanced understanding of crack behavior, guiding the development of improved predictive tools and precise numerical simulations to enhance the design and assessment of concrete structures.

Part II

Discrete shear crack

4 Crack detection algorithm

4.1 Introduction

This chapter focuses on the development of a robust and advanced crack detection scheme that leverages the concept of localized damage-based material modeling. The primary aim is to enhance the accuracy and effectiveness of crack detection in complex materials, particularly in concrete. By incorporating localized damage information, this novel approach seeks to provide a more comprehensive and reliable method of crack identification compared to traditional techniques that rely solely on strain distribution.

The primary focus of this chapter is to accurately trace the history of crack paths, which is fundamental to the proposed crack detection scheme and crucial for advancing our understanding of crack propagation and behavior. By systematically recording and analyzing localized damage evolution throughout loading, the model facilitates precise visualization and tracking of crack paths as they propagate through the material.

To enhance the accuracy and robustness of crack tracing methods, constitutive models integrate surface DIC data with modeled stress redistribution within the specimen volume. In this chapter, damage models are implemented to improve data resolution in crack localization zones.

Based on the detected crack propagation geometry, automatic evaluation of opening and sliding profiles along crack ligaments, as well as center-of-rotation from experimental surface displacement measurements, becomes feasible (refer to Chapter 5). Such validation across various design configurations supports the further development and practical application of mechanical and engineering design models in engineering practice.

4.2 Crack path tracing concept

Two significant concepts constitute the basis for the proposed crack detection algorithm:

- Cracks are detected at the ultimate state in which all cracks exhibit a maximum opening. The cracking history is then detected in a reverse direction by going back in the loading history.
- The detection algorithm exploits the knowledge that the cracks in a shear zone start at the bottom layer and propagate in the direction of increasing bending moment.

The crack detection at the ultimate state is performed by tracing the ridges of the maximum principal damage values indicated by the isolines in Fig. 3.1d at the load level near the ultimate failure with all cracks fully developed and exhibiting the maximum crack opening during their propagation history. Backward tracing of the cracking history is then applied by considering the damage field history in reverse order, i.e. by stepping through the load levels down to zero and identifying the crack tips along the detected paths.

The knowledge of the crack path histories enables an evaluation of shear zone characteristics corresponding to the cross-sectional stress resultants, i.e. bending moment and shear force. Three possible evaluations are demonstrated in Chapter 5 that includes the history of opening and sliding profiles along each crack, the position of the center of rotation for all cracks, and the evaluation of moment rotation curves for each crack.

4.3 Crack detection algorithm

The crack detection is performed on a grid with the positions X_{aMN} defined with an appropriate resolution in analogy to (2.5) illustrated in Fig. 4.1. The values of damage on this grid are obtained using the mapping (3.15) for the ultimate load level $\lambda = 1$ as

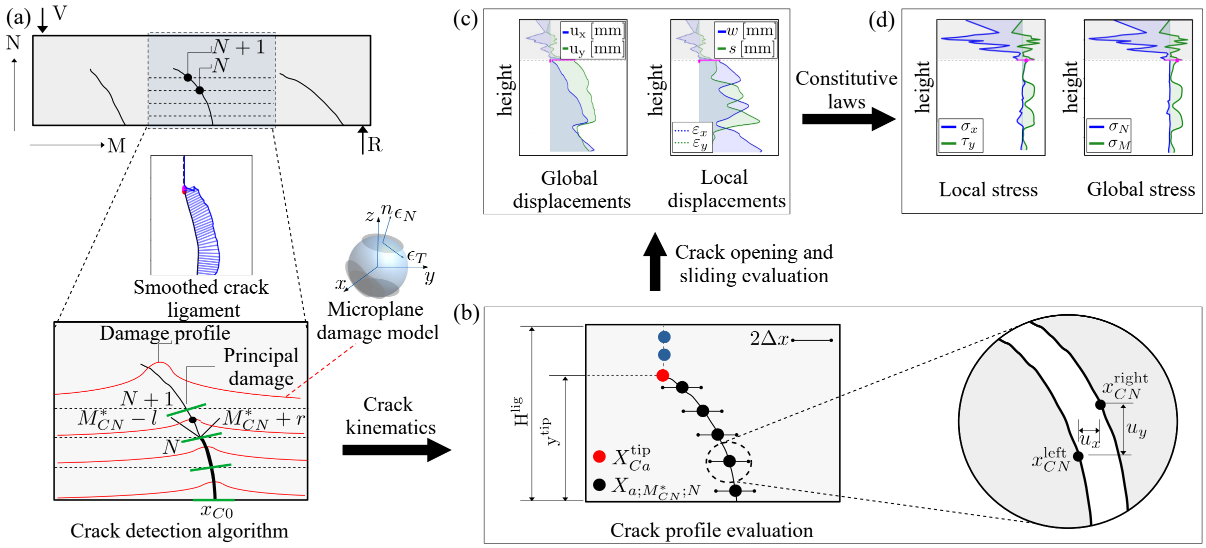

Figure 4.1: (a) Crack detection algorithm, (b) crack profile evaluation (c) global and local opening profiles for first crack in beam B1

$$\omega_{1MN} = \tilde{\omega}(\lambda = 1, X_{aMN}) \tag{4.1}$$

The algorithm initiates the crack detection process by identifying the peak values of damage along the bottom edge of the DIC frame, denoted as $\omega_{1M;N=0}$. These peak values are used to find the starting positions of cracks, represented by the indexes $M_{C0} \subset [0, n_M - 1]$ for each crack indexed by $C \in [0, n_C - 1]$. These indexes represent the global positions of the cracks at the bottom row, given by $X_{a;M=M_{C0};N=0}$.

The crack tracing proceeds row by row from the bottom to the top, systematically identifying the next damage peaks. The algorithm exploits the fact that the crack propagates in the direction of increasing bending moment. Thus, the index of the crack position in the next row is determined as:

$$M^{\star}_{C;N+1} = \mathrm{argmax}_{D=M^{\star}_{CN}-l}^{M^{\star}_{CN}+r} \left(\omega_{D,N+1} \right) \tag{4.2}$$

where $M^{\star}_{CN} - l$ and $M^{\star}_{CN} + r$ represent the minimum and maximum horizontal indexes of the corridor of the crack C, in which the peak value is searched. The parameters l and r are preset a-priori when using a scalar damage field as a localization indicator. However, when employing the anisotropic damage model implemented in the CDT package, their values are adapted row by row based on the principal directions of the damage tensor at the crack tip in the row below, i.e., $\omega_{1;M=M^{\star}_{CN};Nab}$.

Once the damage value drops below a predefined threshold $\bar{\omega}$, the crack tip value is recorded, and the horizontal index C for the above rows N is kept constant. This process constructs a vertical compression ligament corresponding to the shear crack path up to the top of the cross-section. By implementing a row-by-row processing of cracks, the algorithm requires n_N steps to detect all cracks in parallel.

The results of the detection are exemplified in Fig. 3.1d, showing the isolines of the damage field ω_{MN} and the discrete cracks represented as black solid lines. The obtained discrete piecewise linear representation of the crack path is then transformed into a continuous shape using Bezier spline approximation.

To enable a flexible implementation of operators characterizing the cracking process, the crack path at the ultimate state with the crack tip at $X^{\mathrm{tip}}_{Ca}(\lambda = 1)$ is transformed into a spline approximation. With the geometry of all cracks available, a reverse process begins to obtain the history of crack propagation for the values of $\lambda < 1$. The DIC snapshots at decreasing load steps T are iterated in a decreasing order with the load parameter λ_T. In each step, the intermediate position of a crack tip $X^{\mathrm{tip}}_{Ca}(\lambda)$ is identified by comparing the damage value with the predefined threshold $\bar{\omega}$.

As depicted in Fig. 4.1b, the changing geometry of the ligament consists of two branches: (1) the crack path along the spline running from the bottom up to the crack tip $X^{\mathrm{tip}}_{a}(\lambda)$, and (2) the vertical line from the crack tip to the top of the cross-section.

In the implementation, this crack geometry is dynamically adapted for the changing parameter λ. This process allows for the characterization of crack propagation at different load levels, providing valuable insights into the evolution of crack patterns and behavior during the loading process.

4.4 Elementary study

In this section, an elementary study is presented for beams B1 and B2, demonstrating the main features of the developed crack detection algorithm. The study highlights the automatic tracking of crack propagation, achieved through the DIC-driven constitutive modeling with localized damage-based material.

4.4.1 Automatic tracing of the cracking history

4.4.1.1 Beam B1

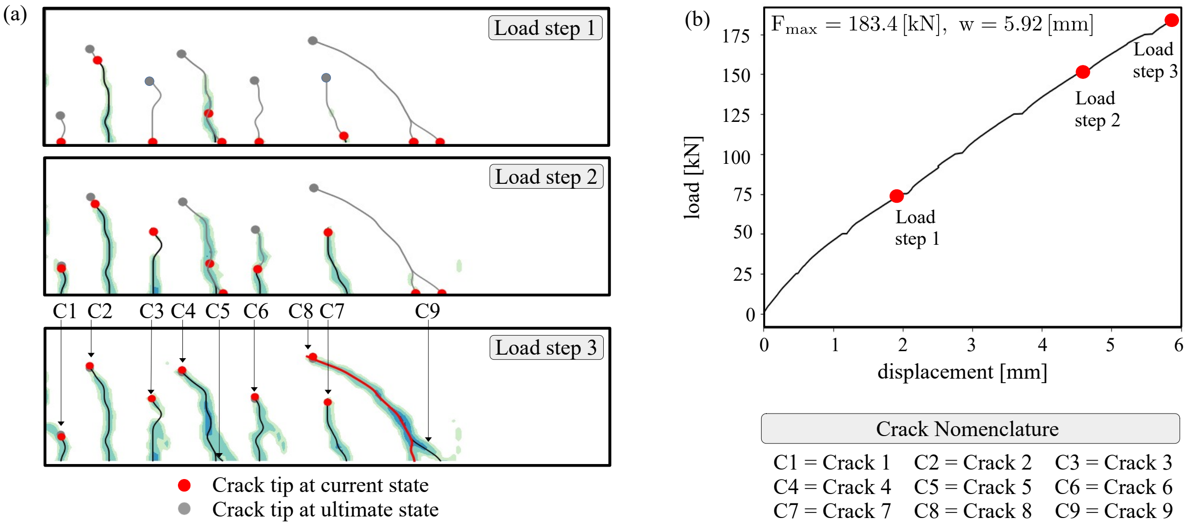

Figure 4.2: (a) Crack history tracing, (b) load deflection curve

Figure 4.2 presents a study on the crack detection algorithm described in Section 4.3, utilizing data from beam B1. The algorithm's ability to extract the complete history of all propagating cracks from the DIC data is demonstrated.

To visualize the propagating crack paths, three specific loading steps are selected, as depicted in the load-deflection curve shown in Figure 4.2b. The crack paths at the ultimate load ($\lambda = 1$) are represented by black solid lines, while the black lines with red markers at the tip indicate the states of the cracks corresponding to the specified load levels.

The critical crack, which ultimately leads to the failure of the beam, is depicted in red color. It initiates at a relatively high load level of $F > 150$ kN. Upon closer examination of the history of crack propagation in Figure 4.2, it is observed that cracks C2 and C4 have already propagated at load step 1, while cracks C6 and C7 have just initiated.

At $F = 150$ kN (load step 2), all cracks from C1 to C7 have developed and matured, while cracks C8 and C9 have not yet initiated. Shortly after load step 2, cracks C8 and C9 begin to propagate rapidly deep into the beam at load step 3, leading to the ultimate failure of the beam.

4.4.1.2 Beam B2

The crack identification study is also extended to Beam B2, and the results demonstrate the accuracy of the crack identification scheme in capturing all the cracks present in the specimen (Figure 4.3). Notably, Crack C2 is observed to initiate and propagate rapidly during the first load stage. However, it is found that the propagation of Crack C2 does not continue further for load steps 2 and 3. In contrast, Crack C3 also shows rapid initiation and propagation during the initial load stage, but its propagation persists and continues for load steps 2 and 3.

Additionally, the study reveals that Cracks C4 and C8 appear to be branched cracks. These cracks are identified as initiating and propagating after load step 2. Similarly, Crack C9 is also observed to initiate and propagate after load step 2.

The study's findings highlight the dynamic behavior of cracks in Beam B2, with some cracks initiating and propagating quickly at the initial load stage, while others continue to evolve and propagate over subsequent load steps. The identification of branched

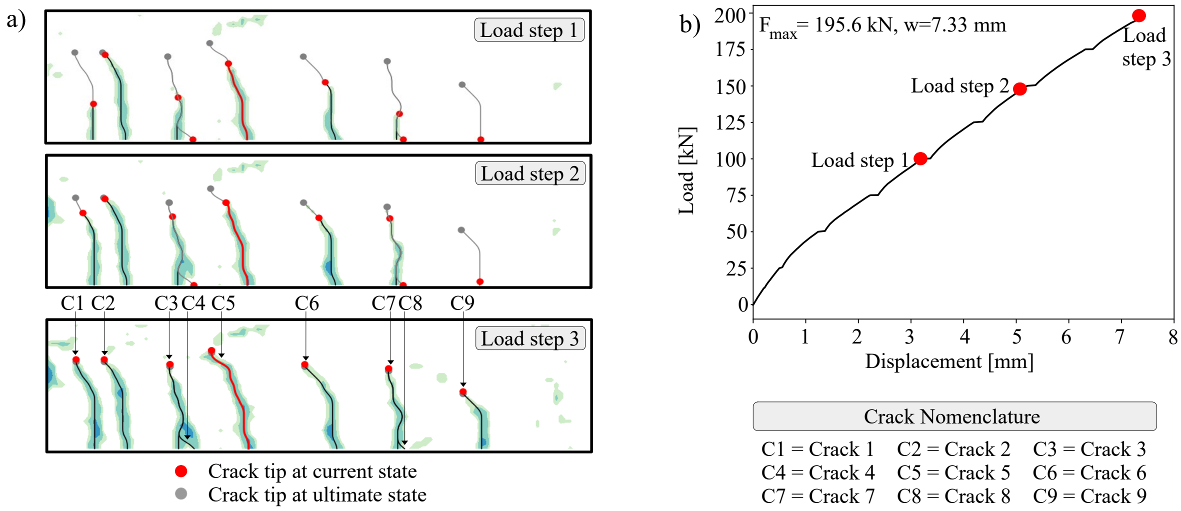

Figure 4.3: (a) Crack history tracing, (b) load deflection curve

cracks and the varying rates of crack propagation contribute to a more comprehensive understanding of crack behavior in concrete structures.

The analysis for beams B1 and B2 showcases the crack detection algorithm's capability to track and visualize the complete history of crack propagation. The ability to identify crack initiation, development, and interaction with loading conditions is crucial for understanding structural behavior and predicting failure mechanisms accurately. The results obtained from this study contribute to advancing our understanding of crack mechanics in concrete structures and can inform the design and assessment of safer and more reliable engineering structures.

4.5 Conclusions

The chapter revolves around the development of a crack identification procedure using the localized damage model and its practical application on two beams tested at the institute. The successful application of the crack detection algorithm demonstrates its effectiveness in accurately predicting all the shear cracks' initiation and propagation.

The significant outcomes achieved through the developed scheme provide valuable insights into the complex phenomena of shear crack propagation in longitudinally reinforced beams. This newfound understanding lays the foundation for enhancing mechanical and engineering design models that can predict the response of longitudinally reinforced beams more effectively.

The successful application of the crack detection algorithm on the tested beams showcases its practical significance and its potential to impact the field of concrete engineering positively. The knowledge gained from this study can be leveraged to enhance structural analysis, optimize concrete designs, and ensure the integrity and safety of construction projects.

5 Crack-centered operators

5.1 Introduction

In this chapter, the practical applications of the crack detection algorithm are discussed, showcasing its advantages in understanding the complex process of shear crack propagation. A concise overview of the model is presented in Fig. 5.1, providing a visual representation of its key components.

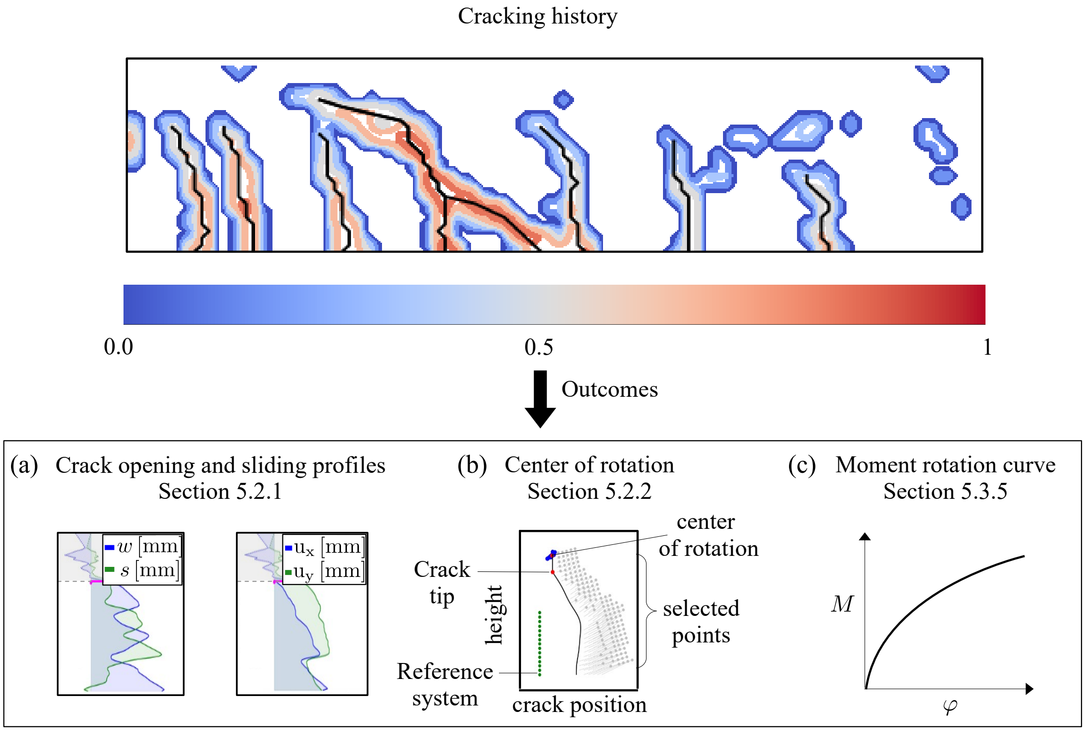

Figure 5.1: Outcomes from the crack detection scheme(a-c)

5.2 Examples of crack-centered operators

5.2.1 Crack opening and sliding evaluation

With the detected crack geometry at hand the profiles of opening and sliding along the crack path can be automatically evaluated as exemplified in Fig. 4.1c. Using the interpolation $\tilde{U}_a(\lambda, x, y)$, the global displacements are evaluated on the left and right side of a crack C with the coordinates denoted as

$$x_{CN}^{\text{left}} = X_{0;M^{\star}_{CN};N} - \Delta x,\;\; x_{CN}^{\text{right}} = X_{0;M^{\star}_{CN};N} + \Delta x, y_{CN} = X_{1;M_{CN};N}$$

$$\begin{aligned} U_{aCN}^{\text{left}} &= \tilde{U}_a(\lambda, x = x_{CN}^{\text{left}}, y = y_{CN}) \\ U_{aCN}^{\text{right}} &= \tilde{U}_a(\lambda, x = x_{CN}^{\text{right}}, y = y_{CN}) \end{aligned} \tag{5.1}$$

where, Δx is the distance between the crack ligament and the points on each side of the crack. This length is specified depending on the resolution of the DIC measurement. The displacement jump across the crack is then obtained as

$$\Delta U_{aCN} = U_{aCN}^{\text{right}} - U_{aCN}^{\text{left}} \tag{5.2}$$

The global displacement jump profiles are transformed to local kinematic profiles

$$\Delta U_{bCN}^{\ell} = T_{CNab} \Delta U_{aCN}, \tag{5.3}$$

where T_{CNab} represents the transformation matrix into the crack path coordinates. These coordinates are constructed from the derivatives of the spline representation of the crack path. The opening and sliding profiles for crack C are extracted using the dimensional index $b \in [0, 1]$, i.e.

$$w_{CN} = \Delta U_{b=0;CN}^{\ell}, \;\text{and}\; s_{CN} = \Delta U_{b=1;CN}^{\ell}. \tag{5.4}$$

A quantified example of the global relative displacement along the crack path and the opening and sliding profiles is shown in Fig. 4.1c.

As indicated in Fig. 4.1d, the automatically determined profiles allow for further data processing by applying the constitutive laws for concrete in compression and tension, crack-bridge and dowel action, and aggregate interlock at the crack faces. The example of quantified local and global stress profiles indicates further possible steps in automated crack data processing. This feature will be exploited in the next chapter, quantifying the stress transfer mechanisms using existing constitutive hypotheses and validating them in terms of the global cross-sectional equilibrium conditions.

5.2.2 Quantification of rotational kinematics

Another example of crack-centered operator is focusing on the hypothesis of rotational kinematics, which is the basis of existing mechanical and analytical shear models. These models postulate an existence of a center of rotation between two neighbouring teeth. This assumption constitutes the basis for closed form solutions for an intermediate and ultimate force transmitted by a shear crack. A detailed analysis of local displacement fields in the vicinity of the automatically detected crack can be used to examine the relevance of the rotational kinematics in a broad range of crack configurations.

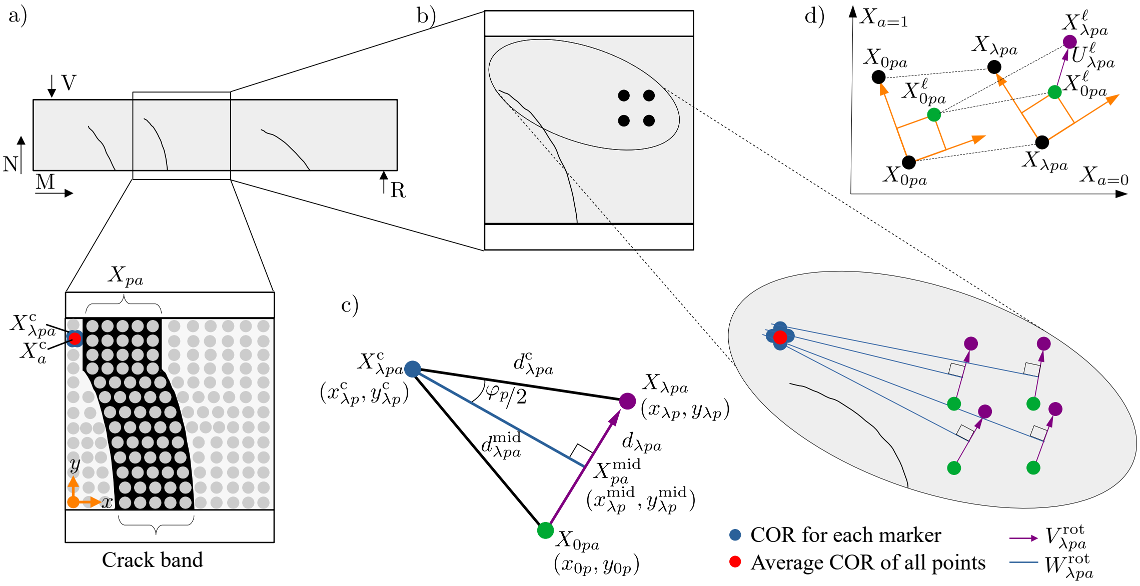

Figure 5.2: Identification of the center of rotation (a) reference system on the left teeth and band of points on right teeth; (b) zoom into the rotating teeth; (c) notation of the displacement and radial vectors with the rotation angle φ_p, (d) DIC aligned grid

The operator evaluating this kinematic assumption has been implemented into the present framework as an optimization problem aiming to isolate the center of rotation (COR) from the relative movement of two neighbouring teeth. The applied procedure is depicted in Fig. 5.2. Assuming the rigidity, a local reference system is defined on the left plate. Then, a band of points X_{Cpa} on the right plate along the crack C is defined with a specified spacing and width. To factor out the rigid body motion from the analysis, a reference system is defined by choosing two points on the left plate of a crack C

$$[X^{\mathrm{r}0}_{Ca}(\lambda), X^{\mathrm{r}1}_{Ca}(\lambda)] \tag{5.5}$$

that change their position during the loading as indicated by the parameter λ. These points are used to rotate displacement from the global system to the reference system defined on the left plate $T^{\mathrm{r}}_{Cab}(\lambda)$ by applying standard procedures of cross product with an out-of-plane vector and normalizing the base vectors of to obtain an orthonormal base. With the reference system at hand, the movement trajectories of the points on the right plate in global coordinates, i.e. $X_{Cpa}(\lambda)$, can be pulled to the reference system origin

$$X^{\mathrm{pull}}_{Cpa}(\lambda) = X_{Cpa}(\lambda) - X^{\mathrm{r0}}_{Ca}(\lambda), \tag{5.6}$$

and then rotated to the movement trajectories relative to the reference system by applying the transformation matrix

$$X^{\ell}_{Cpb}(\lambda) = X^{\mathrm{pull}}_{Cpa}(\lambda)\, T^{\mathrm{r}}_{Cab}(\lambda). \tag{5.7}$$

To shorten the symbols in further equations the dependency on λ is not explicitly stated and the initial and intermediate positions of the points p are explicitly denoted as

$$X^{\ell_0}_{Cpa} = X^{\ell}_{Cpa}(0), \quad X^{\ell_\lambda}_{Cpa} = X^{\ell}_{Cpa}(\lambda). \tag{5.8}$$

Then, the local displacement vectors can be expressed as

$$U^{\ell_\lambda}_{Cpa} = X^{\ell_\lambda}_{Cpa} - X^{\ell_0}_{Cpa}. \tag{5.9}$$

The graphical representation of the described procedure is sketched in Fig. 5.2d.

The displacement vector and the resulting center of rotation (COR) is plotted with respect to the local reference system. This local reference system is defined to be existing on the left side of the studied crack and all points in between the teeth are selected (X_{pa}) to inspect their movement along the loading history (see Fig. 5.2(ab)). Then the center of rotation for all these points is obtained as an optimization problem where COR values for all the points are averaged to get the overall center of rotation ($\mathrm{X}^{\mathrm{c}}_{\mathrm{a}}$) for the entire tooth.

5.2.2.1 Identification of the center of rotation

The displacements on the right plate expressed relatively to the fixed left plate in (5.9) can be used to answer the question, whether or not the movement of the points on the right plate can be expressed as a mutual rotation of both plates around an unknown center of rotation. If the points $X_{Cpa}^{\ell_\lambda}$ rotate around a common center, then all lines perpendicular to the displacement vector $U_{Cpa}^{\ell_\lambda}$, starting at the midpoints

$$X_{Cpa}^{\mathrm{mid}} = \frac{1}{2}\left(X_{Cpa}^{\ell_0} + X_{Cpa}^{\ell_\lambda}\right) \tag{5.10}$$

represent the radial lines and, thus, must intersect in a single point X_{Ca}^{cor}. The situation is sketched in Fig. 5.2bc. The lines perpendicular to the displacement of individual points can be expressed as

$$X_{Cpa}^{\mathrm{line}}(\eta_P) = X_{Cpa}^{\mathrm{mid}} + \eta_p W_{Cpa}, \tag{5.11}$$

where the perpendicular line vector is constructed using the displacement (5.9) to obtain

$$W_{Cpa} = \left[U_{Cp;a=1}^{\ell_\lambda}, -U_{Cp;a=0}^{\ell_\lambda}\right]. \tag{5.12}$$

The scalar parameters η_p representing the position along the perpendicular lines (5.11) can be determined by defining an optimization problem

$$\begin{gathered} d_{pq}^2 = \left(X_{Cpa}^{\mathrm{line}}(\eta_p) - X_{Cqa}^{\mathrm{line}}(\eta_q)\right)^2 \\ \min_{\eta_p} \sum_p \sum_q d_{pq}^2 \rightarrow \hat{\eta}_p, \;\; p,q \in [0, n_p - 1] \end{gathered} \tag{5.13}$$

minimizing the square of distances between the points on all combinations of lines p and q. This task is efficiently solved using the quasi-Newton method BFGS provided in the `scipy` package [Nocedal and Wright, 1999]. The obtained values of $\hat{\eta}_P$ are then substituted in (5.11) to obtain the cloud of points $X_{Cpa}^{\mathrm{line}}(\hat{\eta}_p)$ illustrated in blue in Fig. 5.2c. The smaller the cloud of these points, the more appropriate the assumption on rotational movement of the points p. To obtain a single value of the center of rotation, an averaging operation is introduced using index notation as

$$X_{Ca}^{\text{cor}} = \frac{1}{n_p}\,\delta_{pp} X_{Cpa}^{\text{line}}(\hat{\eta}_p), \tag{5.14}$$

where δ_{pp} again denotes Kronecker delta.

5.2.2.2 Angle of rotation between two teeth

Once the displacement field, crack paths, and the COR of a crack is available, it is possible to evaluate the angle of rotation φ between the left and right teeth using simple trigonometry as illustrated in Fig. 5.2c. To evaluate φ, the distance between the midpoint of the displacement line X_{Pa}^{mid} from X_{Ca}^{cor} and from the intermediate position $X_{Cpa}^{\ell\lambda}$ are written as

$$\begin{aligned} V_{Cpa}^{\text{mid}} &= X_{Cpa}^{\text{cor}} - X_{Cpa}^{\text{mid}}, \\ V_{Cpa}^{\ell\lambda} &= X_{Cpa}^{\ell\lambda} - X_{Cpa}^{\text{mid}}. \end{aligned} \tag{5.15}$$

The rotation angle around the center of the points p shown in Fig. 5.2b is obtained as

$$\varphi_{Cp} = \frac{1}{2}\arctan\left(\frac{V_{Cpa}^{\ell\lambda}}{V_{Cpa}^{\text{mid}}}\right), \tag{5.16}$$

with an average angle

$$\varphi_C = \frac{1}{n_p}\delta_{pp}\,\varphi_{Cp}. \tag{5.17}$$

5.2.3 Remark

As illustrated later in Section 5.3.3 and 5.3.5, the described procedures can be readily used to trace the center of rotation during the cracking process and to construct the moment-rotation curves in all cracks.

5.3 Elementary studies

To demonstrate the main features and outputs of the developed crack detection algorithm, elementary studies are presented in this section. The studies highlight the main outcomes of the crack detection scheme i.e. the automatic tracking of the crack propagation, the evaluation of the opening (w) and sliding (s) propagation along all cracks, the identification and tracking of the center of rotation between two neighboring cracks, and the evaluation of the moment rotation curves.

5.3.1 Profiles of crack opening and sliding

With the cracking history determined for beam B1, the evolution of the profiles of crack opening and sliding has been quantified using the procedure described in Section 5.2.1. The results for the three considered load steps are visualized in Fig. 5.3. The values are plotted along a vertical projection of the ligaments up to the crack tip. Above the crack tip, the normal and shear strain profiles along the uncracked ligament are plotted on a gray background. The distance between the points used in this evaluation was $\Delta x = 29$ mm[1]. The obtained profiles are highly nonlinear with significant variations over the cross-sectional height. The effect of crack bridging and dowel action can be recognized at the position of the reinforcement. Moreover, the ratio between opening and slip changes depending on the position along the beam. While the crack C2 exhibits the largest crack opening at the bottom of the cross section at load step 3, the cracks C8 and C9 have the largest crack opening within the cross section. The sliding profile for crack C8 reaches the largest values of all cracks, indicating that it is the critical crack.

The comparison of the detected crack patterns and load deflection curves obtained for beams B1 and B2 is shown in Fig. 5.4. Opening and sliding profiles are depicted for three selected cracks as well. Regarding beam B2, it can be seen that the location of the critical crack with the maximum sliding and opening at the ultimate load is almost in the middle of the span. The inclination of this crack with respect to the vertical axis is smaller in comparison to the critical crack in beam B1. In both beams, the critical crack was the one that propagated deepest into the compression zone.

5.3.2 Verification of crack opening and sliding profiles

To verify the evaluation of crack opening and sliding obtained using the procedure described in Section 5.2.1, a comparative analysis with the manual inspection using the DIC software is performed [gom, 2019]. The manually evaluation of the opening and sliding at a point along the crack is depicted in Fig. 5.5a. As shown in Fig. 5.5a, the manual inspection of the opening and sliding has been performed at the bottom of the cross

---

[1] This value was chosen based on parametric studies with varied values of Δx. While a stable value of crack opening was obtained already for $\Delta x \approx 10$ mm, stabilized value of slip has been obtained for $\Delta x \approx 29$ mm.

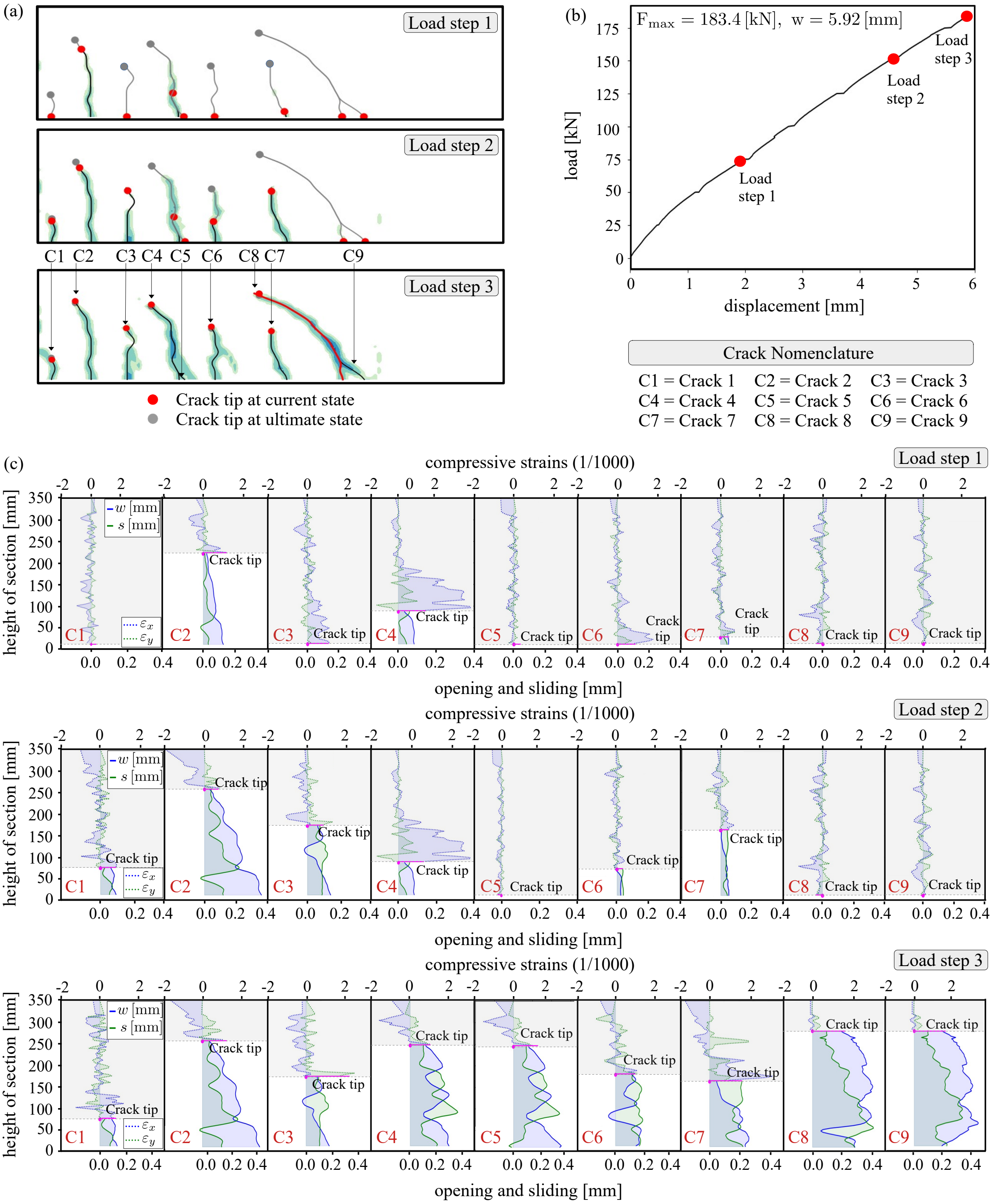

Figure 5.3: (a) Crack history tracing, (b) load deflection curve, (c) crack opening and sliding profiles of all cracks in beam 1 at three loading steps

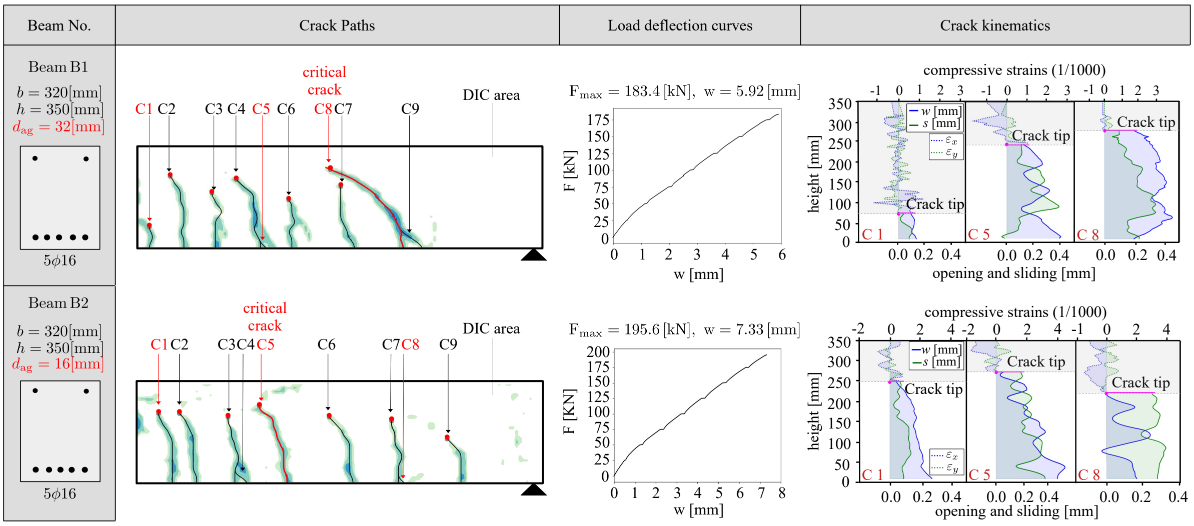

Figure 5.4: Crack paths, load deflection curves and crack kinematics for the two studied beams

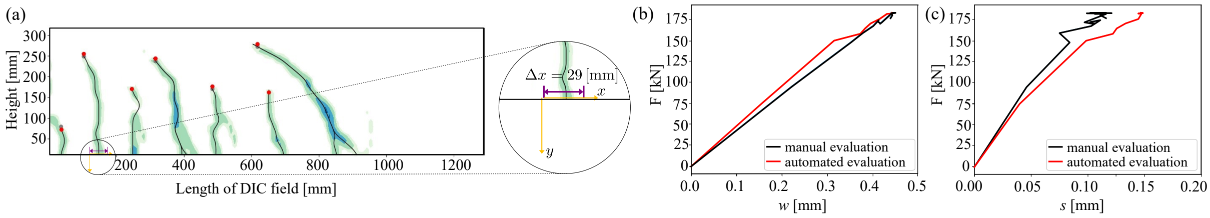

Figure 5.5: Comparison of the opening and sliding evaluated using the automated crack detection tool and the manual inspection from DIC data: (a) crack pattern in beam B1 with the marked location of the inspected opening and sliding histories; (b) crack opening history quantified at level of steel reinforcement; (c) crack sliding history evaluated at the level of steel reinforcement

section by defining two curves parallel to the crack in the direction of crack propagation. Then a local reference system is defined such that the x-axis is normal to the crack y-axis is aligned to the crack path to quantify the relative displacement jump. To measure the opening and sliding on the same distance as done using the automated quantification in (5.1) the horizontal distance between the two parallel curves was set to $\Delta x = 29$ mm. The comparison between the automatically obtained values and manual inspection of

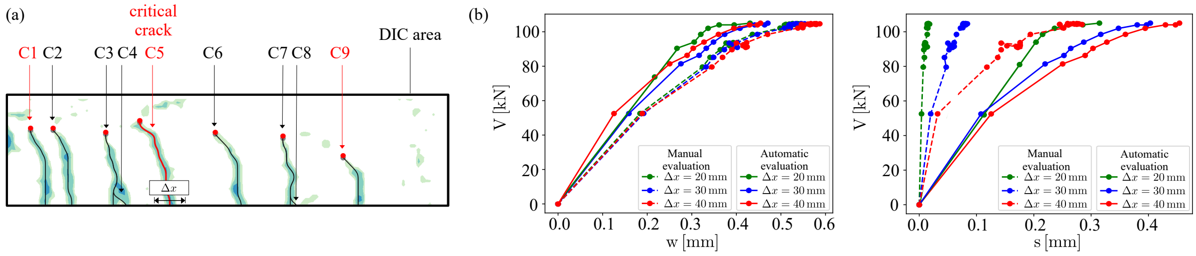

Figure 5.6: Comparison of the opening and sliding evaluated using the automated crack detection tool and the manual inspection from DIC data: (a) crack pattern in beam B2 with the marked location of the inspected opening and sliding histories; (b) crack opening history quantified for the critical crack at the level of steel reinforcement; (c) crack sliding history for the critical crack evaluated at the level of steel reinforcement

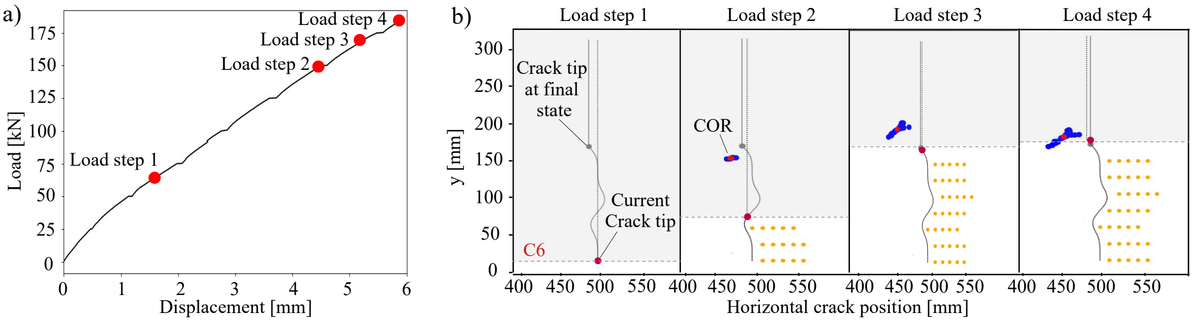

Figure 5.7: Center of rotation identified at four stages of propagating crack C6 in beam B1: (a) load deflection curve, (b) propagating crack with the points in the right tooth that were used for the identification of the center of rotation

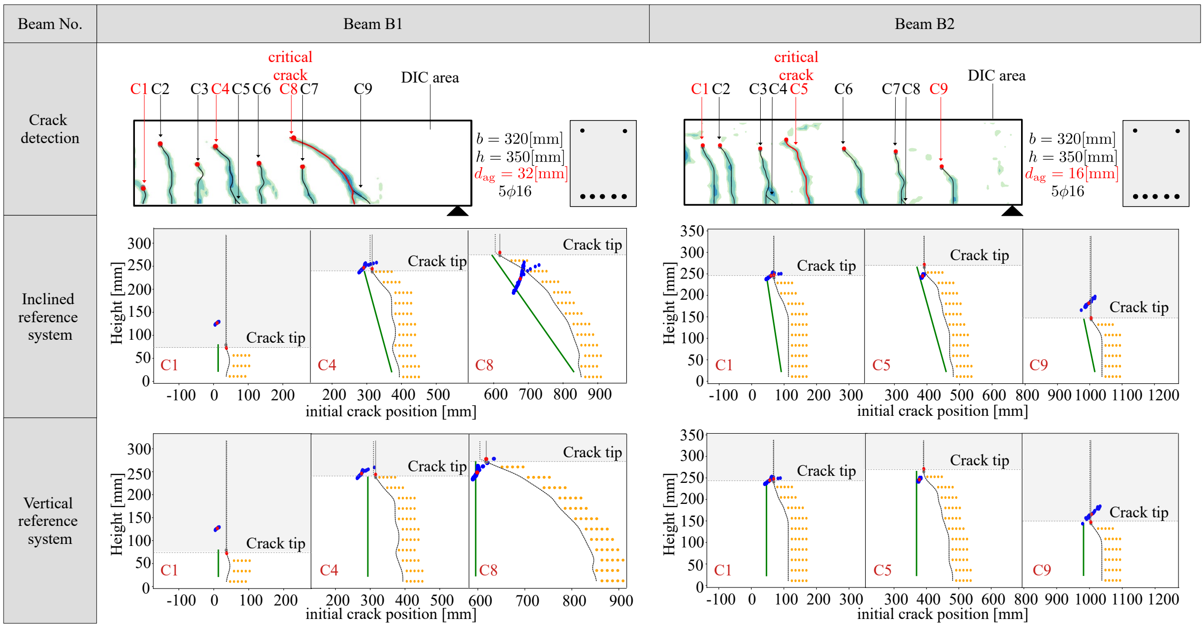

Figure 5.8: Centers of rotations for selected cracks in beam B1 and beam B2 at the ultimate state

opening and sliding is presented for one point in Fig. 5.5. Apparently, the results obtained for opening are almost equal, while the slip obtained using automated evaluation is slightly larger compared to the manual inspection. It should be noted that the results obtained by crack detector are more trustworthy due to the fact that the data obtained from the manual inspection are dependent on multiple factors such as the direction of the local reference system, direction of the curves drawn for inspection and the distance between the two curves. Due to these reasons, the manual inspected results are more prone to human error.

To illustrate the limitations of manual evaluation, another comparison of crack opening and sliding results obtained from the crack detection tool and manual evaluation is performed. The critical crack of beam B2 is chosen, and three different evaluation distances are selected (see Fig. 5.6). Examination of the crack opening profiles for all three distances reveals that the trend of values obtained from both manual and automatic crack detection tools is the same, and that these values are roughly similar and independent of the evaluation distance chosen. However, in contrast to the crack sliding profiles, the range in sliding values obtained from manual inspection is quite substantial, with each of the three distances yielding a distinct value. In contrast, the numbers obtained from the crack detection tool show a closely spaced trend, highlighting the reliance of manual inspection on several elements, such as the selection of curve line for evaluation and the location of local axes, which are subject to human error. As evident from the sliding results, the crack identification tool is not dependent on these parameters, making it more resilient and suitable for crack kinematic evaluation in a shear zone.

5.3.3 Identification and tracing of the center of rotation

The evaluation of the center of rotation between two neighboring teeth presented in Section 5.2.1 is illustrated in Fig. 5.7 for crack C6 in beam B1 at four load levels. This crack started at lower load level so that it was chosen to show correspondence between the crack propagation states and the corresponding positions of the center of rotation (COR). The magenta marker in the figure shows the current crack tip, while the grey marker illustrates the crack tip at the ultimate state. The orange dots along the crack depict the points X_{Cpa} selected for the identification of the center of rotation. The blue points in the vicinity of the crack tip depict the cloud of closest points on the radial lines X_{Cpa}^{line} introduced in (5.11) associated with each point p. The red marker is the average position within the cloud and represents the identified center of rotation. At load step 1, there is no center of rotation as the crack has not yet initiated. When the load increases to load step 2 with already propagating crack, a clearly identified center of rotation with a small blue cloud appears diagonally upwards with respect to the crack tip. At load step 3, further propagation of the crack is observed with the center of rotation propagating diagonally upwards and increasing size of the blue cloud. At the final load step, the center of rotation occurs diagonally upwards from the crack tip, slightly below the position obtained at load step 3. Still, a more scattered cloud of the blue markers reveals that rotational kinematics becomes less justified. To visualize the center of rotation for all types of propagating cracks, i.e. bending, bending-shear, and shear-dominated cracks, in the two tested beams, a comparative study is presented in Fig. 5.8 showing the identified centers of rotation at the ultimate loading state. The study also highlights the impact of the choice of the reference on the evaluation of the center of rotation, considering either inclined or vertical reference frames, given by the points $X_{Ca}^{\ell_0}$ and $X_{Ca}^{\ell_1}$ introduced in (5.5), that are visualized as the green lines in the diagrams in the second and third rows of Fig. 5.8.

It can be seen that the center of rotation for all selected cracks is diagonally above the crack tip as long as the crack propagates in the tensile zone. Once the crack reaches the compression zone, the center of rotation moves diagonally below the crack tip, e.g. for critical cracks C8 in beam B1 and C5 in beam B2. This experimental finding agrees fairly well with the postulated shift of COR location during the loading process that has been hypothesized in the development of SCPT [Classen, 2020]. The choice of the reference frame is found to have no significant influence on the identified center of rotation in most of the cases shown in Fig. 5.8. Only in the case of extremely inclined cracks, such as crack C8 in beam B1, the vertical reference frame leads to a large scatter of the closest points on radial lines depicted by blue markers in Fig. 5.8. This is due to the fact that crack C7 lies between the vertical reference frame and the selected points in the neighboring tooth of crack C8, which violates the assumption of rigid left plate.

5.3.4 Evaluation of the history trend of COR

The history of center of rotation is examined for various cracks existing within a beam and the trend of this history for each unique crack is shown and discussed. The study's goal is to contribute to the debate over the assumption about the presence of a center of rotation used in various kinematic models. A brief glimpse on the concept of evaluation can be seen in Fig 5.9. Here, two cracks with there corresponding CORs are shown (Fig. 5.9a), while the position of the crack tip and its corresponding center of rotation that will be evaluated from the crack detection tool is also depicted in Fig. 5.9b. The difference between the current crack tip and the COR will be given by:

$$\Delta_a = X_{Ca}^{\mathrm{cor}} - X_{Ca}^{\mathrm{tip}} \tag{5.18}$$

The difference will be evaluated for each crack tip during the history and its corresponding COR and the result will be presented as shown in Fig. 5.9c. The average of this difference for each crack will show the trend of COR for all cracks existing in the beam. Beam B1, B2 are presented and discussed here for the evaluation of the history trend of COR for all cracks, while the remaining beams selected for discussion in the thesis are reported and discussed in the appendix.

5.3.4.1 Beam B1

The study in Fig. 5.10 for Beam B1 show the horizontal and vertical differences between the COR and the propagating crack tip. Crack C1 is not shown here as its a very fine and short heighted crack and does not have much impact on the shear behavior. The results for crack C9 are likewise not shown here since it is a branching crack that originates from crack C8 and its occurrence occurred late in the loading history (i.e. near failure).

While looking at the trend of Δx, it can be visualized that for most of the cases the center of rotation is existing on the left side of the crack tip (refer to Fig. 5.10). As the critical crack is a pure shear-governed crack that propagates in a diagonal direction, it is evident that this difference is substantially greater for the critical crack. The average of each crack's center of rotation in grey indicates that the COR always exists horizontally away from the crack tip.

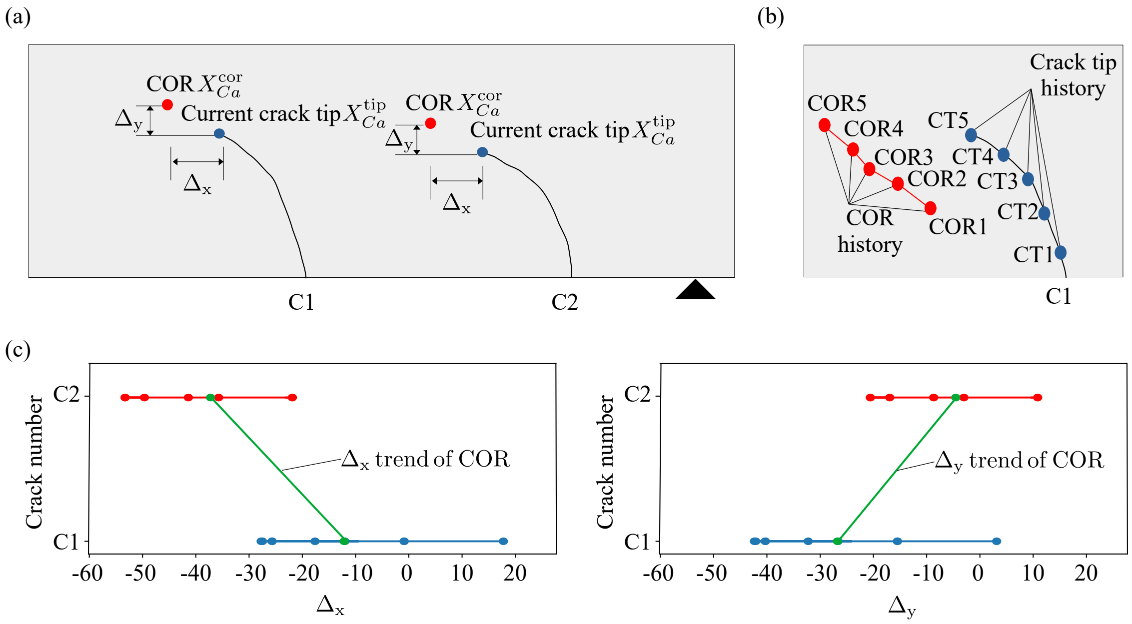

Figure 5.9: (a) Tracing of trend of COR for different cracks, (b) crack propagation and existence of COR during the history of crack C1 development, (c) horizontal and vertical difference in between the crack tip and COR for C1 and C2

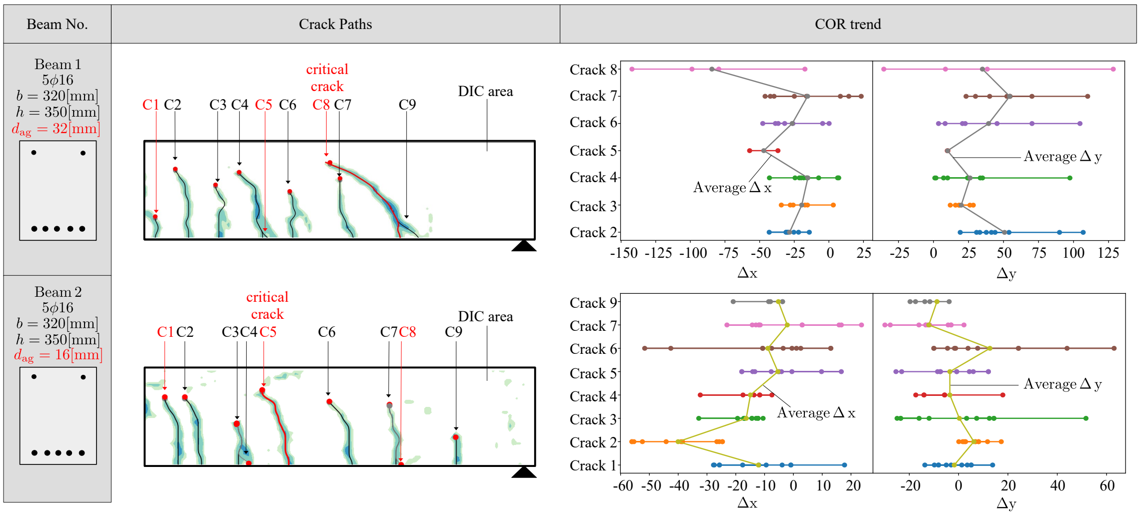

Figure 5.10: (a) Detected crack paths and the study for the trend of the center of rotation (COR)

Similarly, an examination of Δy reveals that the COR for all cracks exists vertically above the crack, whereas it is only found below the crack tip in the final loading condition of the critical crack. Here, the average of all cracks indicates that COR is always present above the crack tip.

5.3.4.2 Beam B2

The horizontal differences for beam B2 reveal that for cracks C1, C5, C6, and C7, the COR exists for some loading stages on the right side of the crack tip, whereas for all

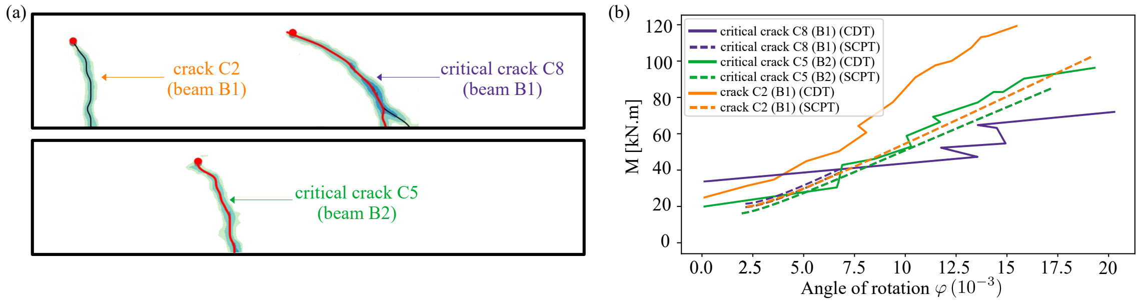

Figure 5.11: Evaluation of the moment-rotation curve: (a) three selected cracks in beams B1 and B2, (b) comparison of the moment-rotation curves with the prediction obtained using SCPT

other cracks, the COR always exists at some left of the crack tip (see Fig. 5.10). Crack C6 demonstrates a large oscillation in the existence of COR. The average of all the cracks indicates that COR can be assumed to exist prior to the crack tip.

As seen by the vertical variations, all cracks except crack C2 have COR below the crack tip at certain stages in the loading history. As crack moves from the tension zone into the compression zone, the COR is shown to migrate downward of the crack's tip.

5.3.5 Evaluation of the moment-rotation curves

As described in Section 5.2.2.2, based on the crack detection scheme the moment-rotation curves for each identified propagating crack within the beam span can be quantified. With the help of the identified center of rotation, the moment value and the rotation angle are calculated with respect to the center of rotation at each load step.

To illustrate this feature, the moment-rotation curve is evaluated for three types of cracks, two in a discontinuity region with direct strutting action (D-region), i.e. close to the load and close to the support, and one in a B-region of the beam, i.e. in the middle between load and support, where flexural shear is prevailing. The moment-rotation curves shown Fig. 5.11 start at the level corresponding to the load at which the crack started to propagate.

The moment-rotation curves obtained from the crack detection tool are compared with the predictions obtained using the shear crack propagation theory (SCPT) [Classen, 2020, Schmidt et al., 2021] in Fig. 5.11. The comparison is done for cracks C2 and C8 from beam B1 and C5 from beam B2. The initial point of the moment-rotation curve represents the onset of cracking, as identified by the crack detection tool (CDT) and predicted by the shear crack propagation theory (SCPT), while the endpoint corresponds to structural failure. For the critical crack C5 located in the B-region of beam B2 the moment-rotation curve obtained from SCPT is in a very close agreement to the curve obtained from the crack detection tool. The moment-rotation responses of two selected cracks C2 and C8 in D-regions, close to the load introduction and the support of beam B1, are either over- or underestimated, respectively.

The cracks have been selected for analysis in order to show, that the SCPT can well predict the behavior of flexural shear cracks in B-regions, while the cracks in a D-region of the beam, where the effect of shear dilatancy is significant, cannot be accurately predicted. To improve the model prediction, an extension of the SCPT is prepared to cover (i) the effect of arching-action close to the supports, (ii) the changed stress-distribution in the compression zone of D-regions, and (iii) the effect of shear dilatancy. In addition to that and with respect to beam B1, where an aggregate grain size of 32 mm was tested, the use of more refined aggregate interlock laws within the SCPT can help to further increase the accuracy of the model.

5.4 Conclusions

The developed crack detection scheme provides the possibility to automatically evaluate the opening and sliding profiles along the crack ligament, as well as the evaluation of the center of rotation directly from the DIC monitoring of the surface displacement applied to longitudinally reinforced concrete beams. The incorporation of damage models within the developed scheme improves the resolution of the DIC data in the localization zones of crack ligaments, which allows for a more accurate and robust detection of propagating cracks.

The outcomes of the developed scheme pave the way for a sound understanding to the complex shear crack propagation phenomena in longitudinally reinforced beams, which can be used to effectively support further development of mechanical and engineering design models that predict the response of longitudinally reinforced beams.

With the possibility to evaluate the crack kinematics and to identify the center of rotation of two neighbouring teeth, the main kinematic assumptions in the existing mechanical and analytical models of shear zones [Reineck, 1990, Cavagnis et al., 2018b, Tran, 2020, Classen, 2020] can be evaluated and refined based on further comprehensive and systematic analysis on sufficient number of tests with varied design parameters.

Moreover, the evaluation of crack opening and sliding for all propagating cracks and the strains in the uncracked ligaments can be further used to evaluate the stress transfer mechanisms, i.e. aggregate interlock [Bazant and Gambarova, 1980, Walraven, 1980], dowel action [Baumann and Rüsch, 1970b, Bosbach, 2024], and the stresses in the fracture process zone [Hordijk, 1992, Jirásek, 2011], and the compressive zone [Kupfer and Gerstle, 1973, Classen, 2020], by incorporating constitutive laws existing in the literature, which will provide the basis for further refinements of the constitutive hypotheses by considering the cross-sectional equilibrium conditions in combination with the DIC processed data.

Part III

Quantification of stress transfer mechanisms in assumed in shear crack models

6 Evaluation of stress transfer mechanisms

6.1 Introduction

As previously mentioned, several analytical models have been proposed in the literature, but a consensus on their validity has yet to be reached among the scientific community. Therefore, the focus of this chapter is to employ existing constitutive laws that incorporate measured crack opening and sliding kinematics to evaluate the stress distribution between shear cracks. This study aims to provide sound data for the validation of the current constitutive laws and propose refinements that enable better analysis of the governing mechanisms of shear crack failure.

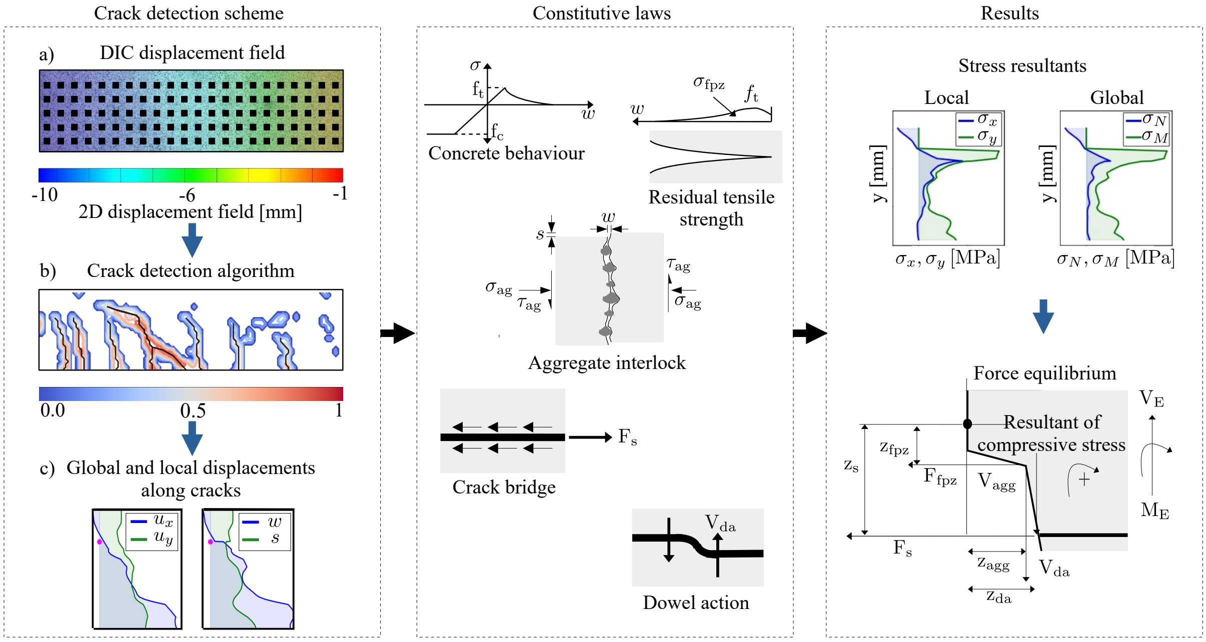

Figure 6.1: Conceptualization of the proposed model

The developed damage based crack detection tool (DCDT) takes 2D displacement field obtained from the DIC images as an input and detects cracks from the crack detection scheme. The cracks are plotted at the ridges of maximal damage, allowing the history of crack opening and sliding kinematics to be evaluated. For further study on the crack detection scheme see Fig. 6.1. On the basis of the assessed crack kinematics, one may easily derive the stress resultants by applying simple constitutive laws available in the

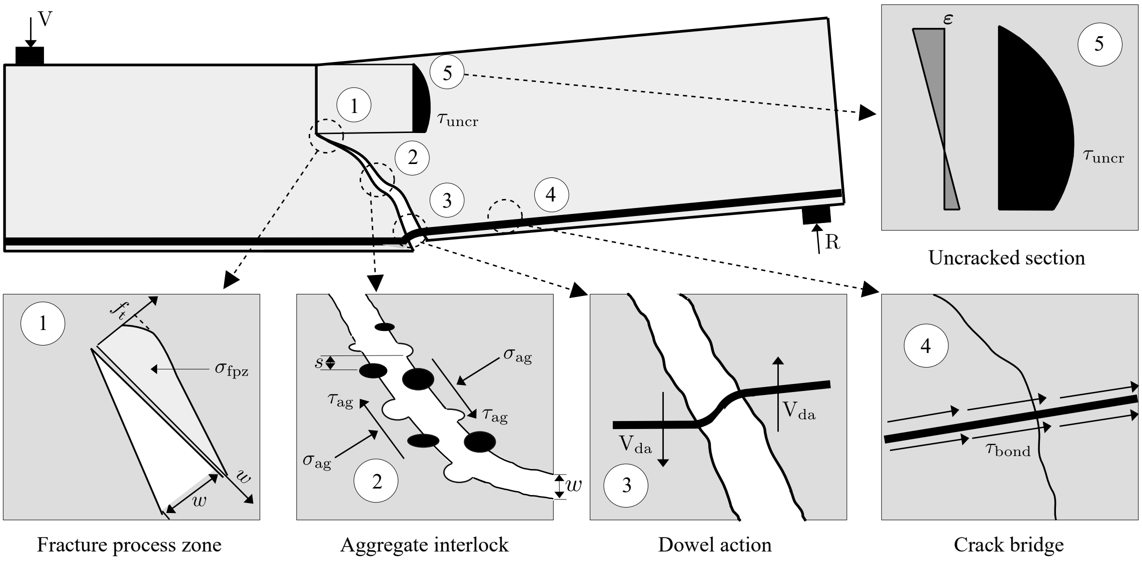

Figure 6.2: Interacting effects in a longitudinally reinforced concrete beam

literature, as well as the internal forces equilibrium along the crack by integrating the stress resultants (see Fig. 6.1)

6.2 Stress transfer mechanisms along cracks

The existing constitutive laws governing the stress transfer mechanisms across a shear crack take crack opening and sliding as an input parameter and evaluate the stress contributions along the crack for each individual action i.e., fracture process zone, aggregate interlock, dowel action, crack bridge and contribution of uncracked section etc. These interacting effects are schematically visualized in Fig. 6.2, whereas the constitutive laws are discussed below:

6.2.1 Fracture process zone

Concrete cracking causes the formation of a fracture process zone (FPZ), where tensile stresses can be transmitted across cracks up to a certain crack width. Several approaches exist in the literature establishing the relationship between residual tensile stresses and the crack opening. One of the first developed approaches to consider this action reads as [Reinhardt, 1984]:

$$\sigma_{\mathrm{fpz}} = f_{\mathrm{t}} \left[1 - \left(\frac{w}{w_{\mathrm{cr}}} \right)^{0.31} \right] \tag{6.1}$$

In this equation, $f_{\mathrm{t}}, w, w_{\mathrm{cr}}$ represents the tensile strength of concrete, crack opening and critical crack opening beyond which no stress is transferred. where,

$$w_{\mathrm{cr}} = 4.226 \frac{G_{\mathrm{f}}}{f_{\mathrm{t}}} \tag{6.2}$$

and, G_{f} denotes the fracture energy that represents the energy dissipated during opening of the crack. This energy is mainly dependent on the compressive strength of concrete and the maximum aggregate size. Based on the Model code [Code, 1990], the fracture energy can be obtained by:

$$G_{\mathrm{f}} = G_{\mathrm{f0}} \left(\frac{f_{\mathrm{c}}}{10} \right)^{0.7} \tag{6.3}$$

here, G_{f0} is the base value of the fracture energy that depends on the maximum aggregate size of a concrete mix. Nevertheless, the dependency on the maximum aggregate size was removed from the model code 2010 to redefine the fracture energy. So,

$$G_{\mathrm{f}} = 0.073 {f_{\mathrm{c}}}^{0.18} \tag{6.4}$$

This expression in model code was later modified on the basis of the experimental data [Marí et al., 2015]. Hence:

$$G_{\mathrm{f}} = 0.028 f_{\mathrm{c}}^{0.18} d_{\mathrm{ag}}^{0.32} \tag{6.5}$$

where, $f_{\mathrm{c}}, d_{\mathrm{ag}}$ is the compressive strength of concrete and size of aggregate respectively. Another well known approach to characterize the relationship between the residual tensile stress and the crack width reads as [Hordijk, 1992]:

$$\sigma_{\mathrm{fpz}} = f_{\mathrm{t}} \left[\left(1 + \left(3 \frac{w}{w_{\mathrm{cr}}} \right)^3 \right) e^{-6.93(w/w_{\mathrm{cr}})} - 0.0274 \frac{w}{w_{\mathrm{cr}}} \right] \tag{6.6}$$

here, $w_{\mathrm{cr}} = 5.14 G_{\mathrm{f}}/f_{\mathrm{t}}$ is the limit of the crack width whereas the fracture energy G_{f} can be calculated from one of the above mentioned equations.

The stress crack opening relationship can also be estimated by a bilinear law in Model code 2010 [Taerwe et al., 2013], written as:

$$\begin{aligned} \sigma_{\mathrm{fpz}} &= f_{\mathrm{t}} \left(1 - 0.8 \frac{w}{w_1} \right) \mathrm{for}\, w \leq w_1 \\ \sigma_{\mathrm{fpz}} &= f_{\mathrm{t}} \left(0.25 - 0.05 \frac{w}{w_1} \right) \mathrm{for}\, w_1 < w \leq w_{\mathrm{cr}} \end{aligned} \tag{6.7}$$

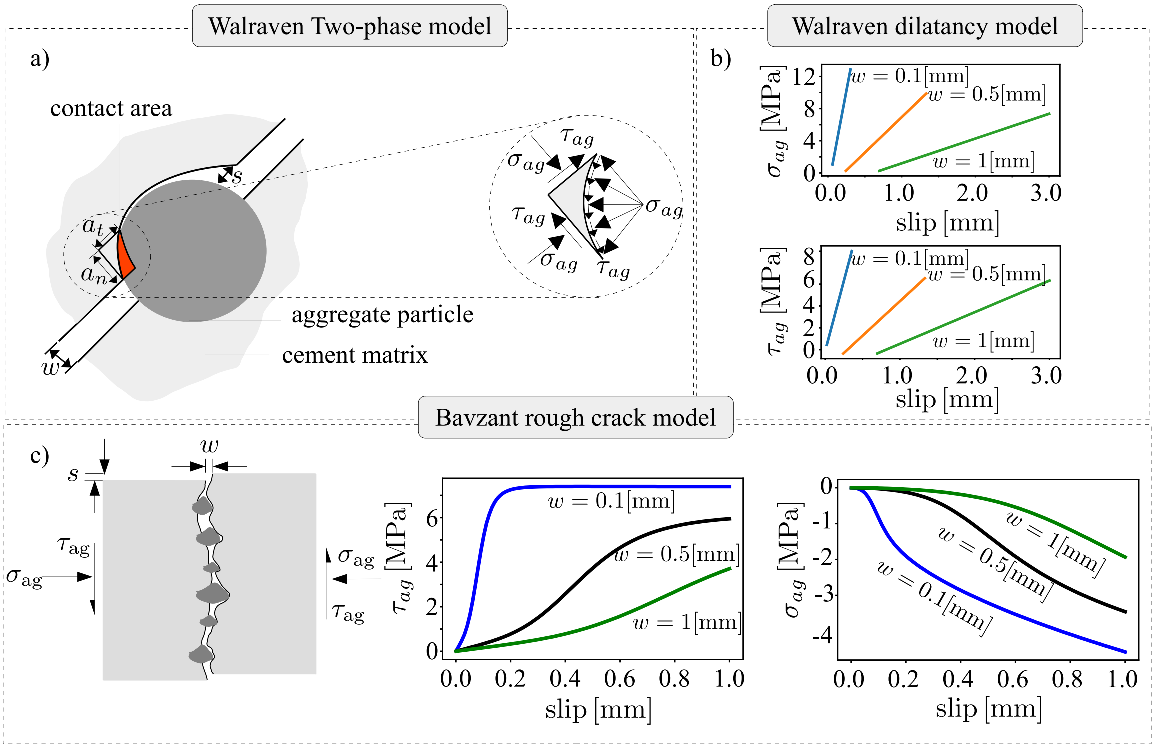

Figure 6.3: Aggregate interlock models

To account for this concrete softening tendency, we can also write the following equation:

$$\sigma_{\mathrm{fpz}} = f_{\mathrm{t}} \exp\left[-f_{\mathrm{t}}\left(\frac{w - w_{\mathrm{cr}}}{G_{\mathrm{f}}}\right)\right] \tag{6.8}$$

6.2.2 Aggregate interlock

The displacement of crack faces with respect to each other is termed as aggregate interlock [Walraven, 1980]. In order to investigate the aggregate interlock action, experiments were conducted by testing double notched specimens under biaxial testing machine [Jacobsen et al., 2012]. Cracks were discovered to propagate vertically at first because the opening is more pronounced at the crack tip [Huber et al., 2016]. The corresponding normal stresses due to these openings become significantly lower than the shear stresses in the region of aggregate interlocking mechanism due to the governing slip displacement [Jacobsen et al., 2012]. Therefore, the shear stresses are prominent in the region of aggregate interlock. However, when the crack surfaces slice against each other the aggregate interlock with the cement matrix of the opposite surface results in increase of shear strength. There are many constitutive laws in the literature that can be used to take into account the interlocking actions of the aggregate. Here, a short summary of some of these models is discussed.

6.2.2.0.1 Walraven two phase model Walraven suggested a two-phase model in which the aggregates are treated as rigid spheres and the cement matrix is considered to exhibit rigid plastic stress-strain behavior. In the model, the size of the contact area in between the cement matrix and the aggregate particles seems to be mainly dependent on the crack kinematics (i.e. w, s), aggregate size (d_{ag}), and the ratio between the volume of the concrete (p_k) and the total volume of the aggregate particles. So, the relationship for estimating the normal and shear stresses in the interface reads as (Fig. 6.3a):

$$\begin{aligned} \sigma_{ag} &= \sigma_{pu}(A_x - \mu A_y) \\ \tau_{ag} &= \sigma_{pu}(A_y + \mu A_x) \end{aligned} \tag{6.9}$$

here, μ is the friction coefficient between the aggregate and the cement matrix, σ_{pu} refers to the yield strength of the cement matrix as a function of the cubic compressive strength of concrete (f_c) such that $\sigma_{pu} = 6.39 f_c^{0.56}$, and A_y, A_x refers to the contact areas between aggregate particles and cement matrix perpendicular and parallel to the crack surface.

6.2.2.0.2 Walraven crack dilatancy model Walraven has also developed, based on regression analysis, an expression that fits the experimental data. The suggested set of equations does not account for the aggregate scale effect, and the only variable is the cube compressive strength. The formula for the curve that best fits the experimental results as presented by Walraven is (Fig. 6.3b):

$$\begin{aligned} \sigma_{ag} &= -\frac{f_c}{20} + \left[1.8w^{-0.80} + \left(0.234w^{-0.707} - 0.20\right) f_c\right] s \\ \tau_{ag} &= -\frac{f_c}{20} + \left[1.35w^{-0.63} + \left(0.191w^{-0.552} - 0.15\right) f_c\right] s \end{aligned} \tag{6.10}$$

where, w, s depicts the crack opening and sliding respectively.

6.2.2.0.3 Rough crack model Bazant proposed a rough crack model [Bažant and Gambarova, 1980] which was later refined by Gambarova [Gambarova and Karakoç, 1983] to take into account the aggregate interlock mechanism in between a concrete crack. Aggregate size appears to play a major role in transferring shear with this refined model. The devised equations are (Fig. 6.3(c)):

$$\begin{aligned} \sigma_{ag} &= --0.62\sqrt{w}\frac{r}{(1+r^2)^{0.25}} \\ \tau_{ag} &= \tau_0 \left(1 - \sqrt{\frac{2w}{d_{ag}}}\right) r \left(\frac{a_3 + a_4\|r\|^3}{1 + a_4 r^4}\right) \end{aligned} \tag{6.11}$$

where, $r = s/w$, $\tau_0 = 0.25f_c$, $a_3 = 2.45/\tau_0$ and $a_4 = 2.44(1 - 4/\tau_0)$. σ_{ag}, τ_{ag}, and d_{ag} represents the normal stresses, shear stresses due to aggregate interlock and size of aggregate, respectively.

6.2.3 Dowel action

Dowel action is the capacity of longitudinal reinforcing bars to transfer forces perpendicular to their axis. Dowel action occurs as a consequence of tangential displacement in the crack plane between the longitudinally reinforced steel and the surrounding concrete. It generally arises at the bottom of the section where the longitudinal reinforcement for beams without shear reinforcement is present. The opening and sliding along the crack face increases with the propagation of the critical crack. Crack sliding takes place perpendicular to the axis of the longitudinal reinforcement. Furthermore, dowel crack develops along the longitudinal reinforcement as a result of increase in slip along crack surfaces. Dowel action can be identified on the basis of two mechanisms (see Fig. 6.4):

1. Transfer of shear force as a result of concrete tensile strength along the longitudinal reinforcement $\mathrm{V}_{\mathrm{da(I)}}$.
2. Transfer of shear force due to deformation of the longitudinal reinforcement $\mathrm{V}_{\mathrm{da(II)}}$.

It should be noted, that the total dowel force is not the sum of these two actions. Moreover, depending on the specimen characteristics, one of these processes will be dominant in shear transfer action (i.e. $\mathrm{V}_{\mathrm{da(I)}}$ or $\mathrm{V}_{\mathrm{da(II)}}$). The information presented in Fig. 6.4 may be used to calculate the equilibrium of forces acting at the longitudinal reinforcement. Hence,

$$\mathrm{V}_{\mathrm{da(II)}} = \frac{2M}{l} \tag{6.12}$$

Based on the assumption that the capacity of the this mechanism is limited by the development of plastic hinges in the longitudinally reinforcing bars, the equation for calculating this action is as follows:

$$\mathrm{V}_{\mathrm{da(II)}} = \frac{4\phi_s A_s f_y}{3\pi l} = \frac{\phi^3 f_y}{3l} \tag{6.13}$$

here, ϕ_s, A_s, f_y represents the diameter of the reinforcement, area of steel and the yield strength of the longitudinal reinforcement, respectively. Importantly, the above equation reveals that the capacity of this mechanism depends heavily on the diameter of the rebars (i.e it is proportional to ϕ^3) [Košćak et al., 2022]. According to a mathematical model designed to comprehend the dowel action, the failure is governed by the crushing of

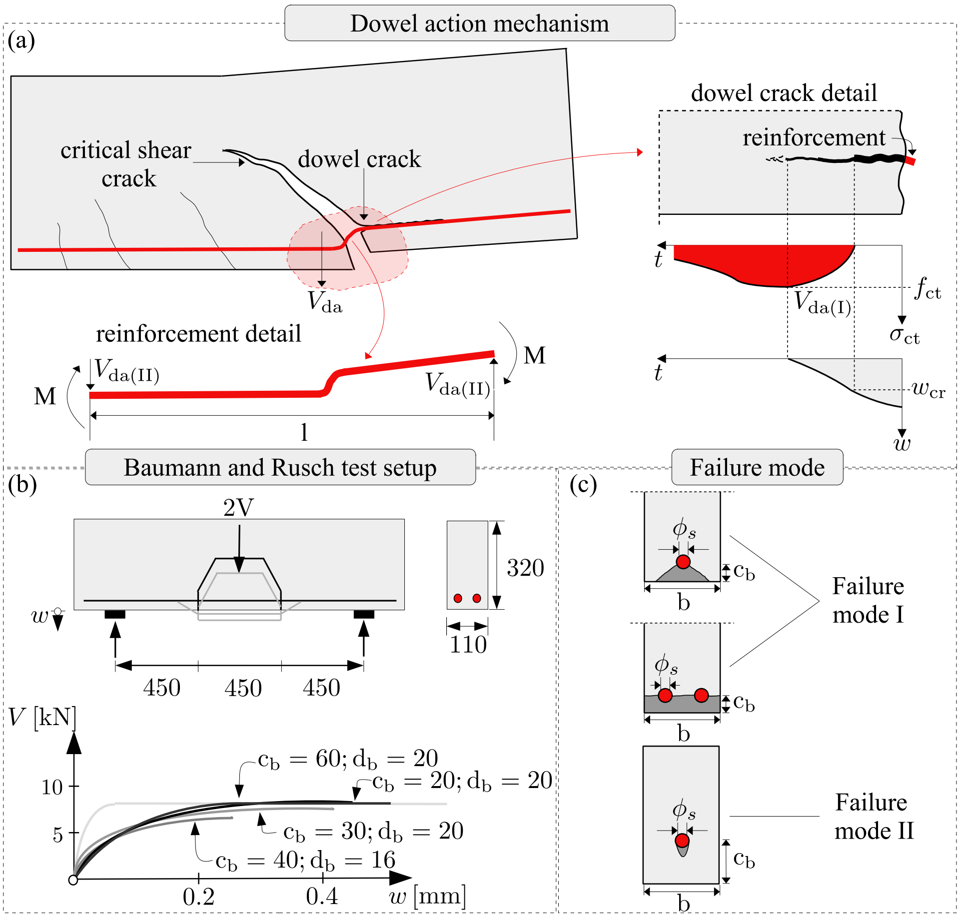

Figure 6.4: (a) Dowel action conceptualization, (b) Test setup of Baumann and Rusch for Dowel action, (c) Failure modes around the reinforcement steel

the concrete and the yielding of the longitudinal reinforcement if a sufficient concrete cover is present (failure mode II) [Vintzēleou and Tassios, 1986]. In such a situation, the shear force is regulated primarily by the deformation of the longitudinal reinforcement $V_{da(II)}$. Similarly, the failure of the specimen with a smaller concrete cover is determined by the tensile strength of the concrete and the development of a splitting crack along the reinforcement (failure mode I). The concrete tensile strength $V_{da(I)}$ is a dominant shear transfer action for beams as they have a smaller concrete cover. In the literature, a number of formulae exist to predict the dowel strength when the failure is due to splitting. A well re-known equation (see Fig. 6.4 (b)) to investigate the dowel action is proposed in [Baumann and Rüsch, 1970a]:

$$V_{da} = 1.64 b_n \phi_s (f_c)^{1/3} \tag{6.14}$$

where, b_n is the net width of the beam $(b_n = b - n\phi_s)$ and b, n are the width of the specimen and the number of reinforcing bars in the cross section, respectively. Another equation to take into account the dowel action reads as [Jimenez, 1979]:

$$V_{da} = \frac{b_n \phi_s}{n} \left(3.25 + \frac{3.79 c_m}{\frac{b_n}{n^2} + \phi_s} \right) \tag{6.15}$$

here, c_m is the minimum concrete cover and n denotes the number of reinforcing bars. An equation was developed to account for the contribution of flexural reinforcement to the punching shear strength of slabs in [Fernández Ruiz et al., 2013]. This equation can be used to take into account the dowel action in beams, hence,:

$$V_{da} = n b_{ef} l_{ef} f_t \tag{6.16}$$

where, l_{ef} is the effective length of concrete and b_{ef} is the effective width per bar that is estimated by:

$$b_{ef} = \min(s_b - \phi_s; 6\phi_s; 4c_b) \tag{6.17}$$

here, s_b denotes the spacing between the bars while c_b represents the concrete cover under the bars. Another equation is presented to achieve equilibrium between the tensile stresses acting between the rebars along the plane of a dowel crack and the compressive stresses acting directly beneath the rebar in concrete in [Vintzēleou and Tassios, 1986]. So,:

$$V_{da} \approx 2 b_n \phi_s f_t \tag{6.18}$$

Subsequently, it was noticed that the dowel capacity is heavily influenced by the tensile strains in the longitudinal reinforcement. An equation is proposed in [Cavagnis, 2017] to account for the reduction in tensile strength caused by the tensile strain.

$$V_{da} = n b_{ef} l_{ef} k_b f_t \tag{6.19}$$

where, k_b represents the strength reduction factor that follows a decay for increasing strains in the longitudinal reinforcement (ε_s). On the basis of the experimental data [Fernández Ruiz et al., 2010], the obtained expression for this factor reads as:

$$k_b = 0.063 \varepsilon_s^{-1/4} \leq 1 \tag{6.20}$$

6.2.4 Crack bridge action

A constant bond slip law is being considered in which force at the steel reinforcement is assumed as a square root function of a pull-out approximation. Hence it is written as:

$$P = \sqrt{w\tau E_f A_f p} \tag{6.21}$$

here, w, τ, E_f, A_f, p are horizontal crack opening, bond stress, modulus of elasticity, area, and perimeter of steel reinforcement respectively.

6.2.5 Concrete compressive behavior

In order to take into account, the compressive behavior of concrete, the constitutive law considering ideally plastic behavior in concrete reads as:

$$\sigma = \begin{cases} -f_\mathrm{c}, \text{ for } \frac{E_\mathrm{c} w}{L_\mathrm{c}} < -f_\mathrm{c} \\ \\ \frac{E_\mathrm{c} w}{L_\mathrm{c}}, \text{ for } w \leq w_{cr} \end{cases} \tag{6.22}$$

where, $E_\mathrm{c}, L_\mathrm{c}$ are the elastic modulus of concrete and the characteristic length.

6.3 Quantification of stress mechanisms

The availability of the opening and sliding profiles along all cracks during the whole loading history can be used to assess the existing constitutive assumptions on the stress transfer mechanisms contributing to the shear force, bending moment and normal force across the localized crack. The evaluation of the stress resultants is done by integrating the stress profiles over the cross-sectional height. A direct evaluation of the shear force by integrating the shear stress profile over the crack path and the uncracked zone appears difficult because it includes several uncertainties related to an insufficient resolution of the DIC to capture the strain state in the uncracked zone.

Thus, to eliminate the major sources of uncertainty from the assessment of the stress transfer mechanisms over the localized crack, an alternative approach quantifying the bending with respect to the position of the compressive force in the uncracked ligament is shown in Fig. 6.5. The cracks detected using the crack detection scheme and the crack path and its damage profile for crack C5 at the ultimate load are shown in Fig. 6.5a. Based on the obtained crack damage profile, the local and global crack opening and sliding profiles are evaluated (see Fig. 6.5b). The corresponding stress profile obtained by employing constitutive laws currently proposed in the literature, that were explained in Sec.6.2 is presented in Fig. 6.5c.

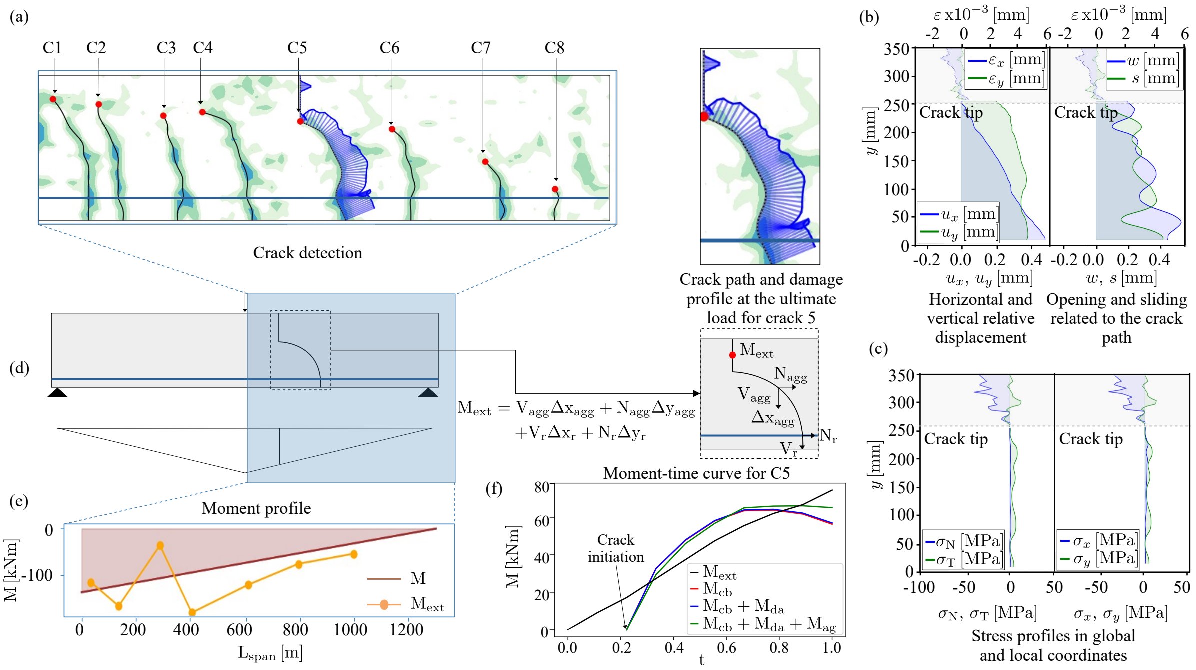

Figure 6.5: Validation of stress transfer mechanisms: (a) crack identification from the crack detection tool, crack path and damage profile from crack 3; (b) opening and sliding profiles in local and global coordinates; (c) stress profile obtained from the constitutive laws; (d) moment profile evaluation concept; (e) moment profile along the beam with the comparison of external and internal values of moment; (f) moment versus load factor curve for crack 5.

Instead of assessing the shear force obtained from the displayed stress profiles, the moment equilibrium is used to validate the constitutive assumption as illustrated in Fig. 6.5d. The external bending moment M_{ext} evaluated at the location of the resultant of the compression stress in the uncracked part of the ligament above the crack tip must be equal to the moment contributions of the aggregate interlock and of the steel reinforcement related to this point. The plausibility of the currently used constitutive assumptions is checked along the loading history for the crack C5 by showing the external moment M_{ext} and the internal moment, due to the three named stress transfer mechanisms in Fig. 6.5f. A comparison of the of the internal and external moments for all cracks at the ultimate state is depicted in Fig. 6.5e.

6.3.1 Beam B1

The damage profiles, local and global stress results, and the horizontal force equilibrium for all primary cracks found by the crack detection tool for beam B1 are reported in Fig. 6.6.

By analyzing the damage profiles in detail, we can determine that crack C6 is the critical crack since it has a high damage value and has propagated far into the compressive zone at the ultimate state. In addition, the stress distribution for each of the primary cracks in beam B1 is shown by the local stress resultants determined from the aforementioned constitutive laws and the associated global stresses after transformation. Horizontal force equilibrium for cracks C1, C2, C4, and C5 demonstrates that the equilibrium is violated due to the enormous force contribution in the compression zone. The cause for this large compression zone force could be due to many uncertainties associated to the DIC's poor resolution to record the strain state in the uncracked zone. In contrast, cracks C3 and C6 appear to be almost horizontally in equilibrium when compared to the rest of the primary cracks in beam B1.

The comparison of external and internal moments (resulting from incorporating crack bridge action, dowel action, and aggregate interlock) for all primary cracks propagating in beam B1 is shown in Fig. 6.7. At the ultimate condition, the internal and external moments of crack C1 appear to be near to each other. During the loading history, the starting location of the internal moment profile for this crack appears to be at $0.1t$, indicating the point of crack initiation. Additionally, it appears that the crack is governed by bending. This is also clear from the internal moment, since the contribution from crack bridging action is substantial, whilst the contributions from dowel action and aggregate interlock are minimal for this crack. The internal moment profile for crack C2 reveals that it begins late in the loading history. This crack also appears to be governed by bending, which means crack bridging action is also a major contributor to the internal moment. In this case, the external bending moment looks to be nearly twice as large as the internal bending moment. Initially, Crack C3 looks to be bending crack as well, but after propagating roughly around 0.6*t* in the loading history, it begins to be governed by shear (see Fig. 6.6, 6.7).The aggregate interlock contribution for this crack is observable beyond 0.6*t* due to its shear action-driven propagation. Crack C4's external and internal moment comparisons resemble crack C2's, it seems. The main distinction here is that, as a result of the crack's visible zigzag pattern, aggregate interlock contribution decreases at the end in Fig. 6.6. The internal moment for crack C5 is also lower in comparison to the external moment. By looking at the crack pattern for crack C6 (Fig. 6.6), one can foresee that this cracks appears to be governed by shear which is evident by high contribution of internal moment due to aggregate interlock action (see Fig. 6.7).

6.3.2 Beam B2

A similar study to understand the cracking mechanism for beam B2 is shown in Fig. 6.8. The damage profiles for all cracks demonstrate that crack C4 is the critical crack since it has an almost uniform damage profile until the crack tip. By closely inspecting the crack tips for cracks C1, C2, and C4, it is possible to see that all of these cracks have propagated deep into the compression zone at the ultimate load, but the damage profile of crack C4 is the highest among the others at this state, indicating that crack C4 is the critical crack. The ensuing local and global stress profiles for all existing cracks in the beam B2 produced by applying the previously described constitutive laws are also displayed in Fig. 6.8. In addition, the horizontal force equilibrium of each crack is reported. It can be shown that the force equilibrium for cracks C1, C2, C5, C6, C7, and C8 is not satisfied, however the state of equilibrium for cracks C2 and C3 appears to be

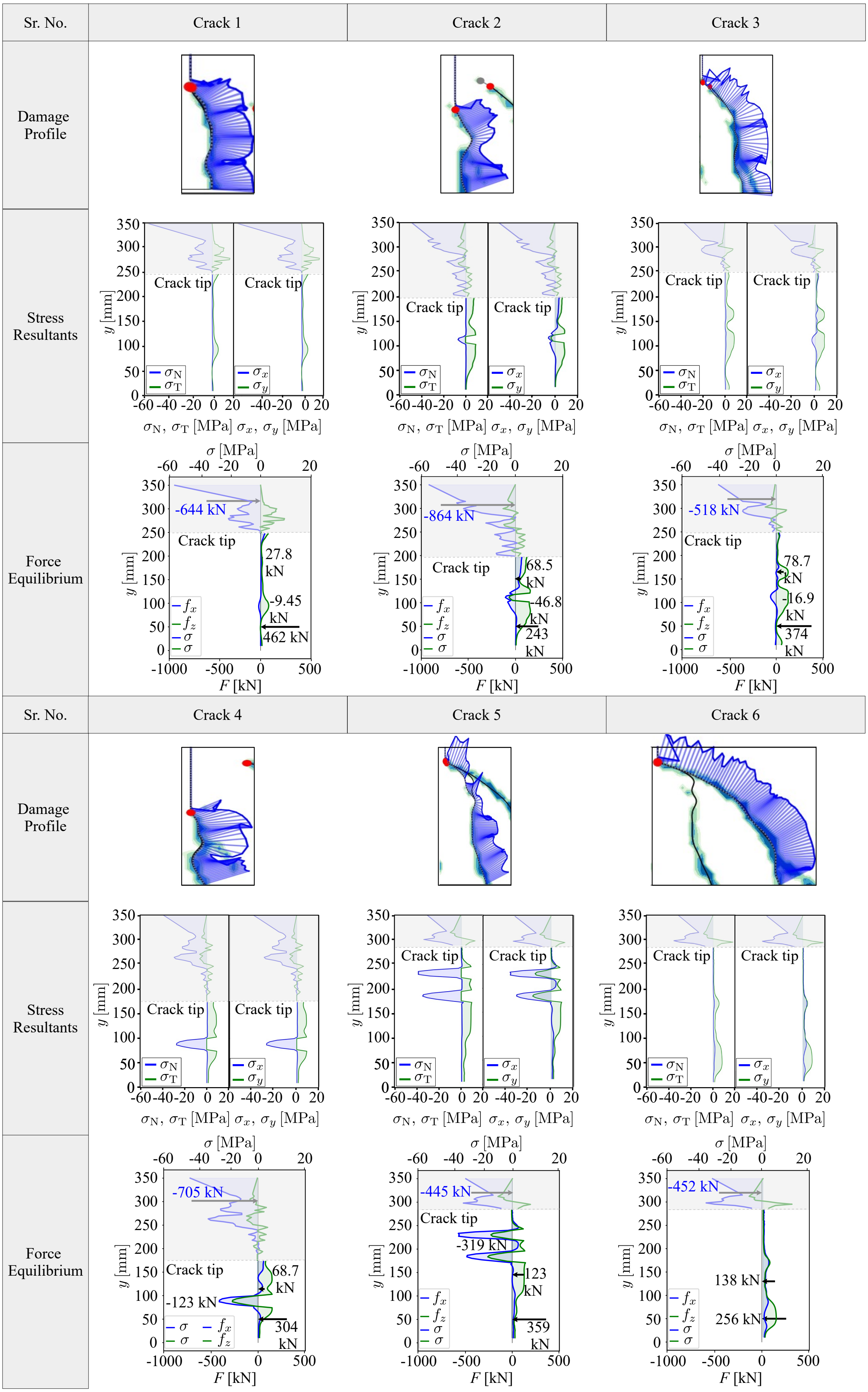

Figure 6.6: Damage profiles, stress resultants and force equilibrium of all the cracks in beam B1

Sr. No.	Crack 1	Crack 2	Crack 3
Moment Time curve	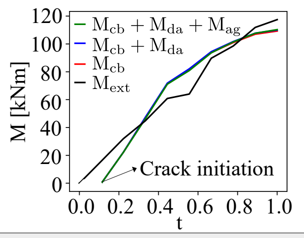	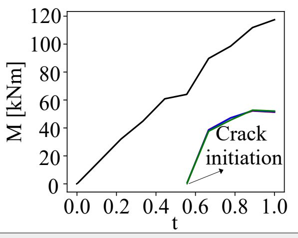	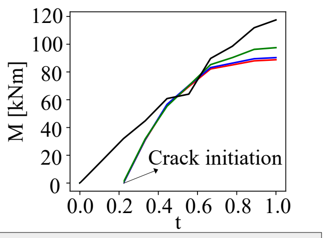
Sr. No.	**Crack 4**	**Crack 5**	**Crack 6**
Moment Time curve	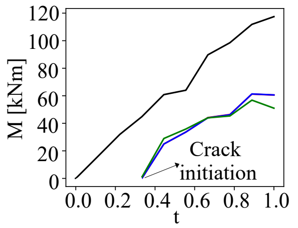	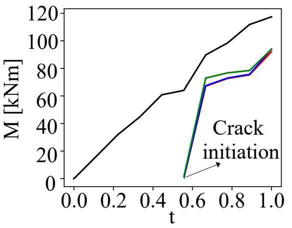	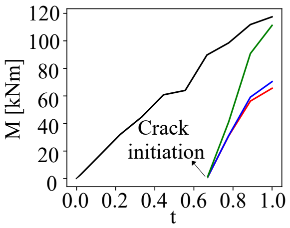

Figure 6.7: External and internal moment comparison for all cracks in beam B1

approximately satisfied. It is worth noting here that the dissatisfaction with the state of equilibrium could be attributable to a number of uncertainties connected to the DIC's inability to capture the strain state in the uncracked zone. Furthermore, this could be owing to the restrictions of the proposed constitutive laws in the literature, which should be evaluated and verified.

The internal and external moment profiles for all the primary cracks obtained from the tool are also plotted in Fig. 6.9. For crack C1, it is being depicted that M_{ext} is higher in comparison to the internal bending moment. Additionally, it is evident from the damage profile (see Fig. 6.8) that crack C1 was initially discovered to be governed by bending, but later on the crack propagation appears to be governed by shear. This is also demonstrated by an internal bending moment obtained by aggregate interlock action, which appears to take the lead in the moment action after 30 kNm in the moment history. While the internal bending moment for crack C2 is somewhat greater than the exterior bending moment, the aggregate interlock action is once more apparent as a result of the crack's inclined propagation close to the ultimate state. Similarly, the internal moment obtained for crack C4 is also higher then M_{ext} and the aggregate interlock contribution is evident for this crack as its governed by shear action. For cracks C5, C6, C7 it can be seen that the internal moment contribution is smaller in comparison to the external moment. Furthermore, the moment contribution due to aggregate interlock action for these cracks is higher due to significant shear action for crack propagation. For crack C8, the aggregate interlock contribution is extremely small and the overall internal moment contribution is too little in contrast to M_{ext}.

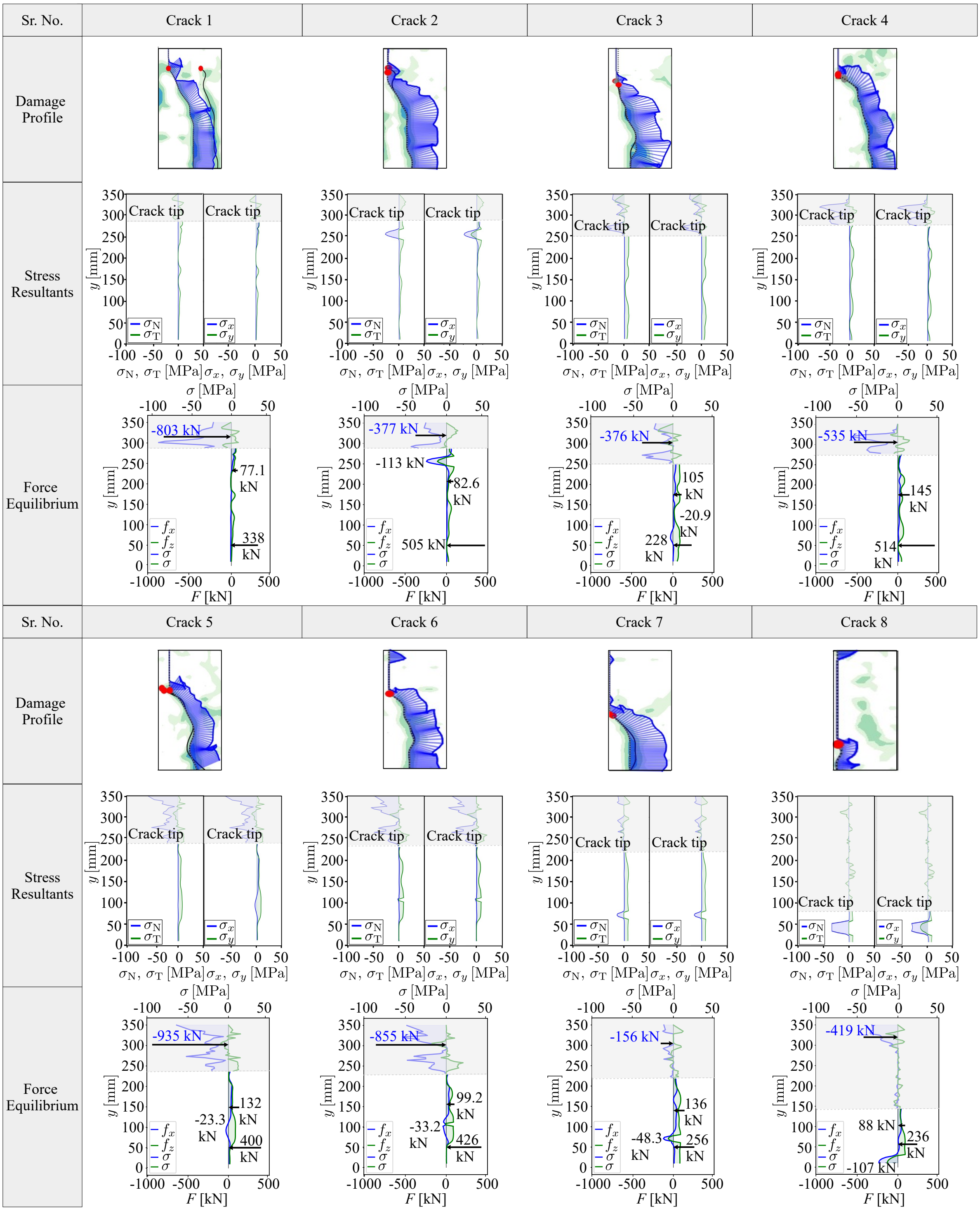

Figure 6.8: Damage profiles, stress resultants and force equilibrium for beam B2

Sr. No.	Crack 1	Crack 2	Crack 3	Crack 4
Moment Time curve	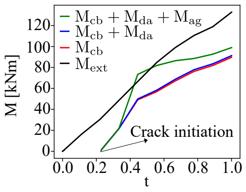	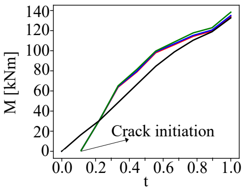	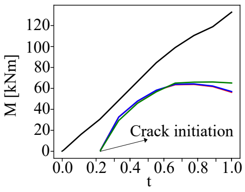	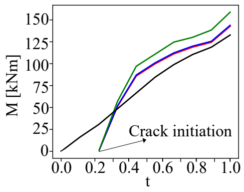
Sr. No.	**Crack 5**	**Crack 6**	**Crack 7**	**Crack 8**
Moment Time curve	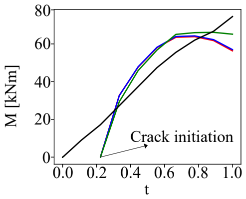	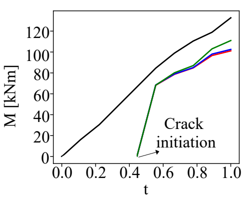	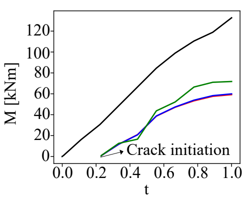	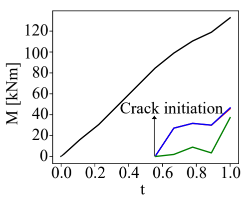

Figure 6.9: Moment-time curves for all cracks in beam B2

6.4 Moment and shear profiles

To visualize the validity of the constitutive laws utilized in the analysis, the overall moment and shear profiles from the crack detection tool are shown and compared to the corresponding exterior moment and shear profiles.

6.4.1 Beam B1

The detected crack patterns, moment profile, and shear contributions for each of the cracks found in beam B1 obtained from the damage based crack detection tool (DCDT) are shown in Fig. 6.10. The DCDT-obtained moment profile demonstrates an erratic pattern, which can be attributed to the limitations introduced by the use of multiple constitutive laws in this research. Therefore, these constitutive laws needs to be verified and refined. Similarly, the shear profile acquired from the crack detection tools shows that the shear profile of crack C1 appears to increase approximately linearly, whereas the shear profiles of cracks C2, C3, C4, C5, and C6 appear to leap fairly abruptly over the loading history. Crack C3 shear profile appears to exhibit a significant increase at $0.3t$ in the loading history. This resultant is almost twice as high in comparison to the actual shear force resultant. Similarly, the shear caused by crack C5 is three times greater than the real contribution. These results raise questions on the validity of the assumed constitutive laws.

6.4.2 Beam B2

A varied trend may also be seen in the moment resultants from beam B2 when compared to its external moment profile (see Fig. 6.10). An approximately linear increase in shear force is seen for crack C2 as the loading history progresses. Yet, this shear force resulting from the beam is twice as large as in comparison to the external shear force obtained from this beam. The shear resultant for crack C1 shows a sudden jump at $0.3t$ (i.e. its almost four times high to the actual shear force) but this resultant than starts to decline as the crack propagates deeper during the loading history. At $0.3t$, the shear resultant increases dramatically for cracks C3 and C4, and it is later determined that for crack C3, the shear resultant is roughly four times higher than the external shear force resultant at the ultimate state. The shear force resultant for crack C6 is the highest, while the shear force resultant for crack C8 is the lowest and less than the beam's external shear force resultant. But crack C8 doesn't propagate much further into the beam and has been found to stop extending earlier. Because of this, the shear force contribution from this crack seems to have a constant profile with small changes.

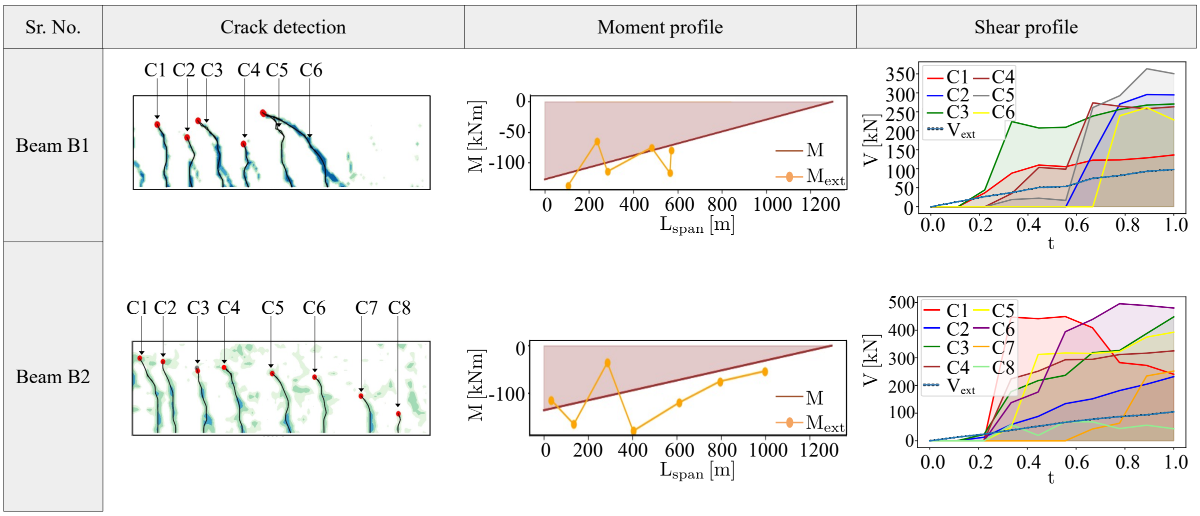

Figure 6.10: Detected crack paths, moment profiles and the shear profiles for both beams B1, B2

6.5 Conclusions

This chapter focuses on advancing and validating analytical models to accurately characterize shear zone behavior in reinforced concrete (RC) elements. Using the Damage-Based Crack Detection Tool (DCDT), the study evaluates stress resultants based on established constitutive laws from the literature.

The chapter discusses the underlying mechanisms governing shear zones and identifies areas for potential improvement. Analysis of moment profiles indicates an overestimation of total stress contributions to bending moments, highlighting the necessity for further refining constitutive laws to achieve equilibrium across various RC beam configurations.

In summary, the framework presented provides a robust tool for refining constitutive assumptions through the analysis of high-resolution kinematic data obtained from multiple RC specimens without shear reinforcement. This automated crack detection scheme represents a significant advancement in concrete mechanics, promising to deepen our understanding of shear zone behavior in RC elements. The findings from this study are poised to refine existing analytical models and enhance the design of RC structures, thereby facilitating more precise and reliable structural assessments.

7 Development of discrete crack model for shear zones

7.1 Introduction

The present thesis also focuses on the development of a discrete crack model to accurately predict the critical shear crack value and its shear capacity for a given initial boundary value problem (IBVP). On the basis of the findings from the crack detection tool, the aim of this development is to propose an analytical model using measured crack kinematics presented in the previous chapters. The reason for pursuing this line of study is because the previously created shear zone models are drawing some worrying criticism from the scientific community. A brief overview on the ongoing debate among the scientific community is discussed here.

7.2 Reservations on the CSCT

Both critical shear crack theory (CSCT) and modified compression field theory (MCFT) assumes that the shear force at the maximum load is controlled by the characteristic crack width w of the dominant crack leading to failure [Fernández Ruiz and Muttoni, 2018]. This assumption is being challenged in [Dönmez and Bažant, 2019] where according to the finite element simulations, the crack width w is highly variable along the crack length. In order to incorporate the size effect, the CSCT assumes that:

$$\frac{v_u}{\sqrt{f_c}} = \frac{\alpha_1}{1+\alpha_2 \frac{w}{d_{dg}}} \tag{7.1}$$

where, $\alpha_1 = 1/3, \alpha_2$ denotes the empirical calibration constant while $d_{dg} = \min(d_{ag} + 16.40)$. Here, d_{ag} is the maximum aggregate size. This assumption seems to defy the basic supposition of the cohesive crack model, according to which crack bridging cohesive stress σ_c decreases due to increasing crack opening w. Whereas in equation 7.1, crack opening w appears linearly in the denominator that agrees neither with the FE simulations nor with the experimental evidence on postpeak softening of cracks in concrete [Dönmez and Bažant, 2019]. Furthermore, in the scientific community it is now generally accepted that cohesive softening curve is approximately bilinear, with a steep initial drop followed by a very long tail [Hoover and Bažant, 2014, Hoover et al., 2013]. In CSCT, the width of the diagonal crack is supposed to be proportional to the reference strain ε, such that:

$$w = \alpha_3 \varepsilon d \tag{7.2}$$

here, $\alpha_3 = 120/\alpha_2$ while ε is the assumed strain. This assumption is deemed a fiction and not possible with reference to the concepts of fracture mechanics [Dönmez and Bažant, 2019]. Moreover, according to CSCT the reference strain ε is assumed to be the longitudinal normal strain acting at distance $d/2$ from the concentrated load $P = V_R$ towards the support and at the depth of $0.6d$ from the top face of the beam. Nonetheless, this assumption has been labeled a mystery, with some questioning the foundation for these suppositions, since the values seem empirical in an attempt to match some of the experimental results. In the case of continuous beams, T, I, or box cross sections, these values would need to be modified due to the fact that these shapes have distinct moment-curvature relations. [Dönmez and Bažant, 2019].

The reference strain ε in CSCT is calculated according to the linear elastic theory based on the Bernoulli-Navier hypothesis of plane cross sections remaining plane, hence:

$$\varepsilon = \frac{M}{bd\rho E_s(d - c/3)} \frac{\alpha_4 d - c}{d - c} \tag{7.3}$$

here, $M = V_R(a - \alpha_5 d)$, $\alpha_4 = 0.6$, $\alpha_5 = 1/2$. Furthermore, in the case of concrete beams with one sided reinforcement,

$$c = \alpha_6 d\, , \alpha_6 = \frac{\rho E_s}{E_c} \left(\sqrt{1 + \frac{2E_c}{\rho E_s}} - 1 \right) \tag{7.4}$$

where, E_c, E_s are the modulus of elasticity of concrete and steel reinforcement respectively, while ρ is the reinforcement ratio and c, a is the distance of the neutral axis from the top face of the beam and shear span respectively. As concrete exhibits nonlinear behavior in its ultimate state, the aforementioned equations have been decried as fiction, raising an alarming question about the reference strain calculation based on linear elasticity [Dönmez and Bažant, 2019]. Other reservations involve the limited applicability of the classical beam bending theory based on the Bernoulli-Navier hypothesis to the flexure of thin beams. In addition, the FE study shows that the originally plane cross section would be very distorted in the final form. For this reason, the formulas to calculate the inelastic behavior are highly complicated. Moreover, it is demonstrated that the total energy release from the structure, rather than the stresses, is the true cause of failure in quasi-brittle materials [Dönmez and Bažant, 2019].

According to the CSCT's final hypothesis, the equations provided are presumptively relevant at the maximum load of the beam since they are based on the linear elastic beam theory. This assumption is questioned with the observation that the suggested size effect equation is used to avoid fracture mechanics and substitute it with simple linear elastic beam analysis [Dönmez and Bažant, 2019]. The authors attempted to address all these reservations regarding CSCT in [Muttoni and Fernández Ruiz, 2019]. In answer to a query about why the crack width varies so much, it is stated that the CSCT takes into consideration the critical shear crack's non-uniform distribution and sliding behavior.

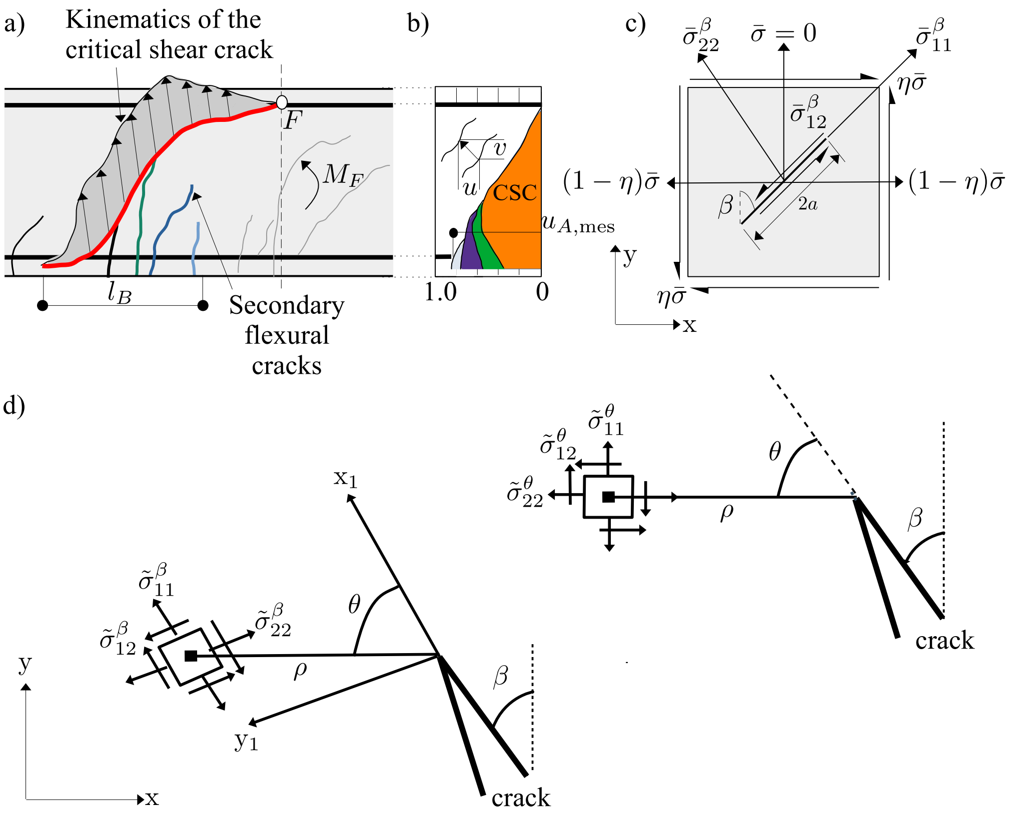

Figure 7.1: (a) Crack geometry and measured relative measured displacements between crack lips [Muttoni and Fernández Ruiz, 2019], (b) horizontal component of the opening of crack, (c) lay out of far field stresses, (d) Maximum principal stress theory

The profiles correlate to the bilinear crack shape as well as the position of the center of rotation, which represents the relative displacements of the two bodies separated by the critical shear crack. It is pertinent to mention that Eq. 7.1 expresses the result of the integration of stresses along the free body defined by the critical shear crack and not the local stress. To address the reservations of equation 7.2, the authors of CSCT have come forward to state that the correlation between the reference value of the opening and of the critical shear crack, the reinforcement and the effective depth of the member is justified by an equation i.e. written as:

$$u_A = \varepsilon_s l_B \tag{7.5}$$

here, l_B is the length where the tributary flexural cracks develop while ε_s represents the reinforcement strain which is being calculated with simple equilibrium conditions and by an assumption of an elastic behavior of the reinforcement (Fig. 7.1) [Muttoni and Fernández Ruiz, 2019]. In addition, the authors of CSCT have commented that the assumptions adopted for the model were verified by the test results (Fig. 7.1(ab)) which were conducted with detailed instrumentation and hence, are not dependent on the numerical results attained by finite element simulation which relies on the consideration of the constitutive laws.

The critique of the reference strain assumption is discussed in great depth in [Muttoni and Fernández Ruiz, 2019]. Regarding the reference strain, it has been made clear that it is appropriate to assume a linear connection between the acting bending moment and the crack opening under the condition that the reinforcement exhibits elastic behavior. The majority of design strategies for shear and bending adopt this hypothesis, which is supported by experimental data (Fig. 7.1) [Muttoni and Fernández Ruiz, 2019]. Moreover, same linear behavior is required for predicting the location of the resultant in the compression zone in order to establish an appropriate value for the lever arm. According to the available data, a critical shear crack opening may be calculated in connection to full information on the variable crack opening and sliding at the crack. In addition, the criticisms of using CSCT for T-shaped beams are also discussed in full detail in [Ribas Gonzalez and Fernández Ruiz, 2017]. In the end, the authors of CSCT conclude that the aim of the CSCT is not to replace fracture mechanics but to provide a mechanical model that is consistent with the test observation and in agreement to the experimental evidence and physical boundary responses [Muttoni and Fernández Ruiz, 2019]. A thorough explanation of the additional concerns on CSCT, as well as the author's remarks to clear up any misunderstandings, may be found elsewhere [Muttoni and Fernandez Ruiz, 2020, Abdullah Dönmez et al., 2020, Dönmez et al., 2020]. Motivated by these talks, we set out to create a discrete crack analytical model and verify its accuracy by comparing its predictions to the measured kinematics and evaluated stress data obtained from the damage based crack detection tool (DCDT).

7.3 Linear elastic fracture mechanics (LEFM) for crack orientation

The crack propagation criteria based on stress resultants at the crack tip is found to be absent in the CSCT. This criterion is a vital component in the development of SCPT [Classen, 2020]. For the sake of the reader's conceptual comprehension, this section provides a quick summary of the techniques of fracture mechanics found in the literature to analyze the direction of crack propagation.

7.3.1 Maximum principal stress theory (MPST)

Over the past two decades, fracture mechanics has been used extensively to study the quasi-brittle behaviour of materials such as concrete, rock and ceramics. Multiple theories exist in the literature to describe quasi-brittle failure under combined effect of tensile and shear loading in fracture mechanics. One of these theories is Maximum Principal Stress Theory (MPST) that can be used for the visualization of shear crack orientation. According to this theory, crack growth will take place for an in-plane mixed mode along the direction for which the initial normal stress across the possible crack path is tensile, principal, and maximum [Bažant and Planas, 2019]. The theory evaluates the stresses in the vicinity of crack tip from the known far field stress state. The external stresses at a point in the finite element and along the crack are shown in Fig. 7.1(c) and represented as:

$$\bar{\sigma}_{ij} = \begin{bmatrix} (1-\eta)\bar{\sigma} & \eta\bar{\sigma} \\ \eta\bar{\sigma} & 0 \end{bmatrix} \tag{7.6}$$

Here, $\bar{\sigma}$ represents the far field stress state whereas η represents a coefficient which acts as a switch whose value range from zero to one to constitute the cases from pure tension to pure shear. The far field stress is depicting the stress state at a point in an element, but transformation is required to convert this stress state along the crack for evaluating the stresses within the propagating crack using the Westergaard stress functions. Hence,

$$R^{\beta}_{kl} = \begin{bmatrix} \cos\beta & -\sin\beta \\ \sin\beta & \cos\beta \end{bmatrix} \tag{7.7}$$

$$\bar{\sigma}^{\beta}_{kl} = R^{\beta}_{ki}\bar{\sigma}_{ij}R^{\beta}_{jl} \tag{7.8}$$

where, R^{β}_{kl} is the transformation matrix along initial crack inclination angle β whereas Eq. 7.8 shows the transformed stress field along the crack. In order to obtain the stress profile at the tip of the crack, Westergaard stress function is used which requires the stress state to be converted into the stress intensity factors i.e. K_I, K_{II} which depicts the mode I, mode II stress intensity factors, respectively. The reason for using stress intensity factors is because they portray the complete severity of the stress state at the crack tip by taking into account the transformed far field stresses and the length of the crack [Irwin, 1957]. So,

$$K_I = \sqrt{\pi a}\,\bar{\sigma}^{\beta}_{11};\, \mathrm{K}_{II} = \sqrt{\pi a}\,\bar{\sigma}^{\beta}_{12} \tag{7.9}$$

Positive sign of stress intensity factors highlights tension while the negative values show compression. A brief overview on stress intensity factors can be found in section 7.3.7.

7.3.1.1 Stress profile at crack tip including T-stress

The stress profile around crack tip as conceptualized by Westergaard stress function [Westergaard, 1997] and simplified by Irwin using Airy stress functions is used in MPST on the basis of an assumption that the material is isotropic. By using complex numbers, Westergaard solved the problem of the stress field in an endless plate with a crack. This equation of complex numbers showing stress at crack tip is written here:

$$\tilde{\sigma}^{\beta}_{ij}(\rho) = \frac{\left[K_I S^{I}_{ij}(\theta) + K_{II} S^{II}_{ij}(\theta)\right]}{\sqrt{2\pi\rho}} + T\delta_{i1}\delta_{j1} \tag{7.10}$$

where $S^{I}_{ij}(\theta)$, $S^{II}_{ij}(\theta)$ are the angular functions obtained from Irwin's approximation and are discussed in detail elsewhere [Bažant and Planas, 2019]. William and Ewing discovered a disparity between MPST results and experiments, with a substantial difference appearing at minor loading angles. T-stress, also known as crack parallel stress, was one of the causes of this disparity [Williams and Ewing, 1972]. Hence, crack parallel stress is added into Eq. 7.10. The crack parallel stress can be evaluated from stress difference method i.e. the difference of stresses acting along the crack [Yang, 1999], hence:

$$T = \bar{\sigma}^{\beta}_{22} - \bar{\sigma}^{\beta}_{11} \tag{7.11}$$

Fig. 7.1(bc) shows the stress field from Westergaard functions to explain the stress state around the crack. To apply the maximum principal stress criterion for crack propagation transformation of the stresses into polar coordinates is required.

$$\tilde{\sigma}^{\theta}_{ij}(\theta,\rho) = R^{\theta}_{ki}\tilde{\sigma}^{\beta}_{ij}R^{\theta}_{jl} \tag{7.12}$$

where,

$$R^{\theta}_{kl} = \begin{bmatrix} \cos\theta & -\sin\theta \\ \sin\theta & \cos\theta \end{bmatrix} \tag{7.13}$$

Now the crack propagation angle can be attained by following the principal condition of MPST which states that the stresses are principal i.e.:

$$\tilde{\sigma}^{\theta}_{12} = 0 \tag{7.14}$$

With this condition, crack propagation angle θ at the tip of the crack can be attained if the global stress states, inclination, and length of the previous crack is already known. With this proposed state of stress at a point in the crack, studies are performed to visualize how the crack will propagate according to Maximum Principal Stress Theory for three cases (i.e. pure tension, mixed mode and pure shear) without the inclusion of T-stresses for simplicity (see Fig. 7.2). The studies show that the propagating crack can be attained simply as:

$$\psi = \theta + \beta \tag{7.15}$$

7.3.2 Westergaard function

Westergaard devised a method to establish the stress profile around the crack. There are two merits to this approach. The cracks are included in the solution, and the results are shown in rectangular coordinates. In his solution this rectangular coordinate is expressed

(a) Pure tension

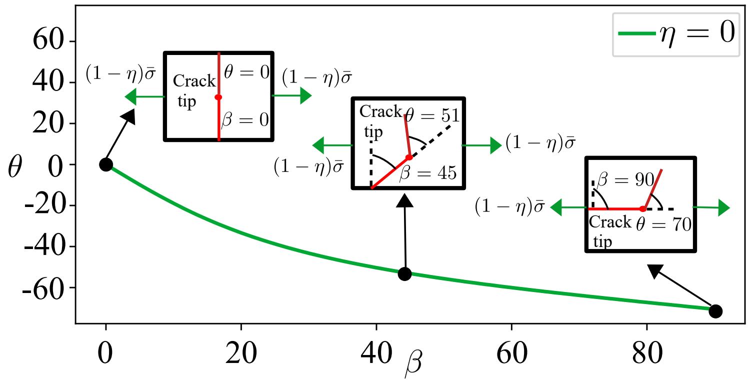

(b) Mixed mode

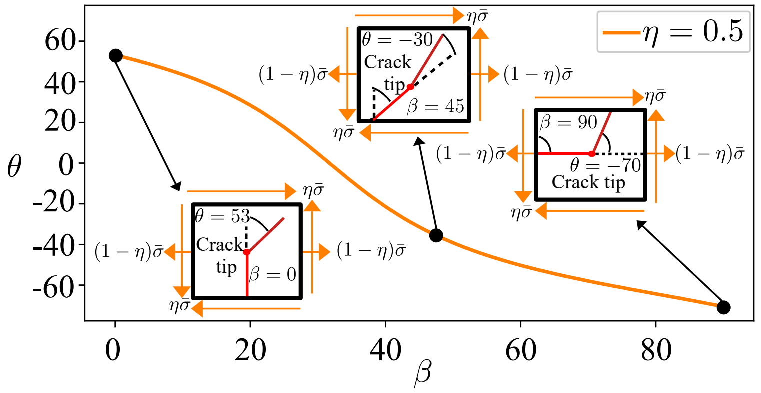

(c) Pure shear

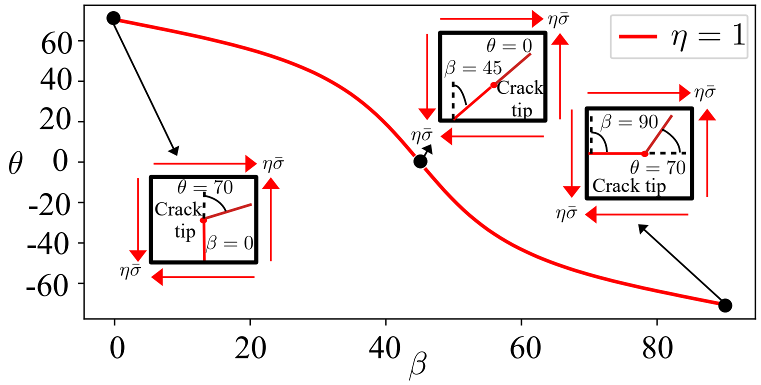

Figure 7.2: (a) Crack propagation for the case of pure tension, (b) crack propagation for the case of mixed mode, (c) crack propagation for the case of pure shear

as complex numbers [Westergaard, 1939], such as:

$$z = x + \imath y \tag{7.16}$$

This feature has certain restrictions. In other words, it may be used to apply equibiaxial tension to an infinite plate rather than uniaxial tension, but it still provides insight into the stress field surrounding cracks.

7.3.3 Airy stress function

This approach is resilient for addressing 2-D equilibrium issues and has been utilized in the past by various researchers to develop analytical solutions to linear elastic problems with fracture. The Airy Stress Function notion begins with Equilibrium, i.e.

$$\Sigma \boldsymbol{F} = m\boldsymbol{a} \tag{7.17}$$

This is applicable if the object is in equilibrium i.e. $\boldsymbol{a} = 0$ and $\Sigma \boldsymbol{F} = 0$. For stress tensor the equilibrium condition will be given as:

$$\nabla \cdot \sigma + \rho f = \rho a \tag{7.18}$$

here, f, a, σ, ρ represents the body forces, acceleration, stress and density respectively. As the body is in equilibrium (i.e. acceleration and body forces are zero), therefore, the equilibrium condition becomes:

$$\nabla \sigma = 0 \tag{7.19}$$

In 2-D the equilibrium condition will be written as:

$$\frac{\partial \sigma_{xx}}{\partial x} + \frac{\partial \tau_{xy}}{\partial y} = 0, \frac{\partial \sigma_{yy}}{\partial y} + \frac{\partial \tau_{xy}}{\partial x} = 0 \tag{7.20}$$

This is based on the assumption that the 2-dimensional stress components are connected to the Airy scalar stress function ϕ:

$$\sigma_{xx} = \frac{\partial^2 \phi}{\partial y^2}; \sigma_{yy} = \frac{\partial^2 \phi}{\partial x^2}; \tau_{yy} = -\frac{\partial^2 \phi}{\partial x \partial y} \tag{7.21}$$

Hence, by substituting (7.21) into (7.20) we get:

$$\frac{\partial}{\partial x}\left(\frac{\partial^2 \phi}{\partial y^2}\right) - \frac{\partial}{\partial y}\left(\frac{\partial^2 \phi}{\partial x \partial y}\right) = 0, \frac{\partial}{\partial y}\left(\frac{\partial^2 \phi}{\partial x^2}\right) - \frac{\partial}{\partial y}\left(\frac{\partial^2 \phi}{\partial x \partial y}\right) = 0 \tag{7.22}$$

where (7.22) shows that equilibrium is satisfied irrespective of the choice of ϕ. Here, the only limitation of choosing ϕ is that the solution is restricted to isotropic materials and that strains are related to stress via Hooke's law. Hence, ϕ must satisfy the biharmonic

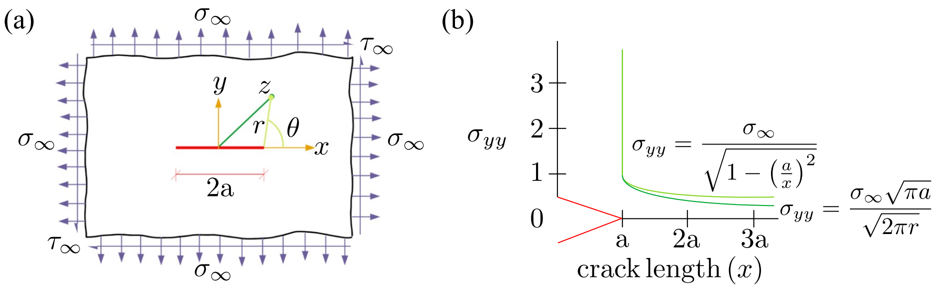

Figure 7.3: (a) Center cracked infinite panel subjected to remote equiaxial tension, (b) stress at the crack tip

equation which reads as:

$$\frac{\partial^4\phi}{\partial x^4} + 2\frac{\partial^4\phi}{\partial x^4 \partial y^4} + \frac{\partial^4\phi}{\partial y^4} = 0 \tag{7.23}$$

Therefore, any ϕ function satisfying the above condition i.e. $\nabla^4\phi = 0$ is guaranteed to produce stress and strain fields that are in equilibrium for an isotropic solid not subjected to body forces.

7.3.4 Complex numbers and Westergaard solution

As shown in figure 7.3a and as stated above, for a crack subjected to tension, Westergaard chose an Airy Stress function consisting of complex numbers i.e. $z = x + \imath y$. Hence, the stress becomes a function of x and y which can be written as $\sigma = f(x,y)$. As we know, stress is the second derivative of the Airy Stress function, and in order to grasp Westergaard's solution, we must first examine the Cauchy-Riemann Equations, which describe the connection between many various kinds of derivatives of complex functions and are expressed as:

$$Re\frac{dZ}{dz} = \frac{\partial ReZ}{\partial x} = \frac{\partial ImZ}{\partial y} \tag{7.24}$$

$$Im\frac{dZ}{dz} = \frac{\partial ImZ}{\partial x} = -\frac{\partial ReZ}{\partial y} \tag{7.25}$$

Any complex function and its derivative can be separated to complex and imaginary parts. So,

$$Z = ReZ + \imath ImZ \tag{7.26}$$

and its derivative:

$$\frac{dZ}{dz} = Re\frac{dZ}{dz} + \imath Im\frac{dZ}{dz} \tag{7.27}$$

Now, from the Cauchy-Riemann condition, the derivative can also be written as:

$$\frac{dZ}{dz} = Re\frac{dZ}{dz} + \imath Im\frac{dZ}{dz} = \frac{\partial ReZ}{\partial x} + \imath\frac{\partial ImZ}{\partial x} = \frac{\partial ImZ}{\partial y} - \imath\frac{\partial ReZ}{\partial y} \tag{7.28}$$

7.3.4.1 Westergaard solution

Westergaard identified an Airy function of complex numbers as the stress field's solution on an infinite plate with a crack. The choice of Airy stress function by Westergaard was:

$$\phi = Re\bar{\bar{Z}} + yIm\bar{Z} \tag{7.29}$$

Here, the integral of Z is represented by $\bar{Z}$ and the integral of $\bar{Z}$ by $\bar{\bar{Z}}$, where Z reads as:

$$Z(z) = \frac{\sigma_\infty}{\sqrt{1-\left(\frac{a}{z}\right)^2}} \tag{7.30}$$

a depicts crack length. The differential equation must also be satisfied here, irrespective of the choice of the function given in Eq. (7.29). The function for $Z(z)$ depicted in (7.30) proved to be solution of a crack in an infinite plate. Now, the derivatives of ϕ will be taken to find out the stresses at the tip of crack. Hence, we get:

$$\sigma_{xx} = \frac{\partial^2\phi}{\partial y^2} = ReZ - yImZ', \sigma_{yy} = \frac{\partial^2\phi}{\partial x^2} = ReZ + yImZ', \sigma_{xy} = -\frac{\partial^2\phi}{\partial x \partial y} = -yReZ' \tag{7.31}$$

7.3.5 Irwin's crack tip solution

Irwin showed that the Westergaard's result can be simplified in the area around the crack by expressing z as a complex variable:

$$z = a + re^{\imath\theta} \tag{7.32}$$

The main point in this equation is that $r = 0$ at the crack tip and $r << a$ in the region around the crack. Irwin utilized this inequality to calculate the polar coordinate values of the stress components around the crack tip. Therefore, substituting (7.32) into (7.30) and assuming that $a^2 >> ar >> r^2$ we get:

$$Z(z) = \frac{\sigma_\infty}{\sqrt{\frac{2are^{\imath\theta}}{a^2}}} \tag{7.33}$$

which can also be written as:

$$Z(z) = \sigma_\infty \sqrt{\frac{a}{2r}} e^{-\imath\frac{\theta}{2}} \tag{7.34}$$

Taking into account Euler's famous identity i.e. $e^{\imath\theta} = \cos\phi + \imath\sin\phi$, we obtain:

$$Z(z) = \sigma_\infty \sqrt{\frac{a}{2r}} \left(\cos\frac{\theta}{2} - \imath\sin\frac{\theta}{2}\right) \tag{7.35}$$

The same process will be repeated for Z' and the resultant will be:

$$Z'(z) = -\frac{\sigma_\infty}{2r}\sqrt{\frac{a}{2r}}\left(\cos\frac{3\theta}{2} - \imath\sin\frac{3\theta}{2}\right) \tag{7.36}$$

Now, with respect to the stress equation given in (7.31), we can conclude the stress components at the crack tip as:

$$\begin{aligned}\sigma_{xx} &= \frac{\partial^2\phi}{\partial y^2} = ReZ - yImZ' \\ &= \sigma_\infty\sqrt{\frac{a}{2r}}\cos\frac{\theta}{2} - y\frac{\sigma_\infty}{2r}\sqrt{\frac{a}{2r}}\sin\frac{3\theta}{2}\end{aligned} \tag{7.37}$$

By replacing $y = r\sin\theta$:

$$\sigma_{xx} = \sigma_\infty\sqrt{\frac{a}{2r}}\left(\cos\frac{\theta}{2} - \frac{1}{2}\sin\theta\sin\frac{3\theta}{2}\right) \tag{7.38}$$

and $\frac{1}{2}\sin\theta = \sin\frac{\theta}{2}\cos\frac{\theta}{2}$. Therefore,

$$\sigma_{xx} = \sigma_\infty\sqrt{\frac{a}{2r}}\left(\cos\frac{\theta}{2} - \sin\frac{\theta}{2}\cos\frac{\theta}{2}\sin\frac{3\theta}{2}\right) \tag{7.39}$$

Finally we get:

$$\sigma_{xx} = \sigma_\infty\sqrt{\frac{a}{2r}}\cos\frac{\theta}{2}\left(1 - \sin\frac{\theta}{2}\sin\frac{3\theta}{2}\right) \tag{7.40}$$

At the end, simply multiplying and dividing by π, i.e. $\sqrt{\frac{\pi}{\pi}}$. So, all three forms of stresses reads as:

$$\sigma_{xx} = \sigma_\infty\sqrt{\frac{\pi a}{2\pi r}}\cos\frac{\theta}{2}\left(1 - \sin\frac{\theta}{2}\sin\frac{3\theta}{2}\right) \tag{7.41}$$

$$\sigma_{yy} = \sigma_\infty\sqrt{\frac{\pi a}{2\pi r}}\cos\frac{\theta}{2}\left(1 + \sin\frac{\theta}{2}\sin\frac{3\theta}{2}\right) \tag{7.42}$$

$$\sigma_{xy} = \sigma_\infty\sqrt{\frac{\pi a}{2\pi r}}\cos\frac{\theta}{2}\sin\frac{\theta}{2}\cos\frac{3\theta}{2} \tag{7.43}$$

Here, $\sigma_\infty\sqrt{\pi a}$ depict K_I i.e the stress intensity factor for mode I cracking. Similarly, a function involving the stress intensity factor for mode II cracking (K_{II}) can also be obtained. A brief overview on stress intensity factors can be found in Sec. 7.3.7.

7.3.6 Reason for selecting Irwin approach for stress resultants

The reason for selection of Irwin's formulation of complex variables over Westergaard function can be visualized in Fig. 7.3b. The plot depicts that we get a better approximation of the stresses with Irwin's formulation which appears to be more accurate. Furthermore, the use of accurate approximation at the tip of crack is important as it governs (1) how fast the crack grows, (2) which direction it grows and (3) and how it propagates. Another reason for the selection of this approach is that the definition of the stress intensity factors, which describes the complete severity of the stress state at the crack tip involving σ_∞ and a. The stress equations obtained by Irwin also includes $\sqrt{r}$ in the denominator that depicts the dependence of stress on the distance from crack tip and reflects the singularity at $r = 0$.

7.3.7 Stress intensity factors

The stress intensity factor describes the state of stress at the crack tip. It is proportional to the rate of crack propagation and is used to create fracture failure criteria [Irwin, 1957]. The definition of stress intensity factor K, according to Irwin's estimate, is a near crack tip approximation to Westergaard's complete solution for the stress field around a crack.

Here, it is pertinent to mention that the numerator of all three equations (7.41), (7.42), and (7.43) contains the expression $\sigma_\infty\sqrt{\pi a}$. The combination of σ_∞ and a describes the complete severity of the crack tip. This was first recognized by Irwin who named the term "Stress intensity factors (SIF)" that reads as:

$$K = \sigma_\infty\sqrt{\pi a} \tag{7.44}$$

7.3.8 Applicability of LEFM on concrete

In the early days of research into concrete fracture, linear elastic fracture mechanics (LEFM) was used as a technique to analyze the findings of laboratory experiments. It was later discovered that these results obtained from LEFM didn't correspond with the experimental data. The presence of a tiny zone that results from gradual softening is the primary factor identified as the cause of this aberration in the fracture behavior of concrete and other quasi-brittle materials. This nonlinear zone, for which stress decreases at increasing deformation is termed as fracture process zone (FPZ) [Bažant and Planas, 2019]. FPZ is surrounded by non softening nonlinear zone (i.e. hardening plasticity or perfect plasticity). As a result of void formation, microcracking, interface breakages, frictional slips, and other causes of material softening in the case of quasi-brittle materials, the majority of the nonlinear zone suffers progressive damage, and the zone of plastic hardening for such materials is frequently negligible. In quasi-brittle materials, the size of FPZ cannot be excluded and has to be taken into consideration for calculations. A typical representation of nonlinear zone in a quasi-brittle material is shown in

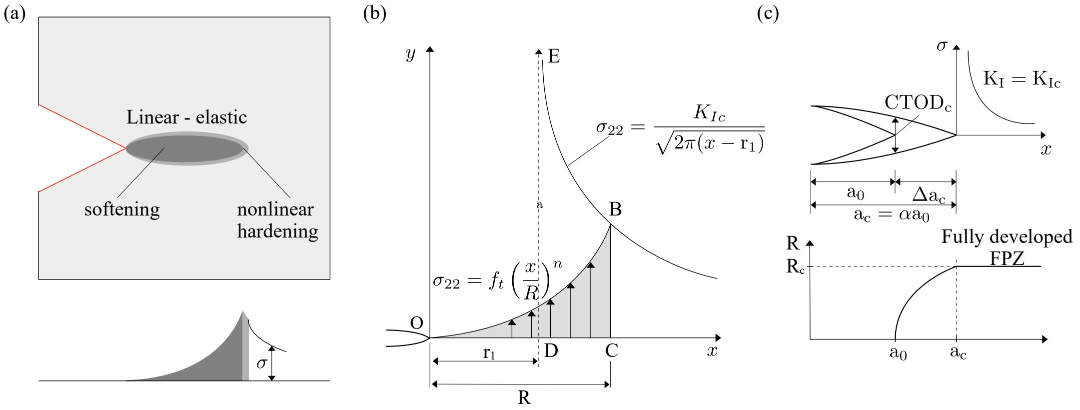

Figure 7.4: (a,b) Fracture process zone in a quasi-brittle material, (c) fracture resistance curve (R-curve)

Fig 7.4ab. On the basis of this, the length of the yielding zone from Irwin formulation is written as:

$$l_{\text{fpz}} = \frac{1}{\pi}\left(\frac{K_I}{\sigma_y}\right)^2 \tag{7.45}$$

Now to decide if LEFM can be used to describe this particular case, we assume that crack growth take place when $K_I = K_{Ic}$, hence:

$$l_{\text{fpz(c)}} = \frac{1}{\pi}\left(\frac{K_{Ic}}{\sigma_y}\right)^2 \tag{7.46}$$

However, for the LEFM to be applicable, $l_{\text{fpz(c)}}$ must be small in comparison to the structural dimensions. Equation (7.46) can be used for a quasi-brittle material by replacing σ_y with f_t but that does not work as then the $l_{\text{fpz(c)}}$ value is much less then the actual one. The difference is caused by the fact that after reaching its tensile strength, concrete softens and microcracks rather than yielding.

Fig. 7.4b shows the progressive softening for a quasi-brittle material in fracture process zone is concave upwards. But to sum up, the size of FPZ (i.e. $l_{\text{fpz(c)}}$) is obtained as:

$$l_{\text{fpz(c)}} = \eta\left(\frac{K_{Ic}}{f_t}\right)^2 = \frac{EG_f}{f_t^2} \tag{7.47}$$

where, η is a dimensionless constant taking the value $1/\pi$ for Irwin's estimate and having higher values ranging from 2 to 5 for concrete. The fraction on the right side of Eq. (7.47) is termed as characteristic length l_{ch}. Therefore, the final result reads:

$$l_{\text{fpz(c)}} = \eta ł_{\text{ch}} \tag{7.48}$$

Using the stated values of concrete's characteristic length, which vary from 0.15 m to

0.40 m, one may deduce that the size of the fully formed fracture process zone will be in the range of 0.3 m to 2.0 m. These approximations prevent LEFM from being used for assessing the behavior of laboratory specimens. Therefore, for the case of fracture of quasi-brittle materials where the fracture process zone is not negligible, we can use simplified, partly linearized models for simulation of the response of the specimen far from the crack tip by an equivalent elastic crack. The only problem then is figuring out how to define this equivalence to figure out where the crack's tip is at a certain load level. Therefore,:

$$\Delta \mathrm{a_c} = \mathrm{a_c} - \mathrm{a_0} \tag{7.49}$$

where $\mathrm{a_c}$ is the equivalent crack and $\mathrm{a_0}$ is the initial crack. In general, this can be done by stating a crack growth rule that relates the effective crack extension $\Delta \mathrm{a_c}$ to the crack driving force R. This method is called the R-curve Approach (see Fig. 7.4c) [Bažant and Planas, 2019](see Sec. 7.3.8.1).

7.3.8.1 R-curve

An envelope of energy release rate is referred to as an R-curve [Chengsheng et al., 1990]. At critical point c, the rate of energy release can be expanded as a Taylor Series Expansion such that:

$$G = G_\mathrm{c} + \sum_{n=1}^{\infty} \frac{1}{n!} \left(\frac{d^n G}{d\mathrm{a}^n} \right)_c (\mathrm{a} - \mathrm{a_c})^n \tag{7.50}$$

where, G_c is the value of G at critical point. Using $G = 0$ at $a = 0$:

$$G_\mathrm{c} = -\sum_{n=1}^{\infty} \frac{1}{n!} \left(\frac{d^n G}{d\mathrm{a}^n} \right)_c (-\mathrm{a_c})^n \tag{7.51}$$

here, the critical crack length $\mathrm{a_c}$ is assumed to be proportional to the initial crack length $\mathrm{a_0}$ for a material with pre-critical stable crack propagation. Therefore,

$$\mathrm{a_c} = \Delta \mathrm{a_c} - \mathrm{a_0} = -\alpha \mathrm{a_0} \tag{7.52}$$

where, α is a parameter describing the pre-critical stable crack growth $(\alpha \geq 1)$. For an accurate solution, the following two requirements must be met during the propagation of the critical crack, according to the definition of R-curve [Ouyang and Shah, 1991]:

$$G_\mathrm{c} = R_\mathrm{c} \tag{7.53}$$

$$\left(\frac{\partial G}{\partial \mathrm{a}} \right)_\mathrm{c} = \left(\frac{\partial R}{\partial \mathrm{a}} \right)_\mathrm{c} \tag{7.54}$$

R-curve is a two parameter model where K_{Ic} (Critical Stress Intensity factor) and $\mathrm{CTOD_c}$ (critical Crack Tip Opening Displacement) are needed to be known to obtain this fracture resistance curve. The formulation of R-curves is based on an equivalent elastic crack approach for traction-free cracks. Substituting Eq. (7.52) in (7.51) and noting that $d\mathrm{a} = d(\mathrm{a}_0 + \Delta\mathrm{a}) = d\Delta\mathrm{a}$, yields:

$$G_\mathrm{c} = -\sum_{n=1}^{\infty} \frac{1}{n!} \left(\frac{d^n G}{d\mathrm{a}^n}\right)_\mathrm{c} \left(\frac{\alpha}{\alpha-1}\right)^n (-\Delta\mathrm{a_c})^n \tag{7.55}$$

The aforementioned equation provides a differential equation with variable coefficients that controls the critical energy release rate for fracture in a material and is valid for any critical point. A linear differential equation with constant coefficients may be derived from this equation as follows:

$$\sum_{n=1}^{\infty} d(d-1)(d-2)....(d-n+1)\left(\frac{\alpha}{\alpha-1}\right)^n (-1)^n + 1 = 0 \tag{7.56}$$

After simplification Eq. (7.55) can be written as:

$$G_\mathrm{c} = \sum_{n=1}^{\infty} \beta_n (\Delta\mathrm{a}_n)_n^d \tag{7.57}$$

Now, according to the conditions stated above in (7.53) and (7.54), we get.

$$R_c = \sum_{n=1}^{\infty} \beta_n (\Delta a_c)_n^d \tag{7.58}$$

where, $R_\mathrm{c}, \Delta\mathrm{a_c}$ are replaced by R and Δa. Fracture resistance R is calculated as follows when the energy release rate is used as an approximation to the quadratic expression of crack length (i.e., when $n = 2$):

$$R = \beta_1 (\mathrm{a} - \mathrm{a}_0)^{d_1} + \beta_2 (\mathrm{a} - \mathrm{a}_0)^{d_2} \tag{7.59}$$

By using the boundary condition i.e. $\left(\frac{\partial R}{\partial \mathrm{a}}\right)_{\mathrm{a_c}=\mathrm{a}_0} = 0$, a relationship between β_1 and β_2 can be obtained. As a result, the simplified equation to determine fracture resistance owing to a crack's changing length is as follows:

$$R = \beta_2 \psi (\mathrm{a} - \mathrm{a}_0)^{d_2} \tag{7.60}$$

where,

$$\psi = 1 - \left(\frac{d_2 - (\alpha-1)/\alpha}{d_1 - (\alpha-1)/\alpha}\right)\left(\frac{\alpha\mathrm{a}_0 - \mathrm{a}_0}{\mathrm{a} - \mathrm{a}_0}\right)^{d_2 - d_1} \tag{7.61}$$

and,

$$d_{1,2} = \frac{1}{2} + \frac{\alpha - 1}{\alpha} \pm \left(\frac{1}{4} + \frac{\alpha - 1}{\alpha} - \left(\frac{\alpha - 1}{\alpha} \right)^2 \right)^{\frac{1}{2}} \tag{7.62}$$

R-curves preserve the concept of an equivalent elastic crack while allowing for thorough mechanical analysis, which includes characterizing the whole crack formation process and calculating load-displacement curves. A crack growth rule is used in this approach to relate the various crack growth resistances to crack development [Ouyang and Shah, 1991]. So,

$$R = R(\Delta \mathrm{a}) \tag{7.63}$$

Initially, it was considered that $R(\Delta \mathrm{a})$ may approximately be a fixed material property but later it was added that R-curve depends on the structure size and also on the shape of the specimen or structure. Now, in order to calculate the pre-critical stable crack growth α, Sneddon's solution for the near field displacement of an equilibrium crack is used [Sneddon, 1946]. According to this solution, Crack Mouth Opening Displacement for $\sigma = Ps/b^2$ for a three point bending beam can be obtained as:

$$\mathrm{CMOD} = \frac{4\sigma f_2}{E} = \frac{4Psf_2}{b^2 E} \tag{7.64}$$

where, P = load on the beam, $s =$ span, $b =$ depth of the beam and f_2 is the geometry factor for the crack mouth opening displacement whose value is equal to 1.42 for three point bend beam. Furthermore, the Crack Opening Displacement with respect to Sneddon's solution is written as:

$$\mathrm{COD} = \mathrm{CMOD}\sqrt{a^2 - x^2} = \frac{4Psf_2}{b^2 E}\sqrt{a^2 - x^2} \tag{7.65}$$

This method developed by Sneddon provides a precise solution for an infinitely large specimen with a central notch, but only an approximation for other geometries. Now, in order to obtain α and β, the critical condition i.e. $K_I = K_{I\mathrm{c}}$ and $\mathrm{CTOD_c} = \mathrm{COD}$ is used which occur at $x = \mathrm{a}_0$ and $l_{fpz(\mathrm{c})} = \alpha \mathrm{a}_0$. Therefore,

$$\mathrm{CTOD_c} = \frac{4Psf_2}{b^2 E}\sqrt{(\alpha \mathrm{a}_0)^2 - (\mathrm{a}_0)^2} \tag{7.66}$$

$$\alpha = \frac{\pi E^2 f_1^2 \mathrm{CTOD_c^2}}{32\mathrm{a}_0 K_{I\mathrm{c}}^2 f_2^2} + \sqrt{\frac{\pi E^2 f_1^2 \mathrm{CTOD_c^2}}{32\mathrm{a}_0 K_{I\mathrm{c}}^2 f_2^2} + 1} \tag{7.67}$$

Replacing $\mathrm{CTOD_c}$ from 7.66 in 7.67, we get:

$$\alpha = \frac{\pi f_1^2 P^2 s^2 (\alpha^2 {\mathrm{a}_0}^2 - {\mathrm{a}_0}^2)}{2\mathrm{a}_0 K_{I\mathrm{c}}^2 b^4} + \sqrt{\frac{\pi f_1^2 P^2 s^2 (\alpha^2 {\mathrm{a}_0}^2 - {\mathrm{a}_0}^2)}{2\mathrm{a}_0 K_{I\mathrm{c}}^2 b^4} + 1} \tag{7.68}$$

Here, E represents the Young's modulus of concrete and f_1 is the geometry parameter for the stress intensity factor whose value is 1.123 for the three point bending beam. Similarly, in order to find β for the critical state, we can assume the condition that R is equal to $R_{Ic} = (K_{Ic})^2/E$. Hence:

$$R_{Ic} = \beta_2 \psi (\alpha \mathrm{a}_0 - \mathrm{a}_0)^{d_2} = \frac{{K_{Ic}}^2}{E} \tag{7.69}$$

So, β becomes:

$$\beta_2 = \frac{{K_{Ic}}^2 (\alpha \mathrm{a}_0 - \mathrm{a}_0)^{-d_2}}{E \psi} \tag{7.70}$$

Replacing the value of ψ from equation 7.61 and by inputting $\mathrm{a} = \alpha \mathrm{a}_0$, yields:

$$\beta_2 = \frac{K_{Ic}^2 (\alpha \mathrm{a}_0 - \mathrm{a}_0)^{-d_2}}{E \left(1 - \frac{d_2 - \frac{\alpha - 1}{\alpha}}{d_1 - \frac{\alpha - 1}{\alpha}}\right)} \tag{7.71}$$

For clarity, Fig. 7.4c illustrates the whole region after the crack tip in the quasi-brittle material, as well as its fracture resistance curve. The value of R should not exceed $R_{Ic} = (K_{Ic})^2/E$ for $\mathrm{a} > \mathrm{a}_c$. The geometry factors are taken into consideration in this technique through f_1 and f_2, which may be acquired via LEFM.

7.4 Cantilever action

7.4.1 Kani's tooth model

With increased stress, a reinforced concrete beam transforms into a comb-like structure. Flexural fractures in the tensile zone creates more or less concrete teeth, while the compressive zone is the backbone of the concrete comb (see Fig. 7.5a). The comb's teeth are represented by the concrete teeth that are physically separated from one another by flexural cracks. On the basis of the analysis of such structural system, two different mechanisms are possible, such as [Kani, 1964]:

1. As long as the capacity of the concrete teeth is not exceeded, the beam-like behavior prevails.
2. When the resistance of the concrete teeth has been removed, a tied arch with quite different qualities remains.

The behavior of narrow beams exposed to progressively rising loads is widely understood in the scientific world. As the load is increased, the first cracks occur far before the allowable load is achieved. These cracks appear as thin cracks, and their presence is inconsequential as long as the tensile strain is less than 0.1 percent. Due to the bond between the two materials, the strain on the steel and concrete in this instance is equal. When the load is increased, the width and length of the crack expand, resulting in a reduction in the area of the compression zone. This impact becomes very obvious as the tension in steel approaches and exceeds the yield point stress. The stress in the compressive zone rises quickly as the bending process continues. This increase is caused by a reduction in the area of the compressive zone caused by cracks, and to a lesser amount by increased load. The internal mechanism of such a beam is shown in Fig. 7.5a.

7.4.1.1 Mechanism of diagonal failure

Diagonal failure occurs as a result when the central section of the test beam under pure loading is stronger than the end sections. In the case of a reinforced concrete beam with bond, the tensile force T is added to the concrete body as a distributed load along reinforcing bars (see Fig. 7.5b).

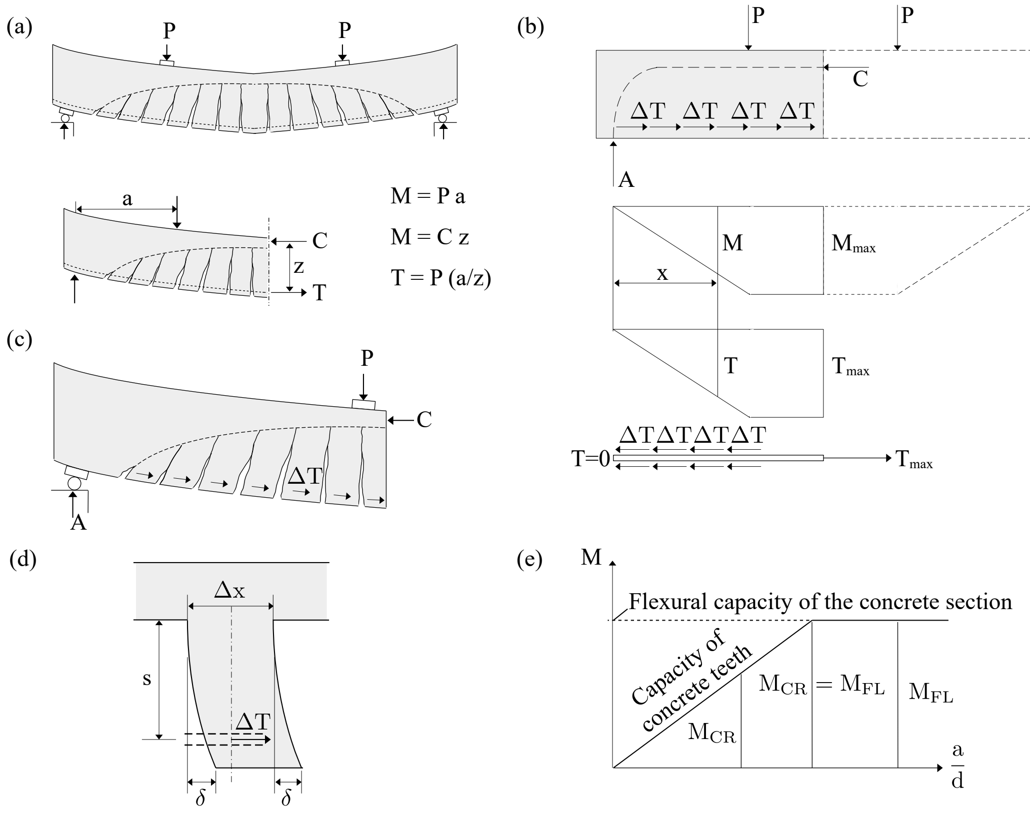

Figure 7.5: (a) Mechanism of flexural failure, (b) internal forces of reinforced concrete beam with bond, (c) function of concrete teeth, (d) deformed concrete tooth, (e) capacity of concrete tooth

In case of a fully effective bond, the force T is uniformly distributed along the reinforcing bars, where the shear force V is constant. This is indicated by ΔT forces in the Fig. 7.5b. The thrust line, which is defined as the direction of the resulting force, is no longer a straight line. The reaction A is combined with a small ΔT so that the resultant starts steeply upwards. More ΔT forces join the free body with increasing distance of the cross section from section A so that the thrust line bends up to the right. The shape of the thrust line depends on the distribution of the ΔT forces. Considering equilibrium of the part of the beam we see that the tensile force is:

$$\mathrm{T} = \frac{\mathrm{M_x}}{\mathrm{z}} \tag{7.72}$$

where, z is the lever arm. As long as the comb like structure functions as a beam, the force T is more or less proportional to the bending moment $\mathrm{M_x}$. As a result, the force T is greatest in the center of the beam and diminishes to zero towards the supports. The force T changes along the reinforcing bar. Equilibrium is only attainable in this instance if such ΔT forces exist solely on the surface of the bar. The bond forces between reinforcement and concrete, or ΔT forces, are internal forces that manifest twice: once acting on the bars and once acting in the opposite direction on the concrete body. Now taking the concrete as a free body (see Fig. 7.5c) and replacing the actions of the bars by corresponding internal forces, the acting ΔT forces will be directed towards mid span while these ΔT forces on the reinforcement will be directed towards the end of the bar. Here Fig. 7.5c illustrates the mechanism of comb like structure i.e. the concrete teeth are separated by flexural cracks and loaded by horizontal ΔT forces. The function of every concrete tooth in the span can be compared to that of a short vertical cantilever anchored in the compressive zone of the beam and possessing a horizontal force ΔT. As long as the concrete teeth carries the ΔT forces, the comb like structure is a actually a beam with a distinctive compressive zone with the highest compressive strain acting at the top fiber. This comb like structure cannot be in equilibrium without the existence of these ΔT forces.The research concludes that the beam theory assumption that the plane cross section stays planar is incorrect since it leads to an inconsistent shear strength theory.

Concrete teeth being short cantilevers loaded by horizontal ΔT forces are subjected to bending. An originally straight axis of a concrete tooth will become curved due to the bending action of the ΔT forces (see Fig. 7.5d). Assuming the axis of the concrete tooth to remain straight will correspond to the condition of no bending i.e $\Delta \mathrm{T} = 0$. Now, in order to determine the resistance of the concrete tooth, lets assume the Fig. 7.5d. By employing the relation of the beam theory, the maximum tensile stress in a concrete tooth due to a force ΔT is given by:

$$\sigma = \frac{\mathrm{M}}{\mathrm{Z}} = \frac{\mathrm{M}}{\mathrm{S}} = \frac{\Delta \mathrm{Ts}}{\mathrm{b}(\Delta \mathrm{x})^2/6} \tag{7.73}$$

The maximum resistance ΔT of the concrete tooth is reached when the stress σ reaches the tensile strength f_t of the concrete. Thus the resistance of the concrete teeth per unit length of the beam can be expressed as:

$$\frac{\Delta \mathrm{T}}{\Delta \mathrm{x}} = \frac{f_t}{6}\frac{\Delta \mathrm{x}}{\mathrm{s}}\mathrm{b} \tag{7.74}$$

When the resistance is met, the concrete teeth break off under increased strain. If T represents the full tensile force of the reinforcement in the central section of the beam, which reduces due to bond action gradually to zero towards the support then the average bond between concrete and reinforcement will be given by T/a. When this bond load which actually constitutes the horizontal load of the concrete teeth reaches the resistance of the concrete teeth then:

$$\frac{T}{a} = \frac{\Delta \mathrm{T}}{\Delta \mathrm{x}} = \frac{f_t}{6}\frac{\Delta \mathrm{x}}{\mathrm{s}}\mathrm{b} \tag{7.75}$$

Now, the maximum bending moment existing in the central section of the beam can be expressed by:

$$\mathrm{M_{CR}} = \frac{7}{8}d\mathrm{T} \tag{7.76}$$

or by using the expression for T, such that:

$$\mathrm{M_{CR}} = \frac{7}{8}\frac{f_t}{6}\frac{\Delta \mathrm{x}}{\mathrm{s}}\mathrm{bad} \tag{7.77}$$

Now, let us designate the part of this moment which depends only on the properties of the cross section width, hence:

$$M_0 = \frac{7}{8}\frac{f_t}{6}\mathrm{bd}^2 \tag{7.78}$$

Thus, the critical bending moment at which the concrete teeth break away can be expressed as:

$$\mathrm{M_{CR}} = M_0\frac{\Delta \mathrm{x}}{\mathrm{s}}\frac{\mathrm{a}}{\mathrm{d}} \tag{7.79}$$

It is being recognized that this critical moment appears to be a linear function of the shear arm ratio a/d. This means that a linear relationship will be obtained between the moment and the shear arm ratio if the cross-section, concrete and the reinforcement are kept constant for a series of beams with only varying a/d (see Fig. 7.5e).

The value of $\mathrm{M_{CR}}$ increases with increasing a/d until at some point the full flexural capacity of the cross section is reached. As, this is the greatest moment that the cross section can carry, therefore, the load-carrying capacity of the beam remains constant from this point on-wards.

7.4.1.2 Limitation of Kani's tooth model

According to Kani's tooth model, a local bending failure of concrete teeth is thought to produce the global shear failure. The model predicts that the concrete teeth would crack when the vertical stresses reach a critical value due to the bending moment at the clamping of the cantilever. This model also assumes that bending cracks grow vertically from the tension side of the member up to the neutral axis, ignoring any shear transfer activities in the crack. It is also being assumed here that the critical stress is equivalent to the tensile strength of concrete. These presumptions lead to the conclusion that the model significantly underestimates the shear strength of RC members [Classen, 2020].

7.4.2 Cantilever action adoption in SCPT

SCPT proposes a more refined technique to account for cantilever action while encompassing all shear transfer actions. In this approach, the considered shear transfer actions are assumed to be identical on the left and right hand side of a concrete tooth i.e. n and $n+1$ (see Fig. 7.6a). SCPT considers cantilever length and geometry to be variable and growing throughout the shear crack propagation process. Lever arms of all shear transfer movements are supposed to increase here appropriately. In SCPT, the variation of the tensile force ΔF_s existing between the crack n and $n+1$ is calculated by:

$$\Delta F_\mathrm{s} = \frac{F_{\mathrm{s(n+1)}}}{n} < (s_\mathrm{cr} - s_\mathrm{cr,delamination}) \pi d_\mathrm{s} n_\mathrm{s} 1.26 \sqrt{\frac{f_\mathrm{c}}{20}} \tag{7.80}$$

and

$$n = \frac{\lambda_\mathrm{cs} d}{s_\mathrm{cr}} \tag{7.81}$$

A complete description of the SCPT can be found in [Classen, 2020]. The upper bound limit of ΔF_s applies, when bond stress reach the bond strength along entire intact bond length where reinforcement is not delaminated. In the end, the vertical stress at the crack tip can be calculated by:

$$\sigma_{\mathrm{z},0} = \frac{M_\mathrm{CA}}{b_w s_\mathrm{cr}^2/6} \tag{7.82}$$

The clamping moment $\mathrm{M_{CA}}$ allows to determine the compressive stresses at the opposite of the concrete tooth, which is a pre-requisite to capture strutting action.

7.5 Evaluation of the shear capacity

The evaluation of the shear capacity yields an idea into the location of the critical crack as predicted by some of the analytical models in the literature. A brief overview of some of these approaches is presented here.

7.5.1 CSCT method

The evaluation of the shear capacity is an iterative process in CSCT. A brief overview of the procedure is presented here whereas the complete detail can be read in [Cavagnis

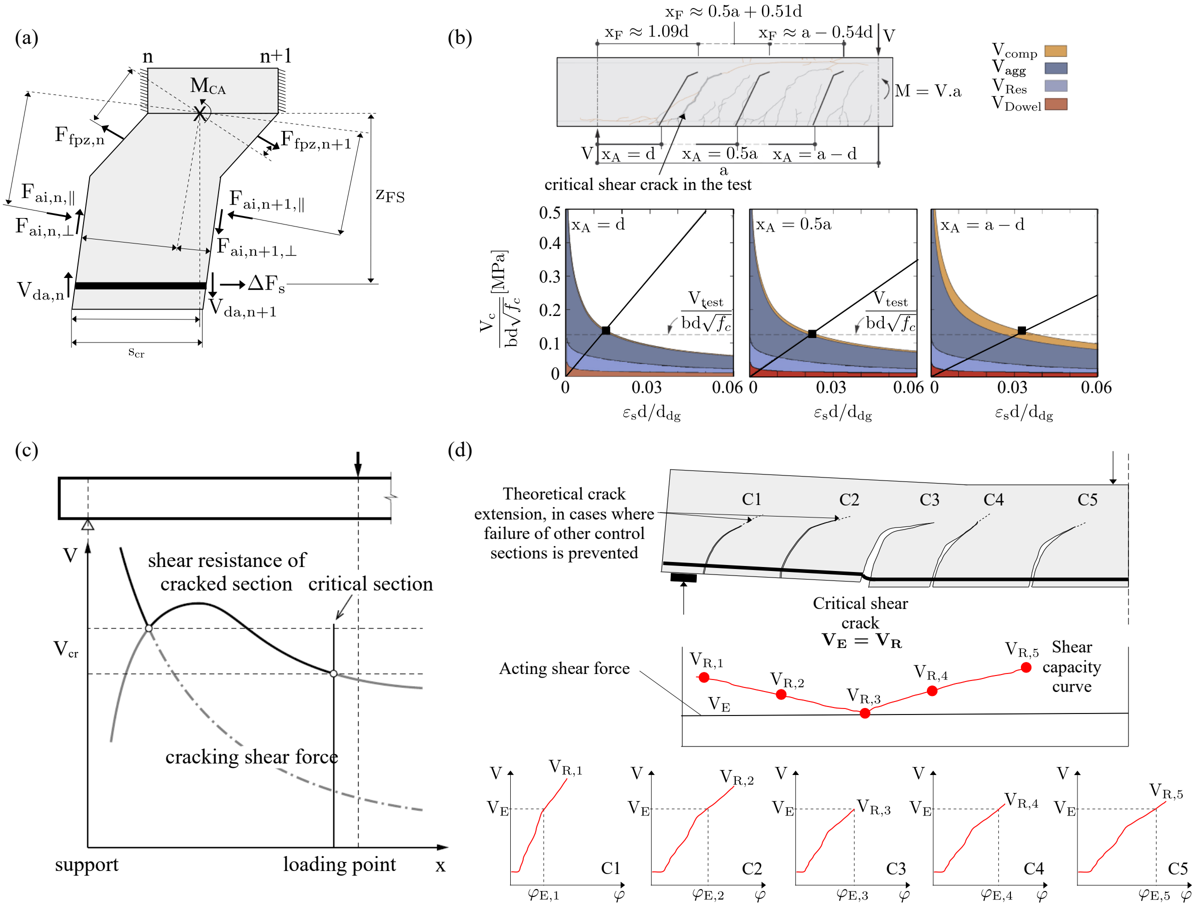

Figure 7.6: (a) Cantilever action (SCPT) [Classen, 2020], (b,c,d) Evaluation of shear capacity [Cavagnis et al., 2018b, Yang, 2014, Classen, 2020]

et al., 2018b]. In the beginning the location of the critical shear crack is selected and an initial horizontal opening of the crack ligament is assumed. Afterwards, the contributions of various shear transfer actions and the corresponding shear strength as the sum of shear carried by various shear transfer actions is calculated. In the next step the crack opening is calculated as a function of the acting bending moment at the section corresponding to the tip of the crack. Now, this attained crack opening is used as an input and the iteration is run again until the assumed and the attained crack openings become equal. Once this is achieved, the shear force defined in the load displacement relationship is compared with the shear capacity obtained from the experiment. Failure occurs when the shear force obtained by the load displacement relationship is equal to the shear capacity defined by the failure criterion. This iterative procedure can be applied for any possible location of the critical crack and it allows determining the shear capacity, deformation capacity, role of various shear transfer actions and theoretical governing location of the critical crack. A look into the shear crack capacity obtained for three cracks that propagated in SC61 is shown in Fig. 7.6b. The complete background of the model can be studied in [Cavagnis et al., 2018b].

7.5.2 Yang approach

Here, a brief discussion of another approach to evaluate the shear capacity is presented [Yang, 2014]. In this method, it is being implied that the cracks initiating at the sections near to the support can carry less shear force in comparison to the ones further away when the M/Vd is very small. A constant critical shear displacement Δ_{cr} is assumed, so that the required shear force needed to make $\Delta = \Delta_{\mathrm{cr}}$ for a crack originated at x_0 from the support can be indicated as the shear resistance of the section (as shown by a solid line in Fig. 7.7c). This observation is in contradiction to the experimental results where the shear resistance of the cracked sections closer to the support become lower. A simple explanation for this is that in spite the shear capacity of an inclined crack is smaller for cross sections located closer to the support, the shear force is still carried by the whole uncracked region as long as the crack does not develop. This results in a much higher shear resistance in comparison to the cracked section. In this approach, the section located at x_0 from the support requires the shear force $V_{\mathrm{cr,m}}$ to generate a crack. Hence,

$$V_{\mathrm{cr,m}} = \frac{M_{\mathrm{cr}}}{x_0} \tag{7.83}$$

$V_{\mathrm{cr,m}}$ is plotted as the cracking shear force line against the location of the cross section in Fig. 7.6c and M_{cr} depicts the cracking moment. The shear resistance is indicated by the part of the shear resistance line between the loading point and the cracking shear force line. After the intersection, the cracking shear force line replaces the other line and acts as a shear resistance line. The location of the lowest point of this curves decides the position of the critical crack.

7.5.3 SCPT method

The criteria to evaluate the critical crack via SCPT is shortly explained here to elaborate the difference in all three presented approaches. The evaluated shear force and the corresponding rotations are plotted for each crack and compared with the acting shear force of the tested beam obtained from the experiment. The crack with the lowest evaluated shear force is considered to be the critical crack (see Fig. 7.6d). The procedure allows to determine the rotations of the cracks throughout the entire loading process up to the state of shear failure that can be used to calculate the overall shear deformations and deflections of the member (see [Classen, 2020]).

7.6 Discrete crack propagation model (DCPM)

The recently developed discrete crack model is explained here for the conceptual understanding of the reader regarding the working principle of the model.

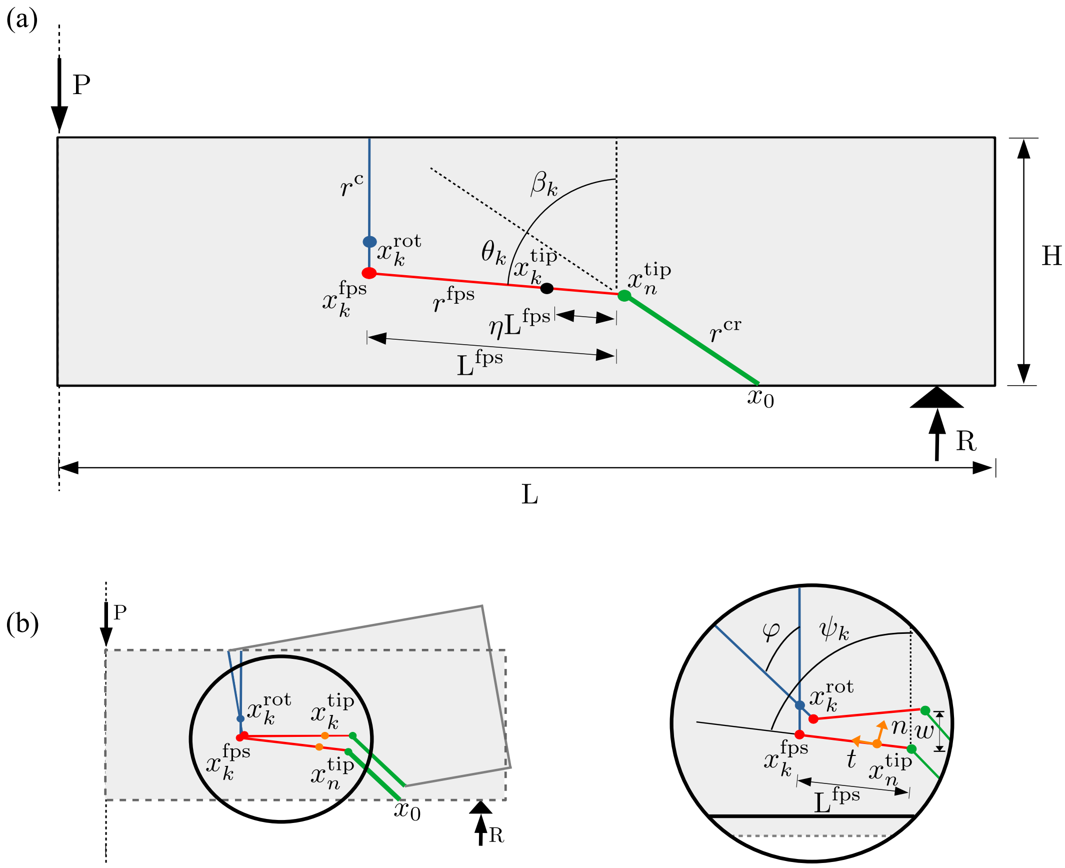

Figure 7.7: a) Crack kinematics, b) zoom in crack tip rotation kinematics

7.6.1 Shear zone kinematics

The novel kinematic approach calculates the geometry of the discrete shear crack and the entire loading process. The model takes the initial crack position as an input parameter and simulates the complete crack geometry as small increments. A simplified three segment crack path is highlighted in Fig. 7.7a to demonstrate the overall step by step incremental procedure. The first segment represents a crack whereas the second part exhibits the fracture process zone represented by a continuous curve i.e. spline or piece-wise linear geometry. The length of the fracture process zone is L^{fps} with an orientation ψ_k with respect to the vertical direction z. The upper part represents the uncracked zone x^{U}. The coordinates of the process zone segment x_{ak}^{fps} given in 7.84 is implicitly considered to be in the state of peak tensile stress with $a \in (0,1)$ denoting the dimension index, k depicting the incremental index and n is the index of the nodal coordinate. So, the position of the tip of the fracture process zone can be expressed by:

$$x_{ak}^{\text{fps}} = x_{an}^{\text{tip}} + L^{\text{fps}} t_{ak} \tag{7.84}$$

where, t_{ak} is the line vector of the fracture propagation segment and depends on the crack orientation angle ψ. x_{an}^{tip} depicts the tip of the pre-existing crack. The kinematics of the section assume that the right side of the shear zone rotates relatively to the fixed left side around an unknown center of rotation x_{ak}^{rot}. The horizontal position of the center of rotation is considered to be aligned to the horizontal position of the tip of the fracture process zone segment (i.e. x_{0k}^{fps}). Therefore:

$$x_{ak}^{\mathrm{rot}} = \begin{bmatrix} x_{0k}^{\mathrm{fps}} \\ x_{1k}^{\mathrm{rot}} \end{bmatrix} \tag{7.85}$$

where, x_{1k}^{rot} represents the vertical position of the center of rotation which is initially taken as $\frac{\mathrm{H}}{2}$ and later derived from the model based on the global equilibrium conditions.

7.6.1.1 Crack extension criterion

Another important aspect of the crack propagation model is the crack extension criterion. It is assumed that the opening w at the tip of the crack is equivalent to the critical width w_{cr} which is written as:

$$w_{\mathrm{cr}} = \frac{f_{\mathrm{t}}}{E_{\mathrm{c}}} L_{\mathrm{c}} \tag{7.86}$$

where, $f_{\mathrm{t}}, E_{\mathrm{c}}, L_{\mathrm{c}}$ represent the tensile strength of concrete, modulus of elasticity of concrete and the characteristic length, respectively. It must be kept in mind that the model takes the initial crack position i.e. x_{ak}^{tip}, L^{fps} as an input parameter which keeps updating the position of the fracture process zone segment (x_{ak}^{fps}) and the previous crack tip. By explicitly relating the tensile concrete strength to a local kinematic variable w_{cr} it is possible to find a closed form solution for the rotation angle ψ corresponding to the prescribed crack extension. With this kinematically described state, the local strain and crack opening profiles along the shear zone ligament become available and can be used as input into the constitutive laws of components acting within the cross section. These constitutive laws are already explained in Chapter 4 of the thesis.

7.6.1.2 Crack tip and its rotated position

After rotation, the final position must be in the line parallel to the vector t_{ak} at the distance w as shown in Fig. 7.7 (b) and calculated as:

$$x_{ak}^{\mathrm{tip},\varphi} = x_{ak}^{\mathrm{tip}} + w_{cr} n_{ak} + \xi\, t_{ak} \tag{7.87}$$

here, $x_{ak}^{\mathrm{tip},\varphi}$ shows the new rotated position of the tip of the crack and n_{ak}, ξ represents a vector normal to the fracture propagation segment depending on the crack orientation angle ψ and slip of the crack segment respectively, whereas x_{ak}^{tip} is depicting the position of iterated current crack tip propagating into the fracture process zone which is written as:

$$x_{ak}^{\text{tip}} = x_{an}^{\text{tip}} + \ell t_{ak} \tag{7.88}$$

where, ℓ is the incremental extension of the crack propagation segment.

7.6.1.3 Slip parameter

The unknown slip ξ is obtained using equal distance by defining two length vectors:

$$p_a = x_{ak}^{\text{tip}} - x_{ak}^{\text{rot}} \tag{7.89}$$

$$q_a^{\xi} = x_{ak}^{\text{tip},\varphi} - x_{ak}^{\text{rot}} \tag{7.90}$$

here, x_{ak}^{rot} refers to the rotation vector (Fig. 7.7 (b)) with an assumption that the horizontal position of the center of rotation is identical to the tip of the segment i.e. $x_{0k}^{\text{rot}} = x_{0k}^{\text{fps}}$ as already discussed before, whereas p_a, q_a^{ξ} are the vectors connecting the rotation center with the current crack tip on the fixed and rotated plate, respectively. So from equal distance, the unknown slip ξ will be evaluated equating Eq.(7.89), Eq.(7.90) as:

$$\|p_a\| = \|q_a^{\xi}\| \tag{7.91}$$

7.6.1.4 Rotation operator

The deformation is assumed to happen within the shear zone only around the center of rotation x_{ak}^{rot}. The rotated position of a point x_{La}^{1} on the ligament L where L denotes line segment can be obtained by taking into account transformation and reads as:

$$x_{\text{L}a}^{1} = T_{ab}(x_{\text{L}a}^{0} - x_{ak}^{\text{rot}}) + x_{ak}^{\text{rot}} \tag{7.92}$$

here $x_{\text{L}a}^{0}$ represents the node on the line of the ligament running through the cross section with L segments whose initial position is pre-existing crack position and it keeps getting updated during the loading history. This crack segment is considered fixed on the left hand side and the rotation operator finds the position of the rotated crack (Fig. 7.7).

7.6.2 Crack path

The crack path defined by a level set function is written as:

$$\gamma(x_a) = 0 \tag{7.93}$$

here x_a represent crack positions. In order to explain the incremental crack path, three branches of the crack are considered including the existing crack which can be denoted as $\gamma_0(x_a) = 0$ ending at the point x_a^{tip} (Fig. 7.7). The crack path is defined along the nodes x_{Ia} where $a \in (0,1)$ representing the dimension index, $\mathrm{I} \in 1 \ldots \mathrm{n_I}$ defining the global node index and $\mathrm{n_I}$ depicting the number of nodes. Furthermore, topological mapping is introduced to specify the association between crack segment number $\mathrm{L} \in 1 \ldots \mathrm{n_I} - 1$ as an index map $\mathrm{I_{Li}}$ where i represents the local node index. Similarly, the uncracked zone will be represented as x_{Ja} where J is a global node index. To simulate the crack path based on finite element procedure, line vector is obtained by subtracting the position of the first node $\mathrm{i} = 0$ from the second node $\mathrm{i} = 1$ as:

$$v_{\mathrm{L}a} = x_{\mathrm{L}1a} - x_{\mathrm{L}0a} \tag{7.94}$$

Normalizing the vector to the unit length:

$$\hat{n}_{\mathrm{L}a} = \frac{v_{\mathrm{L}a}}{\|v\|_{\mathrm{L}}} \tag{7.95}$$

In order to obtain the normal vector to the crack line, Levi-Civita symbol ε_{abc} and an out-of-plane vector $z_a = [0,0,1]$ is assumed. Therefore:

$$\hat{t}_{\mathrm{L}a} = \hat{n}_{\mathrm{L}a} z_c \varepsilon_{abc} \tag{7.96}$$

Now, the transformation matrix for simulating the crack path is written as:

$$\hat{T}_{b\mathrm{L}a} = [\hat{t}_{\mathrm{L}a}, \hat{n}_{\mathrm{L}a}]$$

where, b is the local dimension index. During the simulation, the crack tip keeps getting updated as the crack propagates, changing the position vector x_n^{tip}.

7.6.3 Deformed state

To visualize the deformed state, a rotated configuration of the right plate is considered around the center of rotation x_{ak}^{rot} by the angle φ inducing the critical crack opening w_{cr} at the point x_{ak}^{tip}. Hence, the displacement at the ligament will be:

$$u_{\mathrm{L}a} = x_{\mathrm{L}a}^{1} - x_{\mathrm{L}a}^{0} \tag{7.97}$$

By substituting $x_{\mathrm{L}a}^{1}$ from Eq. (7.92), we obtain the displaced configuration of any point on the right plate. Based on the obtained deformations from Eq (7.97), opening and sliding displacements along the nodes of the ligament are attained from transformation. Hence,

$$w_{\mathrm{L}r} = T_{\mathrm{L}br} u_{\mathrm{L}b} \tag{7.98}$$

where r represents the local coordinate. The opening and sliding displacements are used as an input parameter in constitutive laws incorporating different interacting effects. Hence, the constitutive relation for stresses reads as:

$$s_{\mathrm{L}s} = \mathcal{S}_{\mathrm{L}s}(w_{\mathrm{L}r}) \tag{7.99}$$

here s represents the stresses in the local coordinate and by transformation to the global coordinate system, we get the stress as:

$$\sigma_{La} = T_{Las} s_{Ls} \tag{7.100}$$

7.6.4 Global equilibrium and forces

As the stress profiles are already calculated, one can obtain the force distributions. The two unknowns i.e. center of rotation and crack orientation angle will result in two global equilibrium equations. Therefore:

$$M(\psi, x_{ak}^{\mathrm{rot}}) + Q(\psi, x_{ak}^{\mathrm{rot}})\mathrm{L} = 0 \tag{7.101}$$

$$N(\psi, x_{ak}^{\mathrm{rot}}) = 0 \tag{7.102}$$

The normal forces can be attained simply by integration of horizontal stress distribution:

$$N = \int_0^{\mathrm{H}} \sigma_0(x_1)\,\mathrm{d}x \tag{7.103}$$

here, H represents the height of the beam and σ_0, x_1 are the horizontal component of the stress and vertical coordinate of crack position respectively. The global moment around center of rotation will be obtained from the stress profile and will be written as:

$$M = \int \sigma_0 \left(x_1 - x_1^{\mathrm{rot}}\right)\,\mathrm{d}x_1 + \int \sigma_1 \left(x_0 - x_0^{\mathrm{rot}}\right)\mathrm{d}x_0 \tag{7.104}$$

where, σ_0, σ_1 are the stresses in both directions along the height of the section incorporating all the interacting effects (i.e. dowel action, aggregate interlock, crack bridge action etc.). Now, shear force can be obtained from the global bending moment based on the mathematical fact that the slope of the moment is equivalent to the shear force. Hence, shear force Q reads as:

$$Q(x) = \frac{\mathrm{d}M(x)}{\mathrm{d}x} \tag{7.105}$$

and for a point load in the middle section:

$$Q_M = \frac{M}{L - x_0^{\mathrm{rot}}} \tag{7.106}$$

where, L and M represents the length of the beam and moment obtained from equilibrium.

7.6.4.1 Shear stress at crack tip

The shear stress contribution in continuous concrete is acquired by realizing that the integral of the shear stresses over the cross section must be equal to the global shear force V. Furthermore, based on an assumption that the normal stress distribution along the longitudinal axis of members under concentrated loads is linear so parabolic shape function is used to describe the shear stress state at crack tip. Hence,

$$\tau_z = \mathrm{a}z^2 + \mathrm{b}z + \mathrm{c} \tag{7.107}$$

where, a,b,c can be equated from the boundary condition i.e. zero stress at the top fiber of the compression zone whereas maximum shear distribution acting at the center of rotation (see Fig. 7.8cd). Based on the global boundary conditions the obtained shear stress profile becomes:

$$\tau_z = \mathrm{b}z - \frac{\mathrm{b}z^2}{H} \tag{7.108}$$

The shear force is the integration of the shear stresses over the height of the uncracked

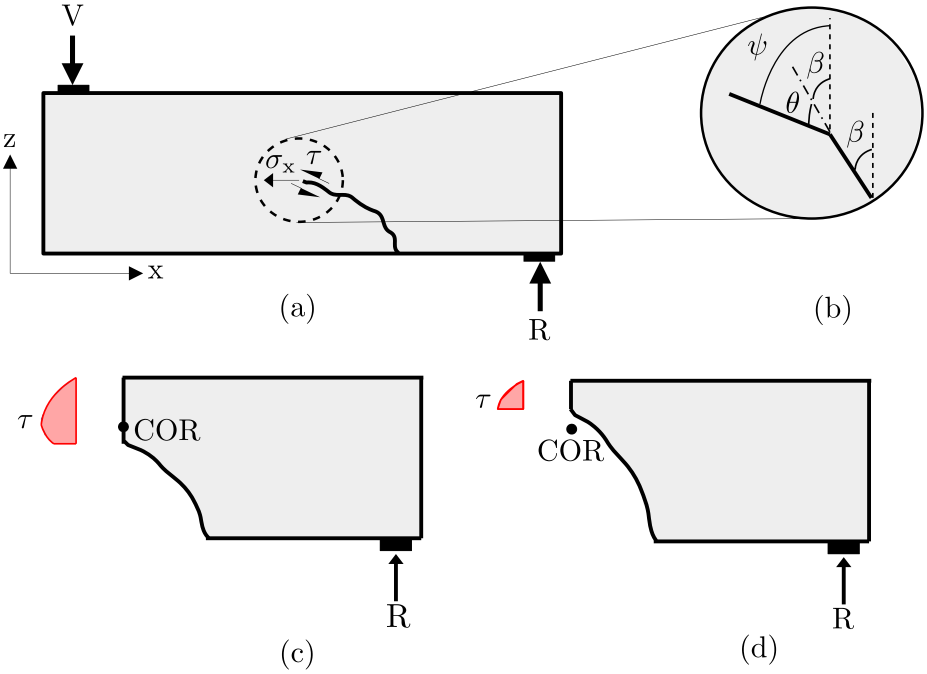

Figure 7.8: (a) Crack tip stresses (b) crack orientation criterion (c), (d) shear stress in uncracked zone

region along the section width B. Therefore, it can be written as:

$$Q = B\int_{z_{\text{fps}}}^{H}\left(\text{b}z - \frac{\text{b}z^2}{H}\right)\text{d}z \tag{7.109}$$

where b value will be evaluated by simply rearranging equation 7.109. So, coefficient b will be replaced into equation 7.108 to attain a function for calculating shear stress at the propagating crack tip.

$$\tau_z = \frac{6HQz}{B(H^3 - 3Hz_{\text{fps}}^2 + 2z_{\text{fps}}^3)} - \frac{6Qz^2}{B(H^3 - 3Hz_{\text{fps}}^2 + 2z_{\text{fps}}^3)} \tag{7.110}$$

where, *B* is the width of the section, *Q* is obtained from the global moment equilibrium condition (already discussed) and *H* is the height of the assumed beam.

7.7 Crack orientation criterion

Another important aspect of the discrete crack propagation criterion is its ability to incorporate crack orientation criterion.

7.7.1 Approach 1

The state of stresses at the tip of the crack are extremely important for the evaluation of the angle of orientation of the next segment in the propagating shear crack. With the condition of the global and local stress state already known, the orientation of the next iteration of the propagating crack can be obtained numerically. A simple approach of principal stress directions is used here to evaluate the orientation of the shear crack.

$$\bar{\sigma}_{ij} = PDP^{-1} \tag{7.111}$$

where, *P*, *D* represents principal stresses and eigen values respectively. By using this direct approach, angle of crack propagation can be simulated efficiently based on the already known stress state at the tip of the crack (Fig. 7.8(a)). Therefore:

$$\bar{\sigma}_{ij} = \begin{bmatrix} \sigma_x & \tau_\text{z} \\ \tau_\text{z} & 0 \end{bmatrix} = \begin{bmatrix} f_t & \tau_\text{z} \\ \tau_\text{z} & 0 \end{bmatrix} \tag{7.112}$$

here, σ_x is the normal stress that is governed by the tensile strength of concrete whereas shear stress τ is obtained from the parabolic shape function (Sec. 7.6.4.1). Based on the known state of stress at the crack tip, orientation of a shear crack is evaluated. Hence, the angle of crack propagation can be obtained simply from principal stresses as (Fig.

7.8(b)):

$$\psi = \tan^{-1}\left[\frac{\sigma_0}{\sigma_1}\right] \tag{7.113}$$

7.7.2 Approach 2

In another approach to evaluate the crack orientation, the direction cosine can be obtained of the vectors:

$$\cos\psi = \frac{p_a q_a^{\xi}}{\|p\|\|q_a^{\xi}\|} \tag{7.114}$$

$$\sin\psi = \sqrt{1-\cos^2\psi} \tag{7.115}$$

Now, after transformation of direction cosines of the vectors p_a and q_a^{ξ}:

$$T_{ab} = \begin{bmatrix} \cos\psi & -\sin\psi \\ \sin\psi & \cos\psi \end{bmatrix} \tag{7.116}$$

7.8 Cross-sectional equilibrium

To find the instantaneous center of rotation and a crack propagation direction for a prescribed extension of a crack, the cross-sectional equilibrium condition is constructed by evaluating all the relevant stress components as indicated in Fig. 7.9. Both horizontal and vertical stress components are considered, including the contributions from uncracked concrete section, reinforcement bridging and dowel action, concrete softening in the fracture process zone and, aggregate interlock between edges of the localized crack. The constitutive laws applied for the individual contributions are already discussed in Chapter 4.

7.9 Cantilever action in DCPM

As a result of increase in loading on a reinforced concrete beam, cracks are formed that transforms a beam into a comb like structure where flexural cracks are created in the tensile region giving an appearance of more or less like a concrete teeth and a compression region on top of the tension zone which represents the backbone of the comb (Fig. 7.10a). Cracks start to appear on the beam long before the allowable load is reached. These cracks are narrow and starts to increase in length and width upon further increase of load, resulting in the decrease of compression zone as the crack propagates upwards. The inclusion of all interacting effects have been incorporated into the novel kinematic

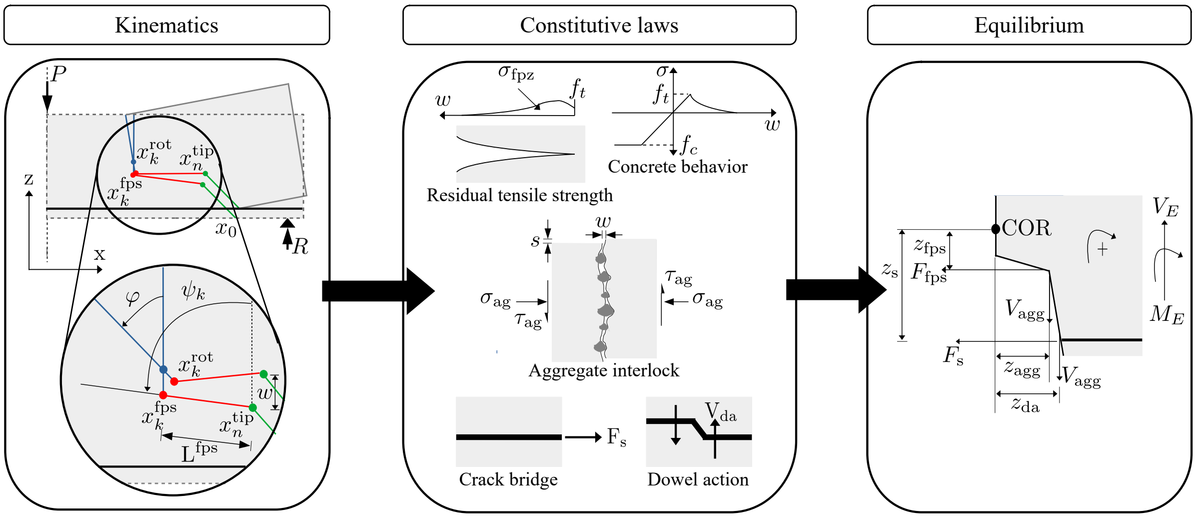

(a) (b) (c)

Figure 7.9: (a) Crack kinematics (b) constitutive laws (c) equilibrium

model to calculate the vertical stress at the tip of the crack due to the cantilever action (Fig. 7.10b).

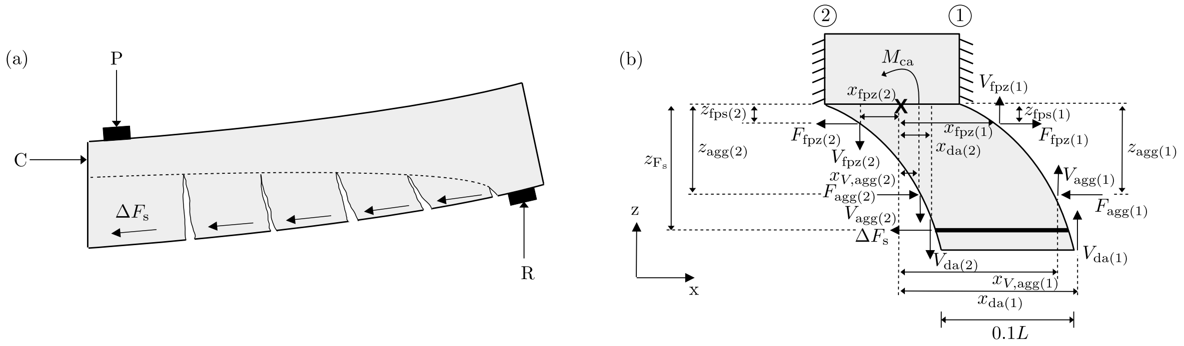

Figure 7.10: (a) Concrete teeth (b) Cantilever action in between two identical cracks

All the shear transfer actions in the dissected concrete tooth are assumed to be alike. Furthermore, the model also takes into account the changing length, geometry of the crack and the lever arms as the crack propagates upwards towards the compression zone. Hence, a general equation to obtain the clamping moment can be written as:

$$\begin{gathered} M_{\text{Ca}} = V_{\text{fpz}(2)} x_{\text{fpz}(2)} - V_{\text{fpz}(1)} x_{\text{fpz}(1)} + \\ V_{\text{agg}(2)} x_{\text{V,agg}(2)} - V_{\text{agg}(1)} x_{\text{V,agg}(1)} + V_{\text{da}(2)} x_{\text{da}(2)} - V_{\text{da}(2)} x_{\text{da}(1)} + \Delta F_{\text{s}} z_{\text{Fs}} \end{gathered} \tag{7.117}$$

where, ΔF_s is limited by bond strength properties between reinforcement and concrete and with an assumption that the tensile force in the reinforcement reduces linearly from maximum bending moment region to zero bending moment region for the type of shear span considered in our calculation. Hence, the vertical stress can be expressed as:

$$\sigma_z = \frac{M_{\mathrm{Ca}}}{B(0.1L)^2/6} \tag{7.118}$$

7.10 Algorithm and iteration scheme

In order to evaluate the shear crack propagation along the beam, the iterative procedure of the DCPM is elaborated here as follows (see Fig. 7.11):

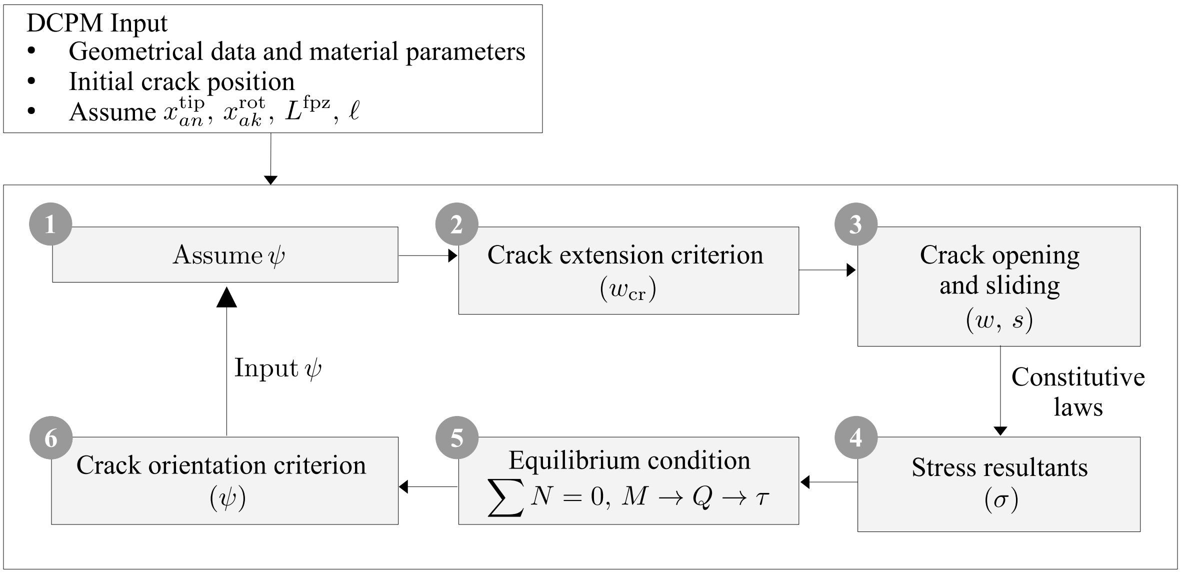

Figure 7.11: Iteration algorithm of DCPM

1. ψ, x_{an}^{tip}, x_{ak}^{rot}, L^{fps} and ℓ are assumed and taken as the input parameters for the numerical simulation of the crack algorithm. The length of the fracture process zone segment L^{fps} and length of each iteration step ℓ is fixed throughout the simulation.
2. The model considers a crack orientation criterion that serves as basis for crack extension. Upon crack extension, the state parameters of the crack tip object, namely ψ, x_{1k}^{rot} are reset to the values at the previous step and the next iterative solution is obtained. Furthermore, the state of $x_{\mathrm{an}}^{\mathrm{tip}}$ also gets updated along each step of iteration.
3. The crack opening and sliding kinematics (w, s) are evaluated.
4. After the calculation of crack opening and sliding kinematics, constitutive laws to incorporate interacting effects are used, which evaluates the local and global stress resultants.

5. Two equilibrium conditions are considered as the model has two unknowns (i.e.$\psi, x_{ak}^{\text{rot}}$).
6. In the end, the model incorporates a crack orientation criterion. Once that is evaluated, the loop continues from step 1 to evaluate the next crack extension. It is pertinent to mention here that x_{an}^{tip} and x_{ak}^{rot} are evaluated by the simulator and updated for each iteration step.
7. The value of ψ is calculated using the previous segment of the crack path.
8. The model also needs the number of segments to be defined and the incremental loop continues running until the assigned number of iterations are reached or until convergence is lost.

7.11 Comparison between analytical models

A brief comparison in between the recently proposed analytical models and the currently under-development discrete model is done to highlight the differences in the assumptions adopted in these models.

Model Comparisons			
Characteristics	DCPM (2023)	CSCT (2018)	SCPT (2020)
Initial assumptions	The initial position of the crack, length of the fracture process zone segment, initial angle of orientation and the initial location of the COR at mid height of the section is assumed.	The location of the critical crack and the initial crack opening is assumed.	In SCPT, the geometrical data and the material properties, crack geometry of step (i-1) and the structural system is assumed and a certain depth of the compression zone is imposed.

Center of rotation	The center of rotation is assumed to be located vertically above the crack tip when the crack tip is in tension while the COR moves vertically below the crack tip when the crack tip moves into compression zone.	The COR is assumed to be located at the tip of the crack.	The center of rotation is assumed to be located vertically above the crack tip when the crack tip is in tension while the COR moves vertically below the crack tip when the crack tip moves into compression zone.
Critical crack opening	The critical crack opening is a function of fracture energy and the tensile strength of concrete.	It is a function of normal strain in longitudinal reinforcement and depth of cross section until steel reinforcement.	The critical crack opening is a function of fracture energy and the tensile strength of concrete.
Opening profiles along the crack	The crack opening profile is considered to be linear while slip is nonlinear. Both are obtained from the rotation state of the segment points with respect to the COR.	The crack opening profile is linear while the slip is assumed to depict a constant profile.	Crack opening is linear and slip is constant. Both are a function of the COR.
Opening displacements at steel	The opening displacement at steel reinforcement is calculated by extrapolation.	It is a product of tributary length times the strain at the level of reinforcement.	The opening displacement is calculated from rotation around COR.
Distance between cracks	$0.1L$	$l_B = d - c$	$s_{cr} = 0.7d$

Depth of compression zone	Compression zone depth incorporates both concrete in tension and compression.	Calculated by assuming linear response of concrete in compression and neglecting concrete in tension.	Compression zone incorporates both concrete in tension and compression.
Crack Shape	Incremental nonlinear	Bilinear (top part: Mode I, bottom part: Mixed Mode)	In its simplest form includes a bilinear crack along with a horizontal delamination crack.
Crack propagation criterion	Included	Missing	Included
Uncracked section Contribution	Parabolic equation for shear stresses distribution at the crack tip and integrating it along the uncracked region to get the uncracked force contribution.	Calculated by incorporating the force contribtutions from residual action, aggregate interlock, dowel action and reducing it by a factor.	Parabolic equation for shear stresses distribution at the crack tip and integrating it along the uncracked region to get the uncracked force contribution.
Total Shear Capacity	Obtained by calculating the moment distribution along center of rotation.	Calculated by a simple summation of the force resultants from all the actions.	Shear capacity obtained by calculating the moment along steel reinforcement incorporating all the individual components of the shear zones.

Iteration procedure	The primary unknowns are the center of rotation and the inclination angle of a new crack segment.	The primary unknowns are the crack orientation angle and the initial crack opening that is adjusted upon iteration.	The primary unknowns are the crack extension length, crack orientation angle, vertical stress and the center of rotation. That are iteratively calculated and adjusted.

7.12 Verification studies

A simply supported beam is assumed here for performing simulations from the proposed crack propagation model (see Table 7.2). The results show various advantages of this novel approach which are discussed here. The model can simulate the stresses in a crack and is able to depict the history of stress distributions throughout the crack profile until failure. The stress states for three different positions along the height of propagating crack located at the center of the beam are shown in Fig. 7.12 (ab). The stress at crack tip is illustrated with red line. The stress profile visualizes all positions i.e. crack tip, fracture process zone and center of rotation.

Another important aspect of the model is its ability to show force distributions along the history of the propagating crack. To explain the clear picture, three different crack positions are selected i.e. 0.1L, 0.5L, 0.9L (see Fig. 7.12 a). The corresponding results are plotted for two shear zone actions (aggregate interlock and dowel action (see Fig. 7.12de)). The obtained results are shown here for the same three vertical positions of the crack discussed above. A significant rise in the force contributions can be seen for both

Table 7.2: Geometrical parameters of beam

Material parameters	**Values**
Shear span	3850 mm
Cross-section	250 x 600
Comp. strength of concrete	33.3 N/mm^2
Dia. of aggregate	16 mm
Number of bars	2
Bar diameter	28 mm
Yield strength of steel	713 N/mm^2

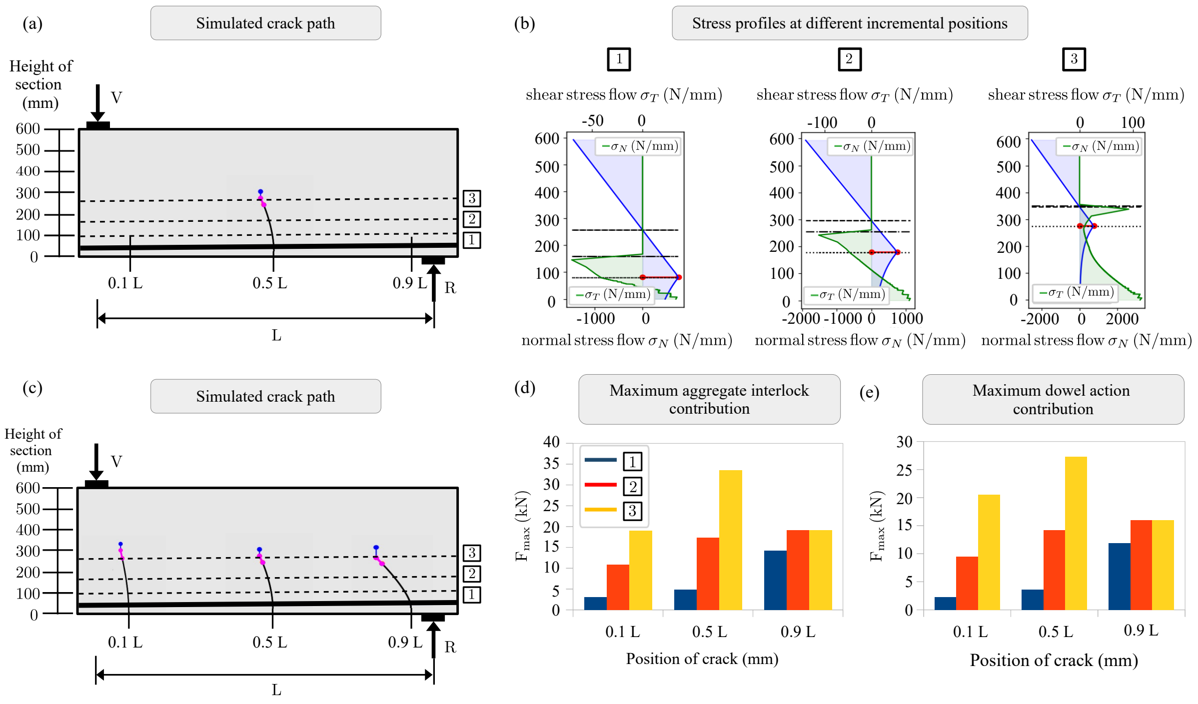

Figure 7.12: (a) Simulated crack paths, (b) stress profiles at different incremental positions, (c) simulated crack paths of three selected cracks, (d) maximum aggregate interlock contribution, (e) maximum dowel action contribution

0.1L and 0.5L crack but the spike in force contributions for 0.9L is not as remarkable as observed for other two cracks. This behaviour of the maximum force contributions is expected to improve by the incorporation of a crack propagation criterion and further effects i.e. cantilever action.

The efficiency of models analysing shear crack propagation are crucial for their applicability in engineering practice. This computational complexity of the model is demonstrated in Fig. 7.13a where the crack located at the center of the beam is analysed. Fig. 7.13a illustrates the time taken for the complete simulation against number of simulated crack propagation steps. This example shows that 140 crack segments are obtained within 25 seconds indicating a relatively fast convergence to equilibrium. The corresponding load deflection curve is plotted in Fig. 7.13b.

Maximum dowel action and aggregate force contributions are also plotted to contribute towards ongoing discussion of the role or significance of individual components contributing towards shear strength. The performed study shows that for the chosen constitutive laws, the effect of the dowel action is slightly higher than the aggregate interlock closer to the loading point but this trend changes and it appears that aggregate interlock is governing contributor towards shear capacity as we move away towards the support (Fig. 7.14c).

The maximum shear capacity is plotted in Fig. 7.14b. The shear capacity tends to increase towards the support. Still, this result is only preliminary as the crack propagation

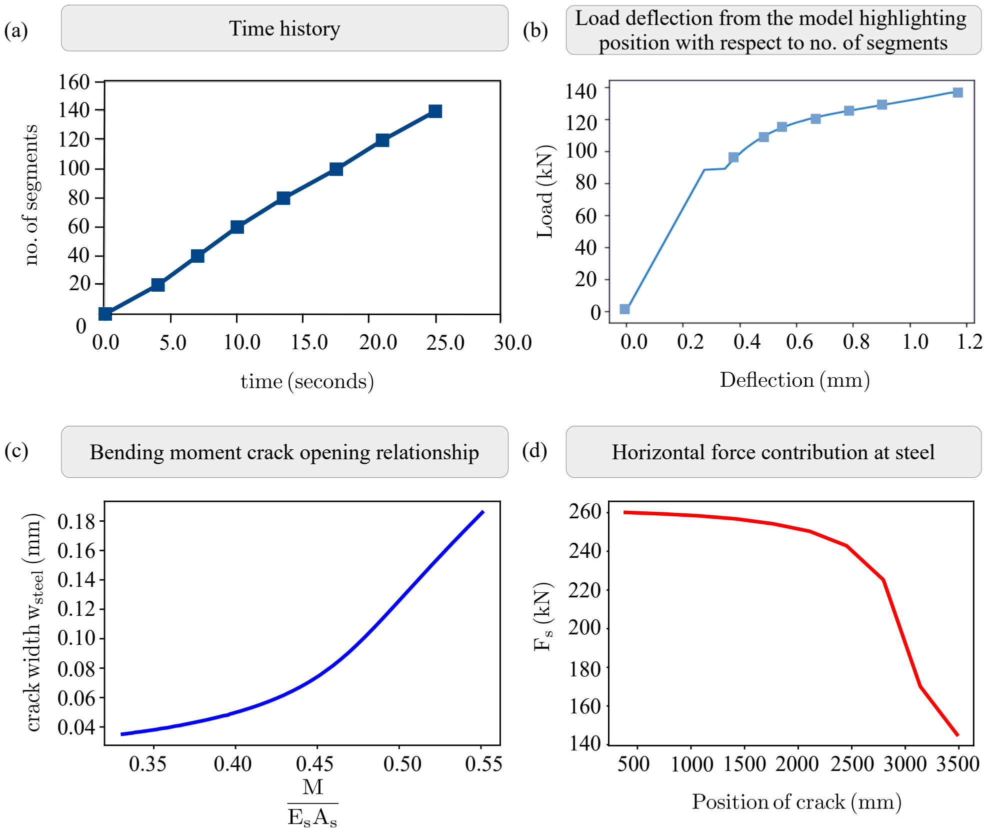

Figure 7.13: (a) Segment and calculation time relationship, (b) load deflection curve, (c) bending moment and crack opening relationship, (d) horizontal force contribution

criterion and eventually further effects, like cantilever action are not yet added to the model. Enriched with these model components, more detailed studies can be performed and validated based on experimental results. The shown simulations are performed for 9 different crack positions but only three different locations are highlighted here for clarity (Fig. 7.14a).

The model is also able to simulate any experimental result such as the bending moment-crack opening relationship as shown in Fig. 7.13c. The result of bending moment crack opening relationship shows a realistic behaviour. The horizontal steel force (Fig. 7.13d) from the model also shows a realistic trend i.e. the force contribution is decreasing towards the support. This action is needed to improve further in the model for the state at which high crack parallel stress and a crack orientation criterion (i.e. maximum principal stress theory) develops in the compression zone.

7.13 Conclusions

The aim of this chapter is to provide a new perspective on the role and significance of various actions within a shear zone towards shear capacity using a novel approach. Currently, the technique is still under development and can only incorporate SCPT. How-

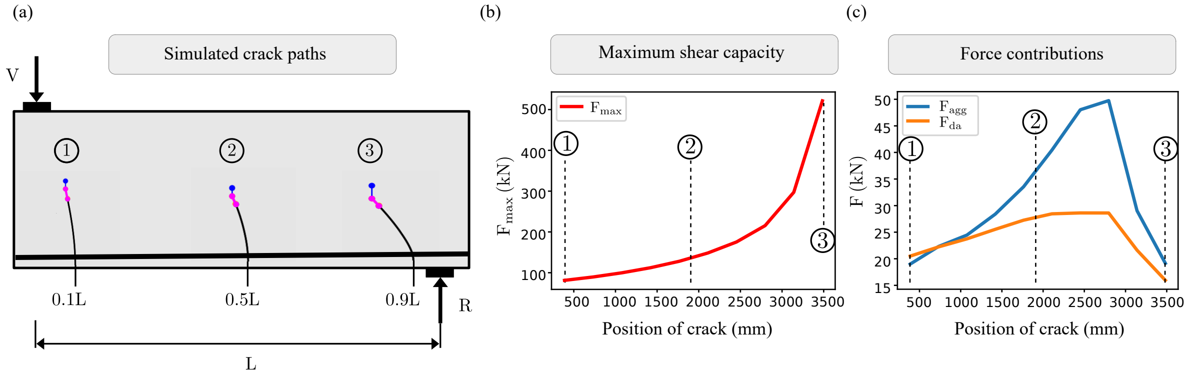

Figure 7.14: (a) Simulated crack path, (b) maximum shear capacity, dowel and aggregate force contributions

ever, some conclusions can already be drawn from the discrete crack propagation model (DCPM):

- The discrete crack propagation model (DCPM) can display stress profiles, force contributions from individual actions, and maximum shear capacity.
- The DCPM is highly efficient and can simulate numerous segments within seconds.
- The kinematics of the DCPM shows promising results, and further improvements are expected with the incorporation of crack orientation criteria and crack parallel stress.
- The study found that the contribution of dowel action is higher than aggregate interlock in the initial crack positions, but aggregate interlock becomes more significant towards the support.
- The DCPM demonstrates reasonable behavior in terms of horizontal force acting at the steel throughout the beam and the bending moment-crack opening relationship.

8 Summary and Outlook

This dissertation focuses on the development of a novel tool, the Damage-Based Crack Detection Tool (DCDT), which is designed to extract displacement fields from images obtained through Digital Image Correlation (DIC). The DCDT addresses the need for advanced crack detection techniques by integrating the displacement history from DIC images with the constitutive behavior of the concrete matrix, which refers to the fundamental properties and relationships that govern concrete's response under various stress and strain conditions. This integration is crucial, as it enables a precise time-space approximation that captures the strain, stress, and damage fields within the material. These fields are critical for effectively identifying and monitoring cracks as they develop and propagate within concrete structures.

The DCDT applies a unique damage-based crack identification scheme that goes beyond traditional strain distribution analysis. This approach prioritizes local damage information to detect both primary cracks, which typically signify major structural changes, and more complex crack patterns such as branched and closely spaced cracks. These complex crack forms are often challenging to detect and assess using conventional crack detection techniques, which may lack the precision needed to distinguish closely spaced or intricately branched cracks. By focusing on local damage rather than relying solely on strain distributions, the DCDT offers a significant advantage in detecting and characterizing these complex cracking patterns, thereby providing a more detailed understanding of the structural integrity of concrete materials.

One of the DCDT's main functions is to analyze the kinematic behavior of crack openings and sliding motions, which are critical parameters in understanding the overall deformation and potential failure of a structure. The crack opening and sliding kinematics provide essential insights into the behavior of cracks under stress, offering a more comprehensive understanding of how cracks propagate and evolve. These parameters are then used as input to extract stress resultants along identified cracks using established constitutive laws for concrete. By applying these laws, the tool can quantify the stress fields and force distributions that occur along the path of a crack. This analysis is instrumental in evaluating the structural stability of the material and can guide decision-making processes related to repair or reinforcement.

Additionally, the DCDT evaluates the center of rotation (COR), which is a critical component in the study of crack mechanics. The COR provides a reference point for understanding the rotational behavior of cracked regions and can validate assumptions in various analytical models that describe crack propagation and deformation. By accurately identifying the COR, the DCDT enhances the precision of these models, which are often based on theoretical assumptions about crack behavior. Validating these assumptions with real data from the DCDT strengthens the models' reliability and can improve predictive capabilities for future analyses of similar structures.

A further focus of the dissertation is the development of an analytical model for shear crack propagation, which builds upon kinematic assumptions about the movement and interaction of cracks within the concrete matrix. This analytical model is designed to enhance the understanding of shear failure mechanisms, which are particularly complex due to the nature of shear forces and their interactions with material properties. Ongoing work on this model includes integrating the varied crack patterns and COR data generated by the DCDT into a dynamic, discrete crack propagation model. This model aims to represent the evolving nature of crack behavior under shear forces more accurately and can potentially provide deeper insights into the conditions that lead to shear failure.

In addition to presenting the DCDT and the associated analytical model, this thesis outlines areas for future research to further refine the tool and its applications. One avenue for continued research involves refining the constitutive laws used to analyze interacting effects within the concrete matrix, particularly those that influence the combined kinematics of crack opening, sliding, and rotation. Another suggested area of investigation involves comparing crack kinematics derived from the analytical model with empirical data from DCDT, which could validate the model's assumptions and enhance its accuracy.

Although this dissertation presents results from four beams out of a total of ten tested, the findings highlight the potential of the DCDT to examine a broader range of cracking patterns across different concrete structures. By identifying centers of rotation and assessing force contributions at different points within a structure, the DCDT offers a new lens through which to understand concrete mechanics and crack behavior. This expanded understanding could have wide-reaching implications for structural monitoring, repair, and longevity, making the DCDT a valuable addition to the field of concrete mechanics. Overall, the tool's capabilities for assessing cracking patterns, identifying COR, and analyzing force contributions underscore its potential to advance our understanding of structural behavior under various loading conditions.

Bibliography

[gom, 2019] (2019). Gom correlate professional: Gom software 2019.

[gom, 2020] (2020). 3d testing technical documentation: Digital image correlation and strain computation basics: Copyright 2016.

[Abdullah Dönmez et al., 2020] Abdullah Dönmez, A., Carloni, C., Cusatis, G., and Bažant, Z. P. (2020). Size effect on shear strength of reinforced concrete: Is csct or mcft a viable alternative to energy-based design code? *Journal of Engineering Mechanics*, 146(10):04020110.

[Adam, 2021a] Adam, V. (2021a). *Shear in Reinforced Concrete Structures without Shear Reinforcement – Analysis and Design*. PhD thesis, Aachen, Germany: RWTH Aachen University.

[Adam, 2021b] Adam, V. F. (2021b). *Shear in reinforced concrete structures without shear reinforcement : analysis and design*. Dissertation, Rheinisch-Westfälische Technische Hochschule Aachen, Aachen.

[Alam et al., 2015] Alam, S. Y., Loukili, A., Grondin, F., and Rozière, E. (2015). Use of the digital image correlation and acoustic emission technique to study the effect of structural size on cracking of reinforced concrete. *Engineering Fracture Mechanics*, 143:17–31.

[Baktheer and Becks, 2021] Baktheer, A. and Becks, H. (2021). Fracture mechanics based interpretation of the load sequence effect in the flexural fatigue behavior of concrete using digital image correlation. *Construction and Building Materials*, 307.

[Baktheer et al., 2024a] Baktheer, A., Esfandiari, S., Aguilar, M., Becks, H., Classen, M., and Chudoba, R. (2024a). Fatigue-induced stress redistribution in prestressed concrete beams modeled using the constitutive hypothesis of inter-aggregate degradation. *Fatigue & Fracture of Engineering Materials & Structures*.

[Baktheer et al., 2024b] Baktheer, A., Goralski, C., Hegger, J., and Chudoba, R. (2024b). Stress configuration-based classification of current research on fatigue of reinforced and prestressed concrete. *Structural Concrete*.

[Baktheer et al., 2024c] Baktheer, A., Martínez-Pañeda, E., and Aldakheel, F. (2024c). Phase field cohesive zone modeling for fatigue crack propagation in quasi-brittle materials. *Computer Methods in Applied Mechanics and Engineering*, page 116834.

[Baumann and Rüsch, 1970a] Baumann, T. and Rüsch, H. (1970a). *Schubversuche mit indirekter Krafteinleitung: versuche zum studium der Verdübelungswirkung der Biegezugbewehrung eines Stahlbetonbalkens*. W. Ernst.

[Baumann and Rüsch, 1970b] Baumann, T. and Rüsch, H. (1970b). Tests on dowelling action of flexural reinforcement of reinforced concrete beams. *Deutscher Ausscuss für Stahlbeton*, 210:42–83.

[Bazant and Gambarova, 1980] Bazant, Z. P. and Gambarova, P. (1980). Rough cracks in reinforced concrete. *ASCE J Struct Div*, 106(4):819–842.

[Bažant and Gambarova, 1980] Bažant, Z. P. and Gambarova, P. (1980). Rough cracks in reinforced concrete. *Journal of the Structural Division*, 106(4):819–842.

[Bažant and Planas, 2019] Bažant, Z. P. and Planas, J. (2019). *Fracture and size effect in concrete and other quasibrittle materials*. Routledge.

[Becks et al., 2023] Becks, H., Baktheer, A., Marx, S., Classen, M., Hegger, J., and Chudoba, R. (2023). Monitoring concept for the propagation of compressive fatigue in externally prestressed concrete beams using digital image correlation and fiber optic sensors. *Fatigue & Fracture of Engineering Materials & Structures*, 46(2):514–526.

[Becks et al., 2022] Becks, H., Bielak, J., Camps, B., and Hegger, J. (2022). Application of fiber optic measurement in textile-reinforced concrete testing. *Structural Concrete*, 23(4):2600–2614.

[Belytschko and Black, 1999] Belytschko, T. and Black, T. (1999). Elastic crack growth in finite elements with minimal remeshing. *International journal for numerical methods in engineering*, 45(5):601–620.

[Besnard et al., 2006] Besnard, G., Hild, F., and Roux, S. (2006). Finite-element displacement fields analysis from digital images: application to portevin–le châtelier bands. *Experimental mechanics*, 46(6):789–803.

[Bi et al., 2021] Bi, J., Wang, Z., Zhao, Y., Huo, L., and Xie, Y. (2021). A mechanical model for shear design of steel fiber reinforced concrete beams without shear reinforcements. In *Structures*, volume 31, pages 216–229. Elsevier.

[Bosbach, 2024] Bosbach, S. (2024). *Shear in carbon reinforced conrete- A physically based model to characterize the structural behaviour*. Dissertation, Rheinisch-Westfälische Technische Hochschule Aachen, Aachen.

[Broberg, 2013] Broberg, P. (2013). Surface crack detection in welds using thermography. *NDT & E International*, 57:69–73.

[Brooks et al., 2015] Brooks, W. S., Lamb, D. A., and Irvine, S. J. (2015). Ir reflectance imaging for crystalline si solar cell crack detection. *IEEE journal of photovoltaics*, 5(5):1271–1275.

[Cantone et al., 2022] Cantone, R., Setiawan, A., Ruiz, M. F., and Muttoni, A. (2022). Characterization of shear deformations in reinforced concrete members without shear reinforcement. *Engineering Structures*, 257:113910.

[Cavagnis, 2017] Cavagnis, F. (2017). Shear in reinforced concrete without transverse reinforcement. Technical report, EPFL.

[Cavagnis et al., 2018a] Cavagnis, F., Fernández Ruiz, M., and Muttoni, A. (2018a). An analysis of the shear-transfer actions in reinforced concrete members without transverse reinforcement based on refined experimental measurements. *Structural concrete*, 19(1):49–64.

[Cavagnis et al., 2015] Cavagnis, F., Ruiz, M. F., and Muttoni, A. (2015). Shear failures in reinforced concrete members without transverse reinforcement: An analysis of the critical shear crack development on the basis of test results. *Engineering structures*, 103:157–173.

[Cavagnis et al., 2018b] Cavagnis, F., Ruiz, M. F., and Muttoni, A. (2018b). A mechanical model for failures in shear of members without transverse reinforcement based on development of a critical shear crack. *Engineering structures*, 157:300–315.

[Cha et al., 2017] Cha, Y.-J., Choi, W., and Büyüköztürk, O. (2017). Deep learning-based crack damage detection using convolutional neural networks. *Computer-Aided Civil and Infrastructure Engineering*, 32(5):361–378.

[Chengsheng et al., 1990] Chengsheng, O., Barzin, M., et al. (1990). An r-curve approach for fracture of quasi-brittle materials. *Engineering fracture mechanics*, 37(4):901–913.

[Choi and Shah, 1997] Choi, S. and Shah, S. (1997). Measurement of deformations on concrete subjected to compression using image correlation. *Experimental mechanics*, 37(3):307–313.

[Chudoba et al., 2022] Chudoba, R., Seemab, F., and Baktheer, A. (2022). bmcs_shear_zone package repository.

[Classen, 2020] Classen, M. (2020). Shear crack propagation theory (scpt)–the mechanical solution to the riddle of shear in rc members without shear reinforcement. *Engineering Structures*, 210:110207.

[Code, 1990] Code, C.-F. M. (1990). Ceb-fip model code for concrete structures, euro-international committe for concrete. *Bulletin*, (213/214).

[Code, 2010] Code, M. (2010). International federation for structural concrete (fib), lausanne, 2010; vol. *l Bulletin*, 55.

[Collins and Kuchma, 1999] Collins, M. P. and Kuchma, D. (1999). How safe are our large, lightly reinforced concrete beams, slabs, and footings? *Structural Journal*, 96(4):482–490.

[Committee, 2008] Committee, A. (2008). Building code requirements for structural concrete (aci 318-08) and commentary. American Concrete Institute.

[Dhital and Lee, 2012] Dhital, D. and Lee, J.-R. (2012). A fully non-contact ultrasonic propagation imaging system for closed surface crack evaluation. *Experimental mechanics*, 52(8):1111–1122.

[Donmez and Bazant, 2018] Donmez, A. and Bazant, Z. P. (2018). Critique of Critical Shear Crack Theory (CSCT) for fib Model Code Articles on Shear Strength and Size Effect of RC Beams. *arXiv:1810.11506 [physics]*. arXiv: 1810.11506.

[Dönmez and Bažant, 2019] Dönmez, A. and Bažant, Z. P. (2019). Critique of critical shear crack theory for fib model code articles on shear strength and size effect of reinforced concrete beams. *Structural Concrete*, 20(4):1451–1463.

[Dönmez et al., 2020] Dönmez, A., Carloni, C., Cusatis, G., and Bažant, Z. P. (2020). Discussion of the article "from experimental evidence to mechanical modeling and design expressions: The critical shear crack theory for shear design". *Structural Concrete*, 21(4):1688–1689.

[EN, 1992] EN, B. (1992). 1-1: 2004 design of concrete structures. *General rules and rules for buildings*.

[Faron and Rombach, 2020] Faron, A. and Rombach, G. A. (2020). Simulation of crack growth in reinforced concrete beams using extended finite element method. *Engineering Failure Analysis*, 116:104698.

[Fernández Ruiz et al., 2013] Fernández Ruiz, M., Mirzaei, Y., and Muttoni, A. (2013). Post-punching behavior of flat slabs. *ACI Structural Journal*, 110(ARTICLE):801–812.

[Fernández Ruiz and Muttoni, 2018] Fernández Ruiz, M. and Muttoni, A. (2018). Size effect in shear and punching shear failures of concrete members without transverse reinforcement: Differences between statically determinate members and redundant structures. *Structural concrete*, 19(1):65–75.

[Fernández Ruiz et al., 2010] Fernández Ruiz, M., Plumey, S., and Muttoni, A. (2010). Interaction between bond and deviation forces in spalling failures of arch-shaped members without transverse reinforcement. *ACI Structural Journal*, 107(ARTICLE):346–354.

[Gambarova and Karakoç, 1983] Gambarova, P. and Karakoç, C. (1983). A new approach to the analysis of the confinement role in regularly cracked concrete elements.

[Gehri et al., 2020] Gehri, N., Mata-Falcón, J., and Kaufmann, W. (2020). Automated crack detection and measurement based on digital image correlation. *Construction and Building Materials*, 256:119383.

[Ghiassi et al., 2013] Ghiassi, B., Xavier, J., Oliveira, D. V., and Lourenço, P. B. (2013). Application of digital image correlation in investigating the bond between frp and masonry. *Composite Structures*, 106:340–349.

[Guo and Vavilov, 2013] Guo, X. and Vavilov, V. (2013). Crack detection in aluminum parts by using ultrasound-excited infrared thermography. *Infrared Physics & Technology*, 61:149–156.

[Görtz, 2004] Görtz, S. (2004). *Zum Schubrissverhalten von Stahlbeton- und Spannbetonbalken aus Normal- und Hochleistungsbeton*. PhD thesis, Aachen. Aachen, Techn. Hochsch., Diss., 2004.

[Harris et al., 2020] Harris, C. R., Millman, K. J., van der Walt, S. J., Gommers, R., Virtanen, P., Cournapeau, D., Wieser, E., Taylor, J., Berg, S., Smith, N. J., Kern, R., Picus, M., Hoyer, S., van Kerkwijk, M. H., Brett, M., Haldane, A., del Río, J. F., Wiebe, M., Peterson, P., Gérard-Marchant, P., Sheppard, K., Reddy, T., Weckesser, W., Abbasi, H., Gohlke, C., and Oliphant, T. E. (2020). Array programming with NumPy. *Nature*, 585(7825):357–362.

[Hegger et al., 2004] Hegger, J., Sherif, A., and Gortz, S. (2004). Investigation of pre- and postcracking shear behavior of prestressed concrete beams using innovative measuring techniques. *Structural Journal*, 101(2):183–192.

[Helm, 2008] Helm, J. D. (2008). Digital image correlation for specimens with multiple growing cracks. *Experimental mechanics*, 48(6):753–762.

[Herbrand, 2017] Herbrand, M. (2017). *Shear strength models for reinforced and prestressed concrete members*. Dissertation, RWTH Aachen University, Aachen.

[Hild et al., 2002] Hild, F., Raka, B., Baudequin, M., Roux, S., and Cantelaube, F. (2002). Multiscale displacement field measurements of compressed mineral-wool samples by digital image correlation. *Applied optics*, 41(32):6815–6828.

[Hillebrand, 2023] Hillebrand, M. (2023). *Ermüdung der Querkraftbewehrung in Spannbetonträgern*. Dissertation, Rheinisch-Westfälische Technische Hochschule Aachen, Aachen.

[Hoover and Bažant, 2014] Hoover, C. G. and Bažant, Z. P. (2014). Cohesive crack, size effect, crack band and work-of-fracture models compared to comprehensive concrete fracture tests. *International Journal of Fracture*, 187(1):133–143.

[Hoover et al., 2013] Hoover, C. G., Bažant, Z. P., Vorel, J., Wendner, R., and Hubler, M. H. (2013). Comprehensive concrete fracture tests: Description and results. *Engineering fracture mechanics*, 114:92–103.

[Hordijk, 1992] Hordijk, D. A. (1992). Tensile and tensile fatigue behaviour of concrete; experiments, modelling and analyses. *Heron*, 37(1).

[Huber et al., 2016] Huber, P., Huber, T., and Kollegger, J. (2016). Investigation of the shear behavior of rc beams on the basis of measured crack kinematics. *Engineering Structures*, 113:41–58.

[Iliopoulos et al., 2015] Iliopoulos, S., Aggelis, D., Pyl, L., Vantomme, J., Van Marcke, P., Coppens, E., and Areias, L. (2015). Detection and evaluation of cracks in the concrete buffer of the belgian nuclear waste container using combined ndt techniques. *Construction and Building Materials*, 78:369–378.

[Irwin, 1957] Irwin, G. R. (1957). Analysis of stresses and strains near the end of a crack traversing a plate.

[Islam and Kim, 2019] Islam, M. and Kim, J.-M. (2019). Vision-based autonomous crack detection of concrete structures using a fully convolutional encoder–decoder network. *Sensors*, 19(19):42–51.

[Jacobsen et al., 2012] Jacobsen, J. S., Poulsen, P. N., and Olesen, J. F. (2012). Characterization of mixed mode crack opening in concrete. *Materials and structures*, 45(1-2):107–122.

[Janiak et al., 2023] Janiak, T., Becks, H., Camps, B., Classen, M., and Hegger, J. (2023). Evaluation of distributed fibre optic sensors in structural concrete. *Materials and Structures*, 56(9):159.

[Jimenez, 1979] Jimenez, P. R. (1979). Shear transfer across cracks in reinforced concrete.

[Jirásek, 1999] Jirásek, M. (1999). Comments on microplane theory. *Mechanics of quasi-brittle materials and structures*, pages 55–77.

[Jirásek, 2011] Jirásek, M. (2011). Damage and smeared crack models. In *Numerical modeling of concrete cracking*, pages 1–49. Springer.

[Kani, 1964] Kani, G. (1964). The riddle of shear failure and its solution. In *Journal Proceedings*, volume 61, pages 441–468.

[Koščak et al., 2022] Koščak, J., Damjanović, D., Bartolac, M., and Duvnjak, I. (2022). Shear behavior of rc beams without transverse reinforcement: An analysis of crack kinematics and transfer mechanisms based on stereophotogrammetric measurements. *Engineering Structures*, 255:113886.

[Küntz et al., 2006] Küntz, M., Jolin, M., Bastien, J., Perez, F., and Hild, F. (2006). Digital image correlation analysis of crack behavior in a reinforced concrete beam during a load test. *Canadian Journal of Civil Engineering*, 33(11):1418–1425.

[Kupfer and Gerstle, 1973] Kupfer, H. B. and Gerstle, K. H. (1973). Behavior of concrete under biaxial stresses. *Journal of the Engineering Mechanics Division*, 99(4):853–866.

[Li et al., 2018] Li, Y., Li, H., and Wang, H. (2018). Pixel-wise crack detection using deep local pattern predictor for robot application. *Sensors*, 18(9):3042.

[Liu et al., 2019] Liu, Z., Cao, Y., Wang, Y., and Wang, W. (2019). Computer vision-based concrete crack detection using u-net fully convolutional networks. *Automation in Construction*, 104:129–139.

[Luo et al., 2019] Luo, Q., Ge, B., and Tian, Q. (2019). A fast adaptive crack detection algorithm based on a double-edge extraction operator of fsm. *Construction and Building Materials*, 204:244–254.

[Marí et al., 2015] Marí, A., Bairán, J., Cladera, A., Oller, E., and Ribas, C. (2015). Shear-flexural strength mechanical model for the design and assessment of reinforced concrete beams. *Structure and Infrastructure Engineering*, 11(11):1399–1419.

[Merazi Meksen et al., 2010] Merazi Meksen, T., Boudraa, B., Drai, R., and Boudraa, M. (2010). Automatic crack detection and characterization during ultrasonic inspection. *Journal of Nondestructive Evaluation*, 29(3):169–174.

[Mohan and Poobal, 2018] Mohan, A. and Poobal, S. (2018). Crack detection using image processing: A critical review and analysis. *Alexandria Engineering Journal*, 57(2):787–798.

[Muller et al., 2004] Muller, M., Toussaint, E., Destrebecq, J.-F., and Grédiac, M. (2004). Experimental and numerical study of reinforced concrete specimens strengthened with composite plates. *Composites Part A: Applied Science and Manufacturing*, 35(7-8):885–893.

[Muttoni, 2008] Muttoni, A. (2008). Punching shear strength of reinforced concrete slabs without transverse reinforcement. *ACI structural Journal*, 105(ARTICLE):440–450.

[Muttoni and Fernández Ruiz, 2008] Muttoni, A. and Fernández Ruiz, M. (2008). Shear strength of members without transverse reinforcement as function of critical shear crack width. *ACI Structural Journal*, 105(ARTICLE):163–172.

[Muttoni and Fernández Ruiz, 2019] Muttoni, A. and Fernández Ruiz, M. (2019). From experimental evidence to mechanical modeling and design expressions: The critical shear crack theory for shear design. *Structural Concrete*, 20(4):1464–1480.

[Muttoni and Fernandez Ruiz, 2020] Muttoni, A. and Fernandez Ruiz, M. (2020). Authors' closure on the discussion of the article:"from experimental evidence to mechanical modeling and design expressions: The critical shear crack theory for shear design"(discussion by dönmez et al.). *Structural Concrete*, 21(4):1690–1692.

[Muttoni and Schwartz, 1991] Muttoni, A. and Schwartz, J. (1991). Behavior of beams and punching in slabs without shear reinforcement. In *IABSE colloquium*, volume 62, pages 703–708. IABSE colloquium.

[Mündecke and Mechtcherine, 2020] Mündecke, E. and Mechtcherine, V. (2020). Tensile behaviour of strain-hardening cement-based composites (SHCC) with steel reinforcing bars. *Cement and Concrete Composites*, 105:103423.

[Nocedal and Wright, 1999] Nocedal, J. and Wright, S. J. (1999). *Numerical optimization*. Springer.

[Ouyang and Shah, 1991] Ouyang, C. and Shah, S. P. (1991). Geometry-dependent r-curve for quasi-brittle materials. *Journal of the American ceramic society*, 74(11):2831–2836.

[pandas development team, 2020] pandas development team, T. (2020). pandas-dev/pandas: Pandas.

[Pascale and Lolli, 2015] Pascale, G. and Lolli, A. (2015). Crack assessment in marble sculptures using ultrasonic measurements: Laboratory tests and application on the statue of david by michelangelo. *Journal of Cultural Heritage*, 16(6):813–821.

[Pei et al., 2016] Pei, C., Qiu, J., Liu, H., and Chen, Z. (2016). Simulation of surface cracks measurement in first walls by laser spot array thermography. *Fusion Engineering and Design*, 109:1237–1241.

[Pereira and Pereira, 2015] Pereira, F. C. and Pereira, C. E. (2015). Embedded image processing systems for automatic recognition of cracks using uavs. *Ifac-PapersOnline*, 48(10):16–21.

[Reineck, 1990] Reineck, K. (1990). Mechanical model for the behaviour of reinforced concrete members in shear. *PhD thesis, University of Stuttgart*, pages 1–273.

[Reineck, 1991] Reineck, K.-H. (1991). Ultimate shear force of structural concrete members without transverse reinforcement derived from a mechanical model (sp-885). *Structural Journal*, 88(5):592–602.

[Reinhardt, 1984] Reinhardt, H. W. (1984). Fracture mechanics of an elastic softening material like concrete. *HERON, 29 (2), 1984*.

[Ribas Gonzalez and Fernández Ruiz, 2017] Ribas Gonzalez, C. R. and Fernández Ruiz, M. (2017). Influence of flanges on the shear-carrying capacity of reinforced concrete beams without web reinforcement. *Structural concrete*, 18(5):720–732.

[Rodríguez-Martín et al., 2016] Rodríguez-Martín, M., Lagüela, S., González-Aguilera, D., and Martínez, J. (2016). Thermographic test for the geometric characterization of cracks in welding using ir image rectification. *Automation in Construction*, 61:58–65.

[Roth et al., 2015] Roth, S.-N., Léger, P., and Soulaïmani, A. (2015). A combined XFEM–damage mechanics approach for concrete crack propagation. *Computer Methods in Applied Mechanics and Engineering*, 283:923–955.

[Ruocci et al., 2016] Ruocci, G., Rospars, C., Moreau, G., Bisch, P., Erlicher, S., Delaplace, A., and Henault, J.-M. (2016). Digital image correlation and noise-filtering approach for the cracking assessment of massive reinforced concrete structures. *Strain*, 52(6):503–521.

[Salman et al., 2013] Salman, M., Mathavan, S., Kamal, K., and Rahman, M. (2013). Pavement crack detection using the gabor filter. In *16th international IEEE conference on intelligent transportation systems (ITSC 2013)*, pages 2039–2044. IEEE.

[Schmidt et al., 2021] Schmidt, M., Schmidt, P., Wanka, S., and Classen, M. (2021). Shear response of members without shear reinforcement—experiments and analysis using shear crack propagation theory (SCPT). *Applied Sciences*, 11(7):3078.

[Seemab et al., 2022] Seemab, F., Schmidt, M., Baktheer, A., Hegger, J., Classen, M., and Chudoba, R. (2022). On the existence of the center of rotation around a shear crack; numerical inspection of digital image correlation measurements.

[Shirahata et al., 2014] Shirahata, H., Miki, C., Yamaguchi, R., Kinoshita, K., and Yaginuma, Y. (2014). Fatigue crack detection by the use of ultrasonic echo height change with crack tip opening. *Welding in the World*, 58(5):681–690.

[Sneddon, 1946] Sneddon, I. (1946). The distribution of stress in the neighborhood of a crack in an elastic solid. *Philosophical Transactions of the Royal Society of London, Series A*, 187(1009):1934–1990.

[Taerwe et al., 2013] Taerwe, L., Matthys, S., et al. (2013). Fib model code for concrete structures 2010.

[Talab et al., 2016] Talab, A. M. A., Huang, Z., Xi, F., and HaiMing, L. (2016). Detection crack in image using otsu method and multiple filtering in image processing techniques. *Optik*, 127(3):1030–1033.

[Tambusay et al., 2021] Tambusay, A., Suprobo, P., Suryanto, B., and Don, W. (2021). Application of Nonlinear Finite Element Analysis on Shear-Critical Reinforced Concrete Beams. *J. Eng. Technol. Sci.,*, 53(4):21.

[Teworte and Hegger, 2014] Teworte, F. and Hegger, J. (2014). Zum querkrafttragverhalten von spannbetonträgern unter ermüdungsbeanspruchung. Technical report, Lehrstuhl und Institut für Massivbau.

[Tran, 2020] Tran, N. L. (2020). A mechanical model for the shear capacity of slender reinforced concrete members without shear reinforcement. *Engineering Structures*, 219:110803.

[Tung et al., 2008] Tung, S.-H., Shih, M.-H., and Sung, W.-P. (2008). Development of digital image correlation method to analyse crack variations of masonry wall. *Sadhana*, 33(6):767–779.

[Vecchio and Collins, 1986] Vecchio, F. J. and Collins, M. P. (1986). The modified compression-field theory for reinforced concrete elements subjected to shear. *ACI J.*, 83(2):219–231.

[Vintzēleou and Tassios, 1986] Vintzēleou, E. and Tassios, T. (1986). Mathematical models for dowel action under monotonic and cyclic conditions. *Magazine of concrete research*, 38(134):13–22.

[Virtanen et al., 2020] Virtanen, P., Gommers, R., Oliphant, T. E., Haberland, M., Reddy, T., Cournapeau, D., Burovski, E., Peterson, P., Weckesser, W., Bright, J., van der Walt, S. J., Brett, M., Wilson, J., Millman, K. J., Mayorov, N., Nelson, A. R. J., Jones, E., Kern, R., Larson, E., Carey, C. J., Polat, İ., Feng, Y., Moore, E. W., VanderPlas, J., Laxalde, D., Perktold, J., Cimrman, R., Henriksen, I., Quintero, E. A., Harris, C. R., Archibald, A. M., Ribeiro, A. H., Pedregosa, F., van Mulbregt, P., and SciPy 1.0 Contributors (2020). SciPy 1.0: Fundamental Algorithms for Scientific Computing in Python. *Nature Methods*, 17:261–272.

[Walraven, 1980] Walraven, J. C. (1980). Aggregate interlock: a theoretical and experimental analysis.

[Westergaard, 1997] Westergaard, H. (1997). Bearing pressures and cracks.

[Westergaard, 1939] Westergaard, H. M. (1939). Bearing pressures and cracks. *Trans AIME, J. Appl. Mech.*, 6:49–53.

[Williams and Ewing, 1972] Williams, J. and Ewing, P. (1972). Fracture under complex stress—the angled crack problem. *International Journal of Fracture Mechanics*, 8(4):441–446.

[Wolf et al., 2015] Wolf, J., Pirskawetz, S., and Zang, A. (2015). Detection of crack propagation in concrete with embedded ultrasonic sensors. *Engineering Fracture Mechanics*, 146:161–171.

[Yang et al., 2018] Yang, X., Li, H., Yu, Y., Luo, X., Huang, T., and Yang, X. (2018). Automatic pixel-level crack detection and measurement using fully convolutional network. *Computer-Aided Civil and Infrastructure Engineering*, 33(12):1090–1109.

[Yang, 1999] Yang, Y. (1999). Effect of the regular term on the stress field in a joint of dissimilar materials under remote mechanical load. *Archive of Applied Mechanics*, 69(6):364–378.

[Yang, 2014] Yang, Y. (2014). Shear behaviour of reinforced concrete members without shear reinforcement: a new look at an old problem.

[Yiyang, 2014] Yiyang, Z. (2014). The design of glass crack detection system based on image preprocessing technology. In *2014 IEEE 7th Joint International Information Technology and Artificial Intelligence Conference*, pages 39–42.

Appendices

A Appendix

The code snippets for data extraction and the obtained results from the crack detection tool are compiled here in the appendix.

A.1 Code snippets

A.1.1 Displacement field and loading data

```
from os.path import join, expanduser
home_dir = expanduser('~')
data_dir = join(home_dir, 'simdb', 'data', 'shear_zone', dir_name, 'dic_point_data')

dic_param_file = join('dic_point_data', 'dic_params')
time_F_dic_file = join('dic_point_data', 'Kraft.DIM.csv')
```

A.1.2 Beam design

```
beam_param_file = join(dir_name, 'beam_params')

beam_param_types = {'L_right' : float,
                    'L_left' : float,
                    'B' : float,
                    'H' : float,
                    'n_s' : float,
                    'y_s' : float,
                    'd_s' : float}
```

A.1.3 Load displacement history

```
import pandas as pd
Import numpy as np
time_F_w_data_dir = join(dir_name, 'load_deflection')
time_F_w_m = np.array(pd.read_csv(time_F_w_data_dir, decimal=",", skiprows=1,
                              delimiter=None), dtype=np.float_))

time_m, F_m, w_m = time_F_w_m
n_m = len(time_m) #no. of machine sampling points up to the peak load
```

where, the index *m* used here represents the machine.

A.1.4 Time and force data from DIC Images

```
rows_ = []
for row in open(time_F_dic_file):
    rows_.append(row)
    rows = np.array(rows_)
    time_entries_dic = rows[0].replace('name;type;attribute;id;', '').split(';')
    tstring_dic = np.array([time_entry_dic.split(' ')[0] \\
    for time_entry_dic in time_entries_dic])
    time_dic = np.array(tstring_dic, dtype=np.float_)
    F_entries_dic = rows[1].replace('Kraft.DIM;deviation;dimension;;', '')
    F_dic = -np.fromstring(F_entries_dic, sep=';', dtype=np.float_)
    dF_dic = F_dic[np.newaxis, :] - F_dic[:, np.newaxis]
    dF_up_dic = np.triu(dF_dic > 0, 0)
    argmin_dic = np.argmin(dF_up_dic, axis=0)
    tstring_time_F_dic = tstring_dic[asc_dic], time_dic[asc_dic], F_dic[asc_dic]

n_dic = len(time_dic[asc_dic])
```

A.1.5 Displacement history of the DIC grid

```
pxyz_file_T = os.path.join('dic_point_data',
r'Flaechenkomponente 1_0.000 s.csv'.format(tstring))
for tstring in tstring_time_F_dic)
pxyz_list = [np.loadtxt(pxyz_file, dtype=np.float_, skiprows=6, delimiter=';',
\\ usecols=(0, 1, 2, 3))for pxyz_file in pxyz_file_T]

P_list = [np.array(pxyz[:, 0], dtype=np.int_) for pxyz in pxyz_list] \\
# Identify the points that are included in all time steps.
max_n_P = np.max(np.array([np.max(P_) for P_ in P_list])) + 1 \\
# Maximum number of points occurring in one of the time steps to allocate the space

data = np.load('dic_data')
X_TPa, F_T = data['X_TPa'], data['F_T']
X_0Pa = X_TPa[0,:,:] # take the first time step
U_TPa = X_TPa - X_0Pa[None,...] # broadcasting

X_pad_a = np.array([40, 40])
X_min_a = np.array([np.min(X_0Pa[:,a]+X_pad_a[a]) for a in (0,1)]) # left&bottom
X_max_a = np.array([np.max(X_0Pa[:,a]-X_pad_a[a]) for a in (0,1)]) # right&top

L_a = X_max_a - X_min_a # frame dimensions
d, n_a = 4,2 # node distance [mm], n_a dimensions
n_I, n_J = np.array(L_a/d,dtype=np.int_)
d_X_a = [L_a[0]/n_I,L_a[1]/n_J]

I,J,a = [np.arange(n) for n in (n_I,n_J,n_a)]
G_aIJ = (np.einsum('a, I->aI',(1-a),I)[:,:, None]+
         np.einsum('a, J->aJ',a,J)[:,None, :])

X_aIJ = (X_min_a[:,None,None]+
  np.einsum('aIJ,a->aIJ',G_aIJ,d_X_a))

from scipy.spatial import Delaunay
from scipy.interpolate import \
    LinearNDInterpolator as LNDI
triangulation = Delaunay(X_TPa[T])
U_TIJa = np.array([LNDI(tri,U_TPa[T])(X_aIJ)
  for T in range(n_T)])
```

A.1.6 Strain field history

```
xi_rij = np.array([[-1,-1],[1,-1],[1,1],[-1, 1]])
eta_mr = xi_ir / np.sqrt(3)
delta_rs = np.eye(2) # Kronecker delta
N_ijmn = 1/4*(1+
  np.einsum('rmn,rij->ijmn',eta_rmn,xi_rij)+
  np.einsum('rs,smn,sij,rmn,rij->ijmn',
  (1-delta_rs),eta_rmn,xi_rij,eta_rmn,xi_rij)/2)
dN_sijmn = 1/4*(xi_rij[:,:,:,None,None]+
  np.einsum('rs,sij,rmn,rij->sijmn',
  (1-delta_rs),xi_rij,eta_rmn,xi_rij))

G_aEF = G_aIJ[:,:-1,:-1] # w/o last col and row
H_aEiFj = (G_aEF[:,:,None,:,None]+
  g_aij[:,None,:,None,:])
X_EiFja = X_IJa[(H_aEiFj,)]
U_TEiFja = U_TIJa[(slice(None), H_aEiFj)]

J_EmFnas = np.einsum('sijmn,EiFja->EmFnas',
  dN_sijmn,X_EiFja)
inv_J_EmFnsa = np.linalg.inv(J_EmFnas)
Diff_abcd = 0.5*(
  np.einsum('ac,bd->abcd',delta_rs,delta_rs)+
  np.einsum('ad,bc->abcd',delta_rs,delta_rs))
B_EiFjmnabc = np.einsum('abcd,sijmn,EmFnsd->
  EiFjmnabc',Diff_abcd,dN_sijmn,inv_J_EmFnsa)
eps_TEmFnab = np.einsum('EiFjmnabc,TEiFjc->
  TEmFnab',B_EiFjmnabc,U_TEiFja)
```

A.1.7 Damage field history

```
eps_TEmFna, _ = np.linalg.eig(eps_TEmFnab)
kappa_TEmFn = np.max(eps_TEmFna, axis=-1)
omega_TEmFn = np.zeros_like(kappa_TEmFn)
eps_o,eps_f = 0.002,0.0028 # material params.
I = np.where(kappa_TEmFn>=eps0) # I-inelastic
omega_TEmFn[I] = 1.0-(eps_0/kappa_TEFm[I]*np.exp(
  -(kappa_TEmFn[I]-eps_0)/(eps_f-eps_0))) #(18)

X_aEmFn = np.einsum('ijmn,EiFja->aEmFn',
  N_ijmn,X_EiFja)
X_aKL = X_aEmFn.reshape(-1,(n_I-1)*2,(n_J-1)*2)
omega_TKL = omega_TEmFn.reshape(
  -1,(n_I-1)*2,(n_J-1)*2)

from scipy.interpolator import \
  RegularGridInterpolator as RGI
la_T = F_T / np.max(F_T)
get_omega_Ixy = RGI((la_T,)+ *X_aKL),omega_TKL)
get_Ua_Ixy = RGI((la_T,)+ *X_aIJ),U_TIJa)
get_Xa_Ixy = RGI((la_T,)+ *X_aIJ),X_TIJa)
```

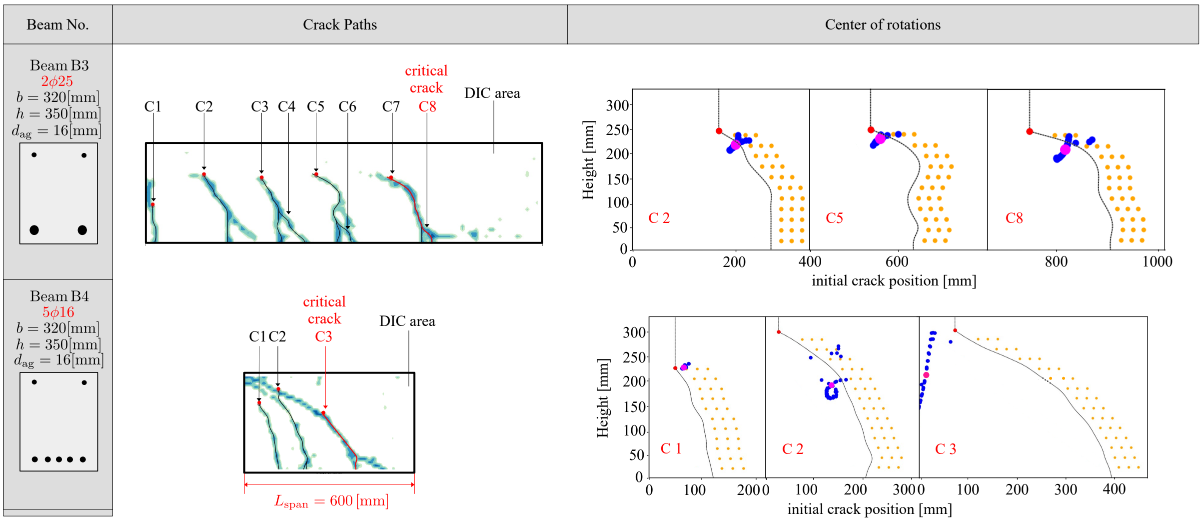

Figure A.1: Evaluation of COR for beam B3 and beam B4

A.2 COR evaluation

A.2.1 Beam B3

The evaluation of COR for beam B3 for cracks C2, C5 and C8 is shown in Fig. A.1. The study shows that the COR is present below the crack tip at the ultimate state for the reported cracks i.e. C2, C5, and C8.

A.2.2 Beam B4

The COR for all cracks in beam B4 is reported in Fig. A.1. The study shows that the existence of COR is above the crack tip for crack C1 while for cracks C2 and C3 the COR is found to exist below the crack tip at the ultimate state.

A.3 COR trend study

A.3.1 Beam B3

By looking at the Δ_x studies for beam B3 (see Fig, A.2), one can visualize that at some points during the loading history the COR is found to be located on the right side of the crack tip for cracks C1, C2, C3, C5 and C7 whereas for crack C8 (that is just a branching of crack C7 appearing near the peak of the loading history) it appears to be always on the right of the crack tip. It was also noted that for crack C6, the center of rotation was far from the crack tip for one step, despite appearing to be close to the crack tip for all previous load stages. On average, COR is found to be on the left side of the crack tip

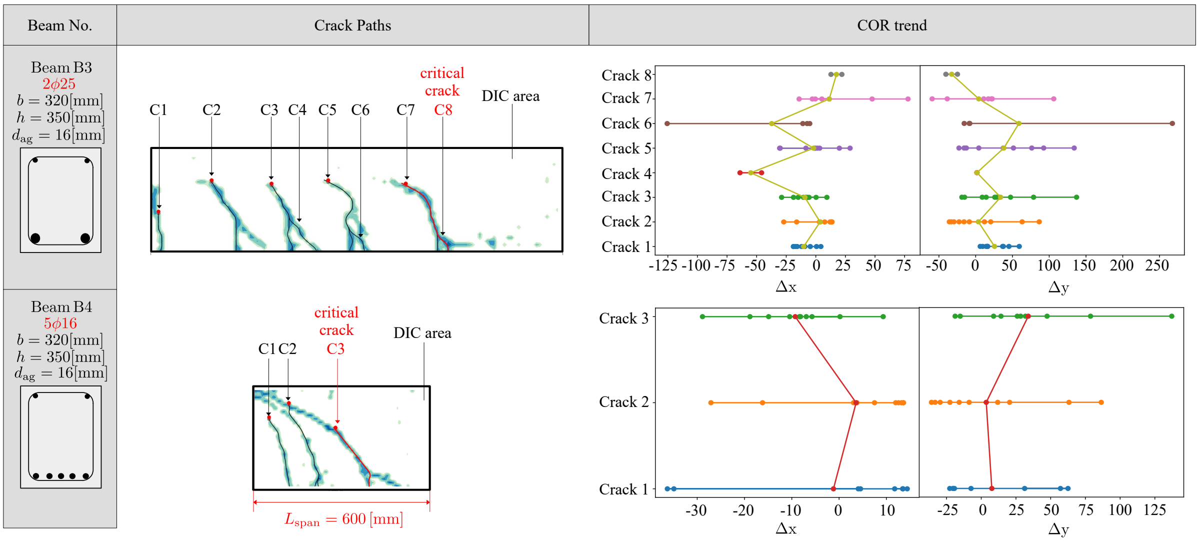

Figure A.2: COR trend study for beam B3 and beam B4

for cracks C1, C3, C4, and C6, but appears to be on the right side of the crack for cracks C2, C7, and C8. It is clear that the COR is quite close to the crack tip for crack C5, as shown by the average.

The studies for Δ_y show that the COR was mostly above the crack tip, however for cracks C2, C3, C5, C6, and C8, the COR moved below the crack tip during several loading stages. For crack C8, the COR was always below the crack tip, while for crack C4, it was always in the close proximity of the crack tip. The average of all cracks reveals that the COR is above the crack tip for cracks C1, C3, C5, and C6 and below the crack tip for cracks C2, C4, and C7..

A.3.2 Beam B4

The study on Δ_x show that COR for all three cracks appear to be oscillating in between the left and right side of the crack tip while the average of two cracks out of three depicts that COR is on the right side of the tip.

Similarly, Δ_y shows that COR is also oscillating vertically above and below the crack tip while it average shows that it is existing above the crack tip for crack C1, C3. The average of difference shows that COR appears to be close to the crack tip only for crack C2.

A.4 Stress and force resultants

A.4.1 Beam B3

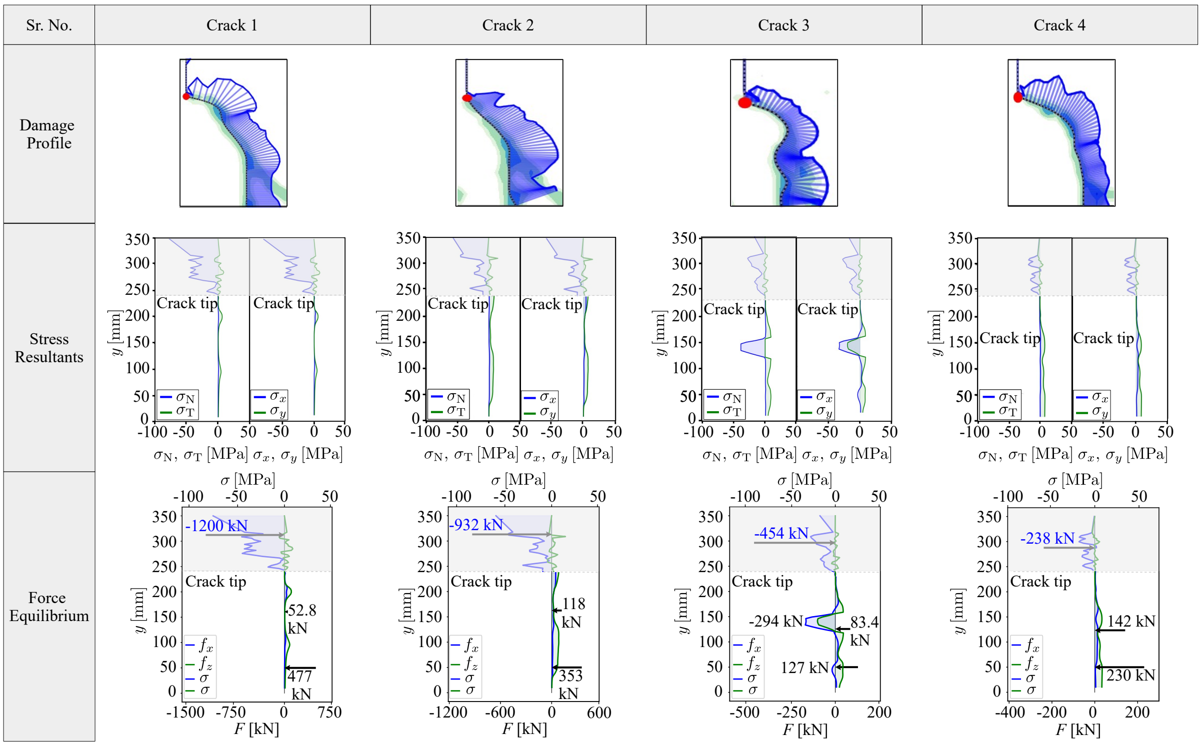

Figure A.3: Damage, stress profiles and force equilibrium for all cracks in beam B3

The damage and stress profiles for all the cracks existing in beam B3 is depicted in A.3. The horizontal force equilibrium is not satisfied for all the major cracks existing in the beam.

A.4.2 Beam B4

Sr. No.	Crack 1	Crack 2	Crack 3
Damage Profile	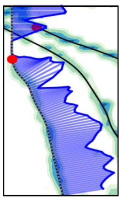	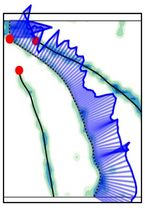	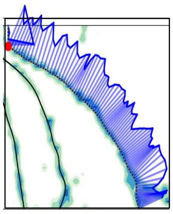
Stress Resultants	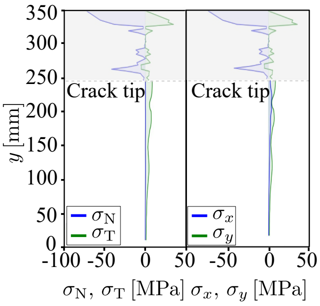	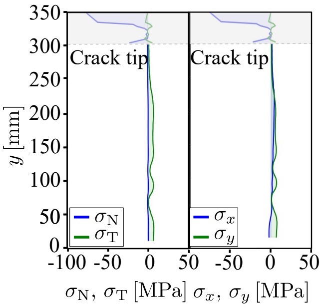	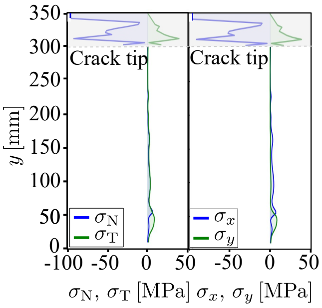
Force Equilibrium	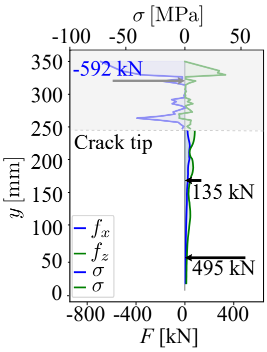	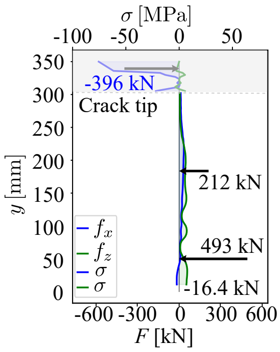	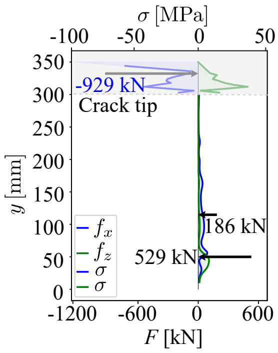

Figure A.4: Damage, stress profiles and force equilibrium for all cracks in beam B4

The damage and stress resultants for all the cracks in beam B4 is shown in Fig. A.4. Crack C1 seems to be approximately in equilibrium with reference to horizontal forces while equilibrium for cracks C2, and C3 is not satisfied.

A.5 External and internal moments comparison for all cracks

A.5.1 Beam B3

<table>
<tr><th>Sr. No.</th><th>Crack 1</th><th>Crack 2</th><th>Crack 3</th><th>Crack 4</th></tr>
<tr><td>Moment Time curve</td>
<td>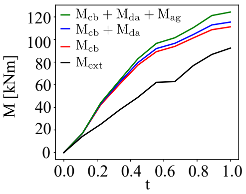
</td>
<td>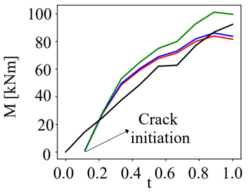
</td>
<td>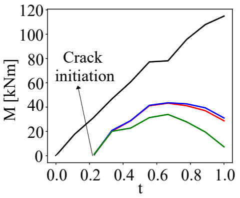
</td>
<td>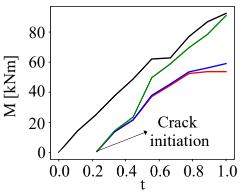
</td>
</tr>
</table>

Figure A.5: Moment-time curve for all primary cracks in beam B3

As soon as the load is put on the beam, crack C1 starts to initiate. It is clear that both cracks C1 and C2 are caused by aggregate interlocking, which reveals that shear is the mechanism that controls crack propagation. Also, for cracks C1 and C2, the internal moment values are higher than the external moment. For crack C3, a different trend is seen: the aggregate interlock action looks to go to zero near the end of the loading history, whereas the corresponding internal moment starts to diminish after 0.6*t* in the loading history and is very little compared to the external moment. For crack C4, the aggregate interlock contribution is very high, so at the end of the loading history, the internal and external moments are about the same.

A.5.2 Beam B4

<table>
<tr><th>Sr. No.</th><th>Crack 1</th><th>Crack 2</th><th>Crack 3</th></tr>
<tr><td>Moment Time curve</td>
<td>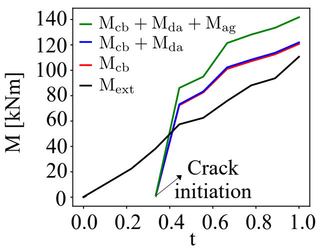
</td>
<td>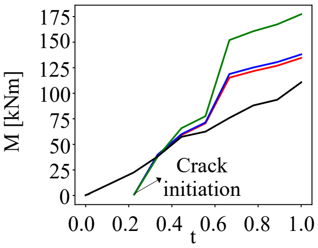
</td>
<td>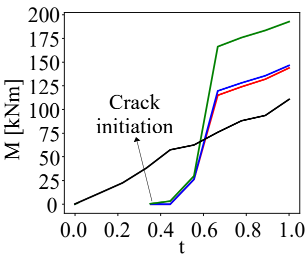
</td>
</tr>
</table>

Figure A.6: Moment-time curve for all primary cracks in beam B4

For all cracks in beam B4, the internal moment is found to be higher in comparison to the M_{ext}. Furthermore, the internal moment from aggregate is significant for all cracks which is also evident from the diagonal crack paths of all the cracks propagating in beam B4.

A.6 Moment and Shear profile

A.6.1 Beam B3 and B4

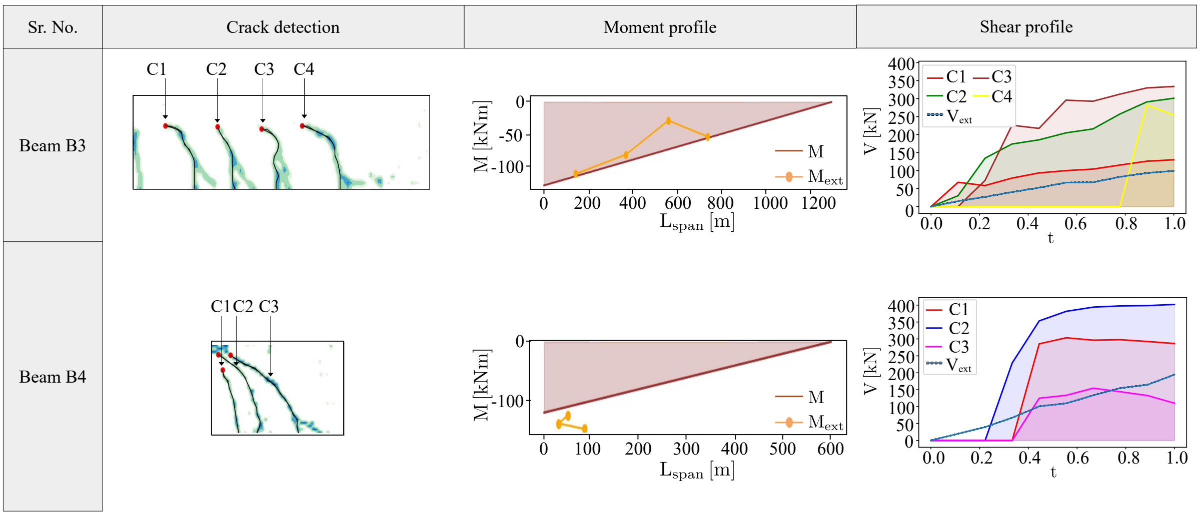

Figure A.7: Moment and shear profiles for beam B3 and B4

The moment and shear profiles for beams B3 and B4 are reported in Fig. A.7. The moment profile for beam B3 shows a very close approximation to the external bending moment while for beam B4 the trend does not show a clear pattern. The shear profiles for all the cracks for beam B3 and B4 depict that the shear resistance from all cracks is higher then the V_{ext} while only for crack C3 in beam B4, the shear resistance is in close approximation to the external shear force.